UC Berkeley
UC Berkeley Electronic Theses and Dissertations

Title
Renewable electrochemical fuel production: Fundamental principles and materials development

Permalink
https://escholarship.org/uc/item/6hm6j0ss

Author
Resasco, Joaquin

Publication Date
2017

Peer reviewed|Thesis/dissertation

eScholarship.org Powered by the California Digital Library
University of California

Renewable electrochemical fuel production: fundamental principles and materials development

By

Joaquin Resasco

A dissertation submitted in partial satisfaction of the

requirements for the degree of

Doctor of Philosophy

in

Chemical Engineering

in the

Graduate Division

of the

University of California, Berkeley

Committee in charge:

Professor Alexis Bell, Chair

Professor Bryan McCloskey

Professor Peidong Yang

Fall 2017

Renewable electrochemical fuel production: Fundamental principles and materials development

© 2017

By

Joaquin Resasco

Abstract

Renewable electrochemical fuel production: Fundamental principles and materials development

By

Joaquin Resasco

Doctor of Philosophy in Chemical Engineering

University of California, Berkeley

Professor Alexis Bell, Chair

Direct solar to fuel conversions offer an attractive and sustainable alternative to the use of fossil fuels an energy source. Electrochemical reactions can produce fuels that act as an energy storage medium for intermittent solar energy. However, current limitations in both materials development and fundamental understanding of electrochemical processes has limited the efficiency of photoelectrochemical systems. In the first portion of this dissertation, we discuss the simplest electrochemical process for producing a fuel using solar energy: water splitting to form hydrogen and oxygen. For this reaction, we discuss how materials development strategies can be developed to maximize the performance of the catalytic and light absorbing components of a photoelectrode. In particular we explore how one dimensional nanostructures can be utilized to improve performance for water oxidation. Although these nanostructures have several beneficial properties, their applicability can be hindered by difficulty in tuning the material composition without sacrificing morphology and material quality. In the first study, we present a method for controlling the composition of metal oxide nanowires without changing their morphology or crystallinity. In particular using this method based on solid state diffusion, and a novel process for manganese oxide atomic layer deposition, we produced manganese doped rutile TiO_2 nanowires. Using a variety of physical characterization techniques, it was determined that Mn could be incorporated as a substitutional dopant for Ti in the rutile lattice. We investigated how this compositional control allows for modification of the optical, electronic, and electrochemical properties of the semiconductor nanowire. The doping process resulted in an enhancement in the electrocatalytic activity for water oxidation, consistent with theoretical predictions. This demonstrated that this simple and general method could be used to control the properties of one-dimensional nanostructures.

We then utilized this technique to improve upon the efficiency of light absorbing photoandoes for water oxidation. Metal oxides that absorb visible light such as monoclinic $BiVO_4$ are attractive for use in this application. However, their performance is often limited by poor charge carrier transport. We investigated the possibility of addressing this issue by using separate materials for light absorption and carrier transport. As a carrier transport material, we used TiO_2 nanowires, modified with a Ta dopant to improve the conductivity. The doping process was accomplished using the previously mentioned solid state diffusion technique. $BiVO_4$ was added to these conductive nanowire arrays as a visible light sensitizer. Electrochemical and spectroscopic measurements were used to provide experimental evidence for the correct band alignment needed for favorable electron transfer from $BiVO_4$ to TiO_2. This host−guest nanowire architecture allows for the benefits of both materials to be taken advantage of, resulting in both high light absorption and carrier collection efficiency. This system resulted in an onset of anodic photocurrent near 0.2 V vs RHE, and a photocurrent density of 2.1 mA/cm^2 at 1.23 V vs RHE.

In the second portion of this work, we discuss the more complex reaction of carbon dioxide reduction. This reaction is appealing because it can produce more energy dense carbonaceous fuels, rather than hydrogen. While this is an appealing prospect, the efficiency of CO_2 reduction systems is currently lower than those for water splitting. One reason for this is that the fundamental understanding of electrochemical processes for this reaction are still lacking, particularly in how the conditions used for testing catalysts for this reaction can significantly impact the measured performance. In particular, it has been shown that the choice of both electrolyte cation and anion has an impact on the measured electrocatalyst performance. In the final works we seek to develop a deeper understanding of these effects using a combination of experimental and theoretical methods.

The first study focuses on the effect of alkali metal cations on the on the intrinsic activity and selectivity of metal catalysts for the reduction of CO_2. Experiments were conducted under conditions where mass transport limitations were minimal to show that cation size affects the intrinsic rates of formation of certain reaction products. Over Cu oriented thin films, increasing cation size increased rates of production of $HCOO^-$, C_2H_4, and C_2H_5OH, while CO and $HCOO^-$ rates increased over polycrystalline Ag and Sn. Reduction of key reaction intermediates identified the elementary reaction steps affected by cation size, namely the activation of CO_2 and the formation of carbon carbon bonds. Density functional theory calculations demonstrated that the alkali metal cations influence the CO_2 reduction reaction due to electrostatic interactions between solvated cations present at the outer Helmholtz plane and polarizable adsorbed species. The observed trends in activity with cation size are attributed to an increase in the concentration of cations at the outer Helmholtz plane with increasing cation size.

The next study presents a combination of experimental and computational studies aimed at understanding the role of electrolyte anions on the reduction of CO_2 over Cu surfaces. The effects of bicarbonate buffer concentration and identity on the rates of formation of the major products formed by reduction of CO_2 over Cu was investigated experimentally. It was demonstrated that the composition and concentration of electrolyte anions has relatively little effect on the formation of CO, $HCOO^-$, C_2H_4, and CH_3CH_2OH, but significantly affects the formation of H_2 and CH_4. Numerical simulations were used to assess the magnitude of changes in pH at the electrode surface for different electrolytes. The influence of pH on the activity of Cu for producing H_2 and CH_4 was also considered. It was determined that these differences in pH at

electrode surface were insufficient to explain the trends in activity and selectivity observed with changes in anion buffering capacity observed for the formation of H_2 and CH_4. We therefore proposed that these differences are the result of the ability of buffering anions to donate hydrogen directly to the electrode surface and in competition with water. The effectiveness of buffering anions to serve as hydrogen donors is found to increase with decreasing pKa of the buffering anion. This understanding of how electrochemical conditions affect measured activity can lead to insights into how to maximize efficiency of CO_2 reduction systems.

To my parents, Daniel and Teresita.

Table of contents

Acknowledgements

I would first like to thank Professor Alex Bell for the opportunity to work with him over the last few years. Your guidance and mentorship has made me a better and more thoughtful scientist. Your dedication and enthusiasm for science over your extensive career will be a constant source of inspiration for me going forward. I have greatly enjoyed my time working with you. I would also like to thank Professor Peidong Yang for also allowing me to work in such an exciting research environment. Your commitment to research has motivated me to always strive further in approaching scientific problems.

I would also like to thank other faculty members who have been very supportive of me throughout my time in Berkeley. To Professor Enrique Iglesia, I am very grateful for your advice and support, and for being a role model to me in both teaching and research. I would also like to thank Professor Tom Jaramillo at Stanford University, for his positivity and mentorship throughout my graduate experience.

I have had the privilege of working with many incredibly talented and friendly researchers at Berkeley. The time I spent working with you has made my graduate research both educational and enjoyable, and I wish you all the best of luck in your future. In particular I must thank Nick Kornienko, Nigel Becknell, and Anthony Fu, who managed to make late nights at the synchrotron fun. Thanks also to Sean Andrews, for keeping humor alive in the lab. Chong Liu and Neil Dasgupta, thank you for being great teachers when I was getting started in research. To Hao Zhang, Yude Su, and Yanwei Lum, thank you for being great labmates. I must also give a special thanks to Ezra Clark, who has been both a great friend and research teammate. I must also thank the great coworkers and collaborators I have had from outside Berkeley, in particular Professor Alex Briseno, Karen Chan, Leanne Chen, and Charlie Tsai.

To all of my friends, both the ones I made in Berkeley, and my friends from home, thank you for being there. To my dearest friend, Stella, thank you for putting a smile on my face every day.

I would not be here were it not for my wonderful family. To my mother, Teresita, thank you for your selfless love and support. To my father, Daniel, you are my greatest teacher and role model. Thank you both for everything that you have done for me. To my brothers and sisters, thank you for all that you do.

And finally to Ieva, thank you for being my companion through graduate school and making the last five years so enjoyable. I look forward to a life of adventures with you.

Chapter 1

Introduction to electrochemical energy conversion reactions

1.1 Abstract

Direct solar to fuel conversions offer an attractive solution to the replacement of fossil fuels with a sustainable energy source. However, designing efficient, stable, and cost effective photoelectrochemical systems is hindered by both fundamental understanding of electrochemical processes, and materials development. We first discuss the simplest electrochemical process for producing a fuel from sunlight: water splitting to form hydrogen and oxygen. For this more simple process, we discuss how materials development strategies can be developed to maximize the performance of the catalytic and light absorbing components of a photoelectrode. We then discuss the more complex reaction of carbon dioxide reduction, which is appealing due to its ability to produce more energy dense carbonaceous fuels. We demonstrate that fundamental understanding of electrochemical processes for this reaction are still lacking, particularly in how the conditions used for testing catalysts for this reaction can significantly impact the measured performance. We close with an outlook for future research directions for electrochemical production of fuels.

1.2 Introduction to water splitting

Finding a carbon neutral source of energy which can replace fossil fuels in a scalable and cost effective way is one of the most important issues facing modern society.[1, 2] Burning fossil fuels as a source of energy leads to an increased concentration of atmospheric CO_2 with an associated rise in global temperatures, a change with significant environmental consequences. Collecting energy from sunlight offers a potential solution to this problem. The solar resource is nearly inexhaustible, as the solar energy striking the earth's surface exceeds the global energy demand by over four orders of magnitude.[3, 4] However, the intermittent nature of photovoltaic energy production means that large scale implementation of this technology must be

accompanied by an energy storage system.[5] Energy storage at the TW scale remains a challenging problem using existing technologies such as batteries. Therefore, the use of solar energy to drive chemical reactions to produce chemical fuels such as hydrogen or hydrocarbons provides an attractive solution that could also fit well into the current energy infrastructure.

The concept of using sunlight to store energy in the form of chemical bonds was first demonstrated by Fujishima and Honda in 1972.[6] In this seminal study anatase TiO_2 was used as a photocatalyst to split water into molecular H_2 and O_2 without external bias. This photoelectrochemical (PEC) process contains two distinct processes, the absorption of light resulting in the generation of excited charge carriers, and the utilization of these carriers to drive chemical transformations.[7] Under illumination, the semiconductor produces excited carriers which are separated by the built-in electric field resulting from the semiconductor-liquid junction. The charge carriers are then transported to surface catalytic sites to carry out oxidation/reduction reactions. This process is illustrated in Fig 1A. The energy requirement for these transformations is determined by the thermodynamics of the chemical reactions involved. The reaction free energy for the water splitting reaction ($H_2O \rightarrow H_2 + 1/2\ O_2$) is 237.2 kJ/mol at standard conditions, which corresponds to 1.23 V per electron transferred per the Nernst equation.[8] Therefore to drive the water splitting reaction a semiconductor must absorb light with energy of at least 1.23 eV and be able to convert this energy into splitting water into H_2 and O_2.

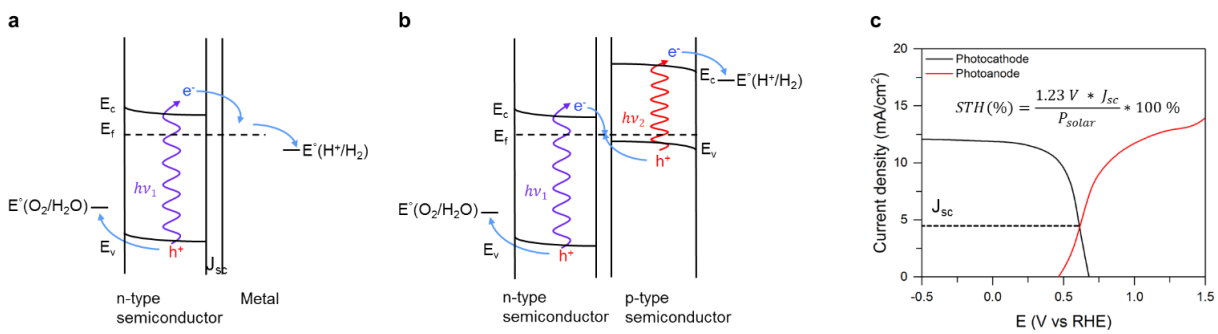

Figure 1.1 Energy diagrams for a water splitting cells (a) a single wide band gap n-type semiconductor photoanode with metal cathode; (b) a dual band gap p/n-PEC configuration with n-type and p-type photoelectrodes connected by an ohmic contact (c) Operation of a dual light absorber water splitting cell: Current vs potential with indicated point of operation for overall water splitting.

In addition to the thermodynamic energy requirement, an electrochemical overpotential is needed such that the reactions can proceed at an appreciable rate. In practice, this overpotential is on the order of 0.1 V for the hydrogen evolution reaction and 0.3 V for the oxygen evolution reaction, even for the most active electrocatalysts.[9, 10] This means that in practice the semiconductor must provide photovoltage significantly above the thermodynamic requirement of 1.23 V. Using a single light absorber, a band gap of at least ~2 eV is needed to provide this voltage.[11, 12] Few solar photons are sufficiently energetic to excite these semiconductors, meaning these materials will have poor utilization of the solar spectrum, leading to low solar to hydrogen efficiencies.[13] For spontaneous water splitting the positions of the conduction and valence bands of the semiconductor must straddle the H^+/H_2 reduction and H_2O/O_2 oxidation potentials (Figure 1A). To alleviate some of these constraints on a single material, a dual light-absorber approach can be used, with separate semiconductor materials that utilize distinct portions of the solar spectrum. In this configuration, one semiconductor acts as a photocathode and drives the reduction reaction,

while the other acts as a photoanode and drives the oxidation reaction.[7] In the two semiconductors, photogenerated minority carriers will move to the semiconductor liquid junction where they carry out their respective redox reactions, while majority carriers recombine at the semiconductor-semiconductor interface. This process is illustrated in Fig 1B. This scheme greatly relaxes the requirements on the semiconductor materials and allows for significantly higher theoretical solar to hydrogen efficiencies.[11, 12] As the components of a water splitting cell are electrically connected, the current is matched throughout the device. This means the efficiency of the device is limited by the performance of the weakest light absorber or surface cocatalyst.[14] Therefore, to achieve high efficiencies, both light absorbers and cocatalysts must be considered, such that the turnover frequency of the electrocatalyst is sufficient to handle the flux of photogenerated carriers reaching the surface. Additionally, there must be flux matching between the two semiconductor photoelectrodes, such that both the photoanode and photocathode provide the necessary voltage such that the operating point is near the maximum power point of the two separate light absorbers. This point is illustrated in Fig 1C. To date, effective matching between all components of the system has not been realized, due primarily to insufficient catalyst and semiconductor materials development.[15]

1.3 Development of nanostructured materials for water splitting

1.3.1 Current limitations for solar water splitting devices

In current water splitting cells, significantly more efficiency limitations are associated with the oxidation reaction than with the reduction reaction.[15] This is true both of the semiconducting light absorber and of the electrocatalyst.[9, 10] For the light absorbing material, this is due to the problems associated with achieving both high efficiency and operational stability. Conventional light absorber materials for photovoltaic applications such as Si, and the III-V and II-VI compounds have been largely unsuccessful because of their poor stability in solution. Recently, promising work has been done on stabilizing conventional light absorbers such as Si,[16] GaAs,[17] and InP.[18] However, the photovoltage obtained by these materials thus far has been insufficient to match with smaller band gap photocathode materials such as Si and InP in a dual absorber photoelectro-synthetic cell.[19, 20] Additionally, these materials have high production and processing costs.

In constrast, many binary oxide materials provide good stability under the highly oxidizing conditions of water oxidation.[21] However, the most commonly studied binary oxide, TiO_2, has a band-gap that is too large to absorb sunlight efficiently (~3.0 eV), consequently limiting its achievable photocurrent.[22] Small band gap metal oxides that absorb visible light and can be inexpensively synthesized, such as WO_3, Fe_2O_3, and $BiVO_4$, are alternative materials that hold promise to overcome these limitations.[23-25] Hematite (Fe_2O_3), has a desirable band gap of ~2.2 eV, making it a visible light absorber. However, hematite has a conduction band edge at 0.55 V versus the reversible hydrogen electrode (RHE), limiting its theoretical maximum photovoltage, and extremely poor charge transport properties that have prevented efficient charge separation. Thus reported efficiencies from hematite lag significantly below theoretical maximum values. $BiVO_4$ is another promising material due to its relatively small optical band

gap of ~2.5 eV and its negative conduction band edge (~0 V versus RHE).[26, 27] Under Air-Mass 1.5 Global (AM1.5G) solar illumination, the maximum achievable photocurrent for water oxidation using $BiVO_4$ is ~7 mA/cm^2.[25] However, the water oxidation photocurrent obtained in practice for $BiVO_4$ again is substantially lower than this value, mainly due to poor carrier transport properties, with electron diffusion lengths shorter than the film thickness necessary to absorb a substantial fraction of light.[26] The use of nanostructured materials could be particularly beneficial for these materials with poor carrier transport. In the following section, we describe how the use of one dimensional nanostructures for this application, and how their material composition can be controlled to give desired properties.

1.3.2 Semiconductor Nanowires for Solar Fuel Generation: Advantages and Challenges

One dimensional nanostructured materials, such as nanorods or nanowires, have unique properties that offer opportunities in a range of applications including solar and thermoelectric energy conversion, energy storage, and photonics.[28] Of particular interest here are their benefits for solar to fuel conversion. These benefits include enhanced light absorption, charge separation, and increased surface area for driving redox reactions.[14] The one dimensional morphology of the nanowire decouples the path lengths for light absorption and carrier collection, as they can provide a long optical path length for light absorption along the length of the nanowires, while minority carrier collection occurs over the short radial direction of the nanowire.[29, 30] This advantage is particularly important for indirect semiconductors and semiconductors with poor internal quantum efficiencies.[31] The large surface area afforded by the nanowire morphology decreases the requirements needed for electrocatalysts by diluting the number of charge carriers over a larger surface area. This means that the activity of each catalytic center, or turnover frequency, can be lower relative to the case of a planar electrode.

A large number of methods have been developed for synthesizing one dimensional nanostructures. However, synthesizing multinary one dimensional nanostructures with compositional tunability, while maintaining control over the morphology and material quality remains challenging using these traditional synthetic approaches. In chapter 2, we will demonstrate a new approach for producing multimetallic oxide nanowires with controllable composition. This composition control is provided by a simple solid state diffusion process that allows the structure and crystallinity of the desired nanostructure to be preserved. In chapter 3, we will demonstrate how we can use this method to improve the efficiency of photoanode materials for solar water splitting. This improvement is based on a host-guest structure, where conductive nanowires are used a scaffold for visible light absorbing sensitizers, thus allowing simultaneously high light absorption and carrier collection efficiency.

1.4 Fundamental principles of carbon dioxide reduction

Although water splitting can produce hydrogen, which has some appeal for its high specific energy (140 kJ/gram), the volumetric energy density of hydrogen is quite low, and storage and transportation of compressed hydrogen is problematic.[32] While renewable hydrogen is still very useful for a variety of applications, it would be appealing to use a similar solar driven electrochemical process to produce higher energy density carbon based fuels. The

electrochemical reduction of carbon dioxide (CO_2) offers an attractive option for doing this, utilizing CO_2 as a source of carbon for the production of transportation fuels and commodity chemicals using intermittent renewable electricity, such as that produced by wind or solar energy.

Extensive work has been done on identifying catalysts and understanding the reaction mechanism for CO_2 reduction.[33, 34] CO_2 can adsorb and be reduced to the two electron reduction products, carbon monoxide (CO) and formate ($HCOO^-$).[35] Carbon monoxide can be reduced further to produce hydrocarbons and oxygenates.[36] Alternatively, as the reduction potentials to produce these products are close to 0 V vs RHE, water can be reduced to form the undesired side product H_2.[37] Hydrocarbons and alcohols, rather than carbon monoxide and formic acid, are the preferred products of CO_2 reduction because of their high energy density. Despite extensive efforts aimed at identifying electrocatalysts that can produce these products, copper (Cu) remains the only material capable of doing so with significant yields.[33, 36, 38] Nevertheless, Cu requires a high overpotential (~−1 V versus RHE) and produces a broad spectrum of products.[39,37] Clearly, the discovery of novel means for reducing CO_2 to desirable products with higher efficiency and selectivity is needed. However, objective evaluation of the activity and selectivity of both standard and novel electrocatalysts is currently hindered by the lack of standardized methods for measuring and reporting electrocatalytic activity. These issues are significant because the performance of electrocatalyts is influenced not only by the composition and morphology of the electrocatalyst itself, but also by the conditions in which the electrocatalyst is tested, and by the purity of the electrocatalyst and electrolyte. For example, several studies have shown that the identity of both the cations and anions in the electrolyte can affect the activity of a catalyst and its selectivity to different products.[39, 40] However, understanding of the physical processes by which these species affect catalytic activity is still lacking. Developing this understanding of the fundamental processes occurring at the electrode surface, including both metal-adsorbate interactions, as well as the effects of solvation and interfacial electric fields is a first step in the direction of developing more efficient systems for reducing CO_2 to useful products.

1.5 Outline

Motivated by the above discussions, this thesis will begin by summarizing the results of materials development for photoelectrode systems for water oxidation. In chapter 2, we will demonstrate a new approach for producing multimetallic oxide nanowires with controllable composition. This composition control is provided by a simple solid state diffusion process that allows the structure and crystallinity of the desired nanostructure to be preserved. In chapter 3, we will demonstrate how we can use this method to improve the efficiency of photoanode materials for solar water splitting. This improvement is based on a host-guest structure, where conductive nanowires are used a scaffold for visible light absorbing sensitizers, thus allowing simultaneously high light absorption and carrier collection efficiency.

Following this, we will summarize work done based on developing an understanding of the fundamental principles involved in electrochemical reduction of CO_2. Electrochemical CO_2 reduction provides a potentially more interesting, but less well understood solar to fuel process relative to water splitting. We will begin in chapter 4 by developing a methodology for accurately measuring and reporting electrocatalyst performance for CO_2 reduction. Then, using this

methodology we will discuss how the electrochemical environment affects the catalytic performance measured. In chapter 5 we will discuss the effect of electrolyte cations on CO_2 reduction, and in chapter 6 we will discuss the effect of anions on CO_2 reduction. We will close with an outlook on how this information can be used in practical systems for CO_2 reduction.

1.6 References

1. Lewis, N. S.; Nocera, D. G. *Proc. Natl. Acad. Sci.* **2006,** 103, (43), 15729-15735.
2. Chu, S.; Majumdar, A. *Nature* **2012,** 488, (7411), 294-303.
3. Barber, J. *Chem. Soc. Rev.* **2009,** 38, (1), 185-196.
4. Blankenship, R. E.; Tiede, D. M.; Barber, J.; Brudvig, G. W.; Fleming, G.; Ghirardi, M.; Gunner, M. R.; Junge, W.; Kramer, D. M.; Melis, A.; Moore, T. A.; Moser, C. C.; Nocera, D. G.; Nozik, A. J.; Ort, D. R.; Parson, W. W.; Prince, R. C.; Sayre, R. T. *Science* **2011,** 332, (6031), 805-809.
5. Gray, H. B. *Nat. Chem.* **2009,** 1, 7.
6. Fujishima, A.; Honda, K. *Nature* **1972,** 238, 37.
7. Walter, M. G.; Warren, E. L.; McKone, J. R.; Boettcher, S. W.; Mi, Q.; Santori, E. A.; Lewis, N. S. *Chem. Rev.* **2010,** 110, (11), 6446-6473.
8. Tachibana, Y.; Vayssieres, L.; Durrant, J. R. *Nat. Photonics* **2012,** 6, 511.
9. McCrory, C. C. L.; Jung, S.; Peters, J. C.; Jaramillo, T. F. *J. Am. Chem. Soc.* **2013,** 135, (45), 16977-16987.
10. McCrory, C. C. L.; Jung, S.; Ferrer, I. M.; Chatman, S. M.; Peters, J. C.; Jaramillo, T. F. *J. Am. Chem. Soc.* **2015,** 137, (13), 4347-4357.
11. Seitz, L. C.; Chen, Z.; Forman, A. J.; Pinaud, B. A.; Benck, J. D.; Jaramillo, T. F. *ChemSusChem* **2014,** 7, (5), 1372-85.
12. Hu, S.; Xiang, C.; Haussener, S.; Berger, A. D.; Lewis, N. S. *Energy Environ. Sci.* **2013,** 6, (10), 2984.
13. Shockley, W.; Queisser, H. J. *J. Appl. Phys.* **1961,** 32, (3), 510-519.
14. Liu, C.; Dasgupta, N. P.; Yang, P. *Chem. Mater.* **2014,** 26, (1), 415-422.
15. McKone, J. R.; Lewis, N. S.; Gray, H. B. *Chem. Mater.* **2014,** 26, (1), 407-414.
16. Chen, Y. W.; Prange, J. D.; Duhnen, S.; Park, Y.; Gunji, M.; Chidsey, C. E.; McIntyre, P. C. *Nat. Mater.* **2011,** 10, (7), 539-44.
17. Hu, S.; Shaner, M. R.; Beardslee, J. A.; Lichterman, M.; Brunschwig, B. S.; Lewis, N. S. *Science* **2014,** 344, (6187), 1005-1009.
18. Sun, K.; Kuang, Y.; Verlage, E.; Brunschwig, B. S.; Tu, C. W.; Lewis, N. S. *Adv. Energy Mater.* **2015**, 5, 1402276.
19. Boettcher, S. W.; Warren, E. L.; Putnam, M. C.; Santori, E. A.; Turner-Evans, D.; Kelzenberg, M. D.; Walter, M. G.; McKone, J. R.; Brunschwig, B. S.; Atwater, H. A.; Lewis, N. S. *J. Am. Chem. Soc.* **2011,** 133, (5), 1216-9.
20. Lee, M. H.; Takei, K.; Zhang, J.; Kapadia, R.; Zheng, M.; Chen, Y. Z.; Nah, J.; Matthews, T. S.; Chueh, Y. L.; Ager, J. W.; Javey, A. *Angew. Chem. Int. Ed.* **2012,** 51, (43), 10760-4.
21. Ni, M.; Leung, M. K. H.; Leung, D. Y. C.; Sumathy, K. *Renew. Sust. Energy Rev.* **2007,** 11, (3), 401-425.

22. Chen, Z.; Jaramillo, T. F.; Deutsch, T. G.; Kleiman-Shwarsctein, A.; Forman, A. J.; Gaillard, N.; Garland, R.; Takanabe, K.; Heske, C.; Sunkara, M.; McFarland, E. W.; Domen, K.; Miller, E. L.; Turner, J. A.; Dinh, H. N. *J. Mater. Res.* **2011,** 25, (01), 3-16.
23. Liu, X.; Wang, F.; Wang, Q. *Phys. Chem. Chem. Phys.* **2012,** 14, (22), 7894-911.
24. Sivula, K.; Le Formal, F.; Gratzel, M. *ChemSusChem* **2011,** 4, (4), 432-49.
25. Park, Y.; McDonald, K. J.; Choi, K. S. *Chem. Soc. Rev.* **2013,** 42, (6), 2321-37.
26. Rettie, A. J. E.; Lee, H. C.; Marshall, L. G.; Lin, J.-F.; Capan, C.; Lindemuth, J.; McCloy, J. S.; Zhou, J.; Bard, A. J.; Mullins, C. B. *J. Am. Chem. Soc.* **2013,** 135, (30), 11389-11396.
27. Kim, T. W.; Choi, K.-S. *Science* **2014,** 343, (6174), 990-994.
28. Dasgupta, N. P.; Sun, J.; Liu, C.; Brittman, S.; Andrews, S. C.; Lim, J.; Gao, H.; Yan, R.; Yang, P. *Adv. Mater.* **2014,** 26, (14), 2137-2184.
29. Su, Y.; Liu, C.; Brittman, S.; Tang, J.; Fu, A.; Kornienko, N.; Kong, Q.; Yang, P. *Nat. Nanotechnol.* **2016,** 11, 609.
30. Kelzenberg, M. D.; Boettcher, S. W.; Petykiewicz, J. A.; Turner-Evans, D. B.; Putnam, M. C.; Warren, E. L.; Spurgeon, J. M.; Briggs, R. M.; Lewis, N. S.; Atwater, H. A. *Nat. Mater.* **2010,** 9, 239.
31. Kayes, B. M.; Atwater, H. A.; Lewis, N. S. *J. Appl. Phys.* **2005,** 97, (11), 114302.
32. Züttel, A. *Mater. Today* **2003,** 6, (9), 24-33.
33. Hori, Y., Electrochemical CO_2 Reduction on Metal Electrodes. In *Modern Aspects of Electrochemistry*, Vayenas, C. G.; White, R. E.; Gamboa-Aldeco, M. E., Eds. Springer New York: New York, NY, 2008; pp 89-189.
34. Peterson, A. A.; Abild-Pedersen, F.; Studt, F.; Rossmeisl, J.; Norskov, J. K. *Energy Environ. Sci.* **2010,** 3, (9), 1311-1315.
35. Hansen, H. A.; Varley, J. B.; Peterson, A. A.; Nørskov, J. K. *J. Phys. Chem. Lett.* **2013,** 4, (3), 388-392.
36. Hori, Y.; Wakebe, H.; Tsukamoto, T.; Koga, O. *Electrochim. Acta* **1994,** 39, (11), 1833-1839.
37. Kuhl, K. P.; Cave, E. R.; Abram, D. N.; Jaramillo, T. F. *Energy Environ. Sci.* **2012,** 5, (5), 7050-7059.
38. Kuhl, K. P.; Hatsukade, T.; Cave, E. R.; Abram, D. N.; Kibsgaard, J.; Jaramillo, T. F. *J. Am. Chem. Soc.* **2014,** 136, (40), 14107-14113.
39. Hori, Y.; Murata, A.; Takahashi, R. *J. Chem. Soc. Faraday Trans. 1* **1989,** 85, (8), 2309-2326.
40. Akira, M.; Yoshio, H. *Bull. Chem. Soc. Jpn.* **1991,** 64, (1), 123-127.

Chapter 2

Uniform Doping in Metal Oxide Nanowires by Solid State Diffusion

This chapter contains material from the following publication:
Resasco, J.; Dasgupta, N.P.; Roque-Rosell, J.; Guo, J.; Yang, P. *J. Am. Chem. Soc.* **2014,** 39, 10521.

2.1 Abstract

The synthesis of one-dimensional nanostructures with specific properties is often hindered by difficulty in tuning the material composition without sacrificing morphology and material quality. Here, we present a simple solid state diffusion method utilizing atomic layer deposition to controllably alter the composition of metal oxide nanowires. This compositional control allows for modification of the optical, electronic, and electrochemical properties of the semiconductor nanowires. Using this method and a novel process for manganese oxide atomic layer deposition, we produced manganese doped rutile TiO_2 nanowires and investigated their structural and photoelectrochemical properties. A homogeneous incorporation of the Mn dopant into the rutile lattice was observed, and the local chemical environment of the Mn was determined using X-ray absorption spectroscopy. The doping process resulted in a tunable enhancement in the electrocatalytic activity for water oxidation, demonstrating that this simple and general method can be used to control the properties of one-dimensional nanostructures for use in a variety of applications including solar-to-fuel generation.

2.2 Introduction

As discussed in the previous chapter, one dimensional nanostructured materials, such as nanorods or nanowires, exhibit unique properties that can be exploited in a diverse range of fields including photoelectrochemistry.[1] One dimensional semiconductor nanostructures are beneficial for use in photoelectrochemistry applications due to the large electrochemically available surface area afforded by their morphology, the decoupling of light absorption and minority carrier

diffusion lengths for efficient charge collection and separation, and enhanced light scattering and trapping in vertical arrays.[2-5]

A variety of methods have been developed for synthesizing one dimensional nanostructures including the vapor-liquid-solid,[6, 7] vapor-solid,[8] solution-liquid-solid,[9] and hydrothermal methods.[10] However, synthesizing ternary or other complex one dimensional nanostructures with compositional tunability, while maintaining control over the material quality and morphology remains challenging using traditional synthesis approaches. The simplest method for synthesizing bulk multinary compound solids is the solid state diffusion method, where reactants are mixed and heated to allow a diffusive transformation to the thermodynamically favored state. However, adapting this technique to one dimensional nanostructures requires a technique to uniformly coat their surfaces with precise control of material loading. One technique that meets this requirement is atomic layer deposition (ALD).[11] ALD is a modified form of chemical vapor deposition (CVD) based on sequential, self-limiting surface reactions. Due to the saturation of the substrate surface with the reactant species after each half-cycle, highly conformal films can be deposited on high aspect ratio structures with sub-nanometer control of film thickness. This technique has been previously demonstrated to precisely tune the optical and electrochemical properties of nanowires by fabrication of uniform core-shell structures.[12, 13] Here we demonstrate that a solid state diffusion process for one dimensional nanostructures can be achieved using ALD to precisely control the surface coating thickness, which is followed by a post annealing step. This approach provides a general method for producing doped or ternary metal oxide nanostructures with compositional control while maintaining the desired morphology.

In this chapter, we demonstrate the compositional control afforded by this method and show its utility for photoelectrochemical water splitting. TiO_2 has been the most widely studied material in this field since Fujishima and Honda's first demonstration of unassisted solar water splitting.[14] Although the wide band gap of TiO_2 limits the achievable photocurrent due to the limited number of solar photons in the ultraviolet range, transition metal doping of TiO_2 can lead to visible light absorption, potentially increasing the maximum achievable efficiency.[15-17] Additionally, theoretical and experimental investigations have shown that transition metal doping of TiO_2, particularly with Mn and Cr, increases the catalytic activity for the oxygen evolution reaction (OER).[18-20] Changing the catalytic activity in this way relies on the ability to introduce the dopants without modifying the original crystal structure, such that the binding strength of the surface to the reaction intermediates can be precisely altered.

This conversion chemistry approach provides a high degree of synthetic control, allowing for the study of the effect of changes in composition on the catalytic activity. We utilize this method to produce Mn doped TiO_2 nanowire arrays and study their photoelectrochemical properties. In subsequent chapters, we will further demonstrate the generality of this method using other compositions and its applicability to modify other material properties of interest in photoelectrochemistry.

2.3 Experimental methods

2.3.1 Synthesis of titanium dioxide nanowire arrays

Titanium dioxide (TiO_2) nanowires were synthesized by a hydrothermal method.[10] In a typical synthesis, 83 μL of titanium isopropoxide (Sigma-Aldrich) was mixed with 5 mL of 6M hydrochloric acid (Sigma-Aldrich) in a 40 mL telfon vessel. A fluorine-doped tin oxide (FTO) coated quartz substrate was angled against the wall of the Teflon vessel such that the FTO surface was facing down. The Teflon vessel was loaded in a stainless steel autoclave and heated to 210°C for 150 min. After cooling, the substrates were thoroughly rinsed in deionized water, yielding single crystalline rutile-TiO_2 nanowire arrays. For higher temperature annealing, a TiO_2 thin film (~30 nm) was deposited on a quartz substrate as a seeding layer for nanowire growth.

2.3.2 Atomic layer deposition of manganese oxide

Deposition of MnO_x thin films was performed in a customized thermal ALD reactor. The precursors used for MnO_x deposition were Manganese bis(N,N'-diisopropylacetamidinate) (Dow) and water. The manganese precursor was held in a customized bubbler that allowed for pulsed doses using nitrogen as a delivery gas through the bubbler, which was maintained at 100 °C. The water source was maintained at room temperature. The substrate temperature for MnO_x deposition was 150 °C. Typical pulse times for the manganese precursor and water were 1.5 and 1.0 sec, respectively. Nitrogen was used as a carrier and purge gas at a flow rate of 10 sccm.

2.3.3 Conversion process

After the atomic layer deposition process, the nanowire substrates were loaded into the center of a 1-inch diameter quartz tube and heated in a tube furnace under an Ar atmosphere at 873-1273 K for 1-24 hrs.

2.3.4 Physical and chemical characterization

The morphology of the nanowire substrates was studied using scanning electron microscopy (SEM). SEM images were collected using a JEOL JSM 6340F field-emission SEM operating at 5 kV. Phase information was obtained using X-Ray Diffraction (XRD). XRD patterns were collected using a Bruker D8 Advance diffractometer with Cu kα radiation. Individual nanowires were imaged by transmission electron microscopy (TEM) using a JEOL 2100-F Field-Emission Analytical TEM operated at 200 kV equipped with an analytical pole piece, a high solid-angle EDS system, and a HAADF (high-angle annular dark field) scanning TEM (STEM) detector, as well as a Hitachi H-7650 TEM operating at 120 kV. Chemical information about the Mn dopant atoms was investigated using X-ray photoelectron spectroscopy (XPS) and X-ray absorption spectroscopy (XAS). XPS spectra were collected using a PHI 5400 X-ray Photoelectron Spectrometer equipped with a 4 kV Argon ion gun, with Al Kα radiation. The angle between the source and detector was 35°. The measurement chamber was maintained at 10^{-9} eV during measurement, and measurements were taken at a pass energy of 17.9 eV. All energies were calibrated to spurious carbon at 285.0 eV.

XAS spectra were collected on beamline 10.3.2 at the Advanced Light Source (ALS) with an electron energy of 1.9 GeV and an average current of 500 mA. The radiation was

monochromated by a Si (111) double-crystal monochromator. The intensity of the incident X-ray was monitored by an N_2-filled ion chamber (I_0) in front of the sample. Fluorescence spectra were recorded using a seven-element Ge solid-state detector. The energy was calibrated using a glitch in the I_0 relative to the absorption edge of Mn foil. All spectra were collected at room temperature. Data reduction of XAS spectra was done using the commonly employed Athena software. Pre-edge and post-edge contributions were subtracted, and results were normalized to the absorption edge step. Background removal in k-space was achieved using a five-domain cubic spline. Curve fitting was performed with Artemis and IFEFFIT software using ab initio-calculated phases and amplitudes from the program FEFF 8.2.[21, 22] These *ab initio* phases and amplitudes were used in the EXAFS equation:

$$\chi(k) = S_0^2 \sum_j \frac{N_j}{kR_j^2} f_{eff_j}(\pi, k, R_j) e^{-2\sigma_j^2 k^2} e^{-2R_j/\lambda_j(k)} \sin(2kR_j + \phi_{ij}(k))$$

The neighboring atoms to the central atom are divided into *j* shells, with all atoms with the same atomic number and distance grouped into a single shell. Within each shell, the coordination number N_j denotes the number of neighboring atoms in shell *j* at a distance of R_j from the central atom. $f_{eff_j}(\pi, k, R_j)$ is the *ab initio* amplitude function for shell *j*, and the Debye-Waller term $e^{-2\sigma_j^2 k^2}$ accounts for the damping due to static and thermal disorder in absorber-backscatterer distances. The mean free path term $e^{-2R_j/\lambda_j(k)}$ reflects losses due to inelastic scattering, where $\lambda_j(k)$ is the electron mean free path. The oscillations in the EXAFS spectrum are reflected in the sinusoidal term, $\sin(2kR_j + \phi_{ij}(k)$ where $\phi_{ij}(k)$ is the *ab initio* phase function for shell *j*. S_0^2 is an amplitude reduction factor due to shake-up/shake-off processes at the central atom. The EXAFS equation was used to fit the experimental data using S_0, R, and the Debye-Waller factor (σ^2) as variable parameters. N was taken as known for these crystalline materials. For the energy (eV) to wave vector (k, $Å^{-1}$) conversion, E_0 was defined as 6547.5 eV and ΔE_0 was obtained in the fit. The optical absorption spectra were recorded using a UV-vis-NIR scanning spectrophotometer equipped with an integration sphere (Shimadzu UV-3101PC).

2.3.5 Electrochemical characterization

Electrochemical activity and stability of the nanowire substrates were studied in a three-electrode electrochemical cell using a Bio-Logic potentiostat/galvanostat with a built-in electrochemical impedance spectroscopy (EIS) analyzer. All CVs were iR-compensated at 85% and measured in 1 M KOH electrolyte at room temperature, using a platinum wire counter electrode and a Hg/HgO reference electrode. The potential scale was calibrated to a reversible hydrogen electrode (RHE). A 300-Watt Xe lamp equipped with an air mass 1.5G filter (Newport) was used as the light source. Prior to measurement, light intensity was standardized using a calibrated silicon photodiode.

2.4 Results and discussion

A novel method for atomic layer deposition (ALD) of manganese oxide was developed using a bis(isopropylacetamidinate)manganese precursor and water vapor as co-reactants. Previously reported work on ALD of manganese oxide has typically relied on cyclopentadienyl precursors.[23-25] Amidinates are well suited for use as ALD precursors due to their high volatility, thermal stability, and reactivity, and have been successfully used for ALD and CVD of various transition metals and transition metal oxides.[26-28] To measure film thicknesses, ALD MnO_x was deposited on planar Si substrates and conformally coated on TiO_2 nanowires yielding core-shell nanowires. The film thicknesses on Si were measured using ellipsometry, and the thickness on the nanowires was measured using transmission electron microscopy (TEM). Two important characteristics of an ALD reaction are the saturation of the surface reaction after each precursor pulse, and a linear relationship between film thickness and number of cycles after a sufficient number of cycles.[11] Saturating, linear growth was demonstrated indicating an ALD growth mode (Fig 1). A growth rate of ~1Å/cycle was measured both on Si substrates and TiO_2 nanowires, with no thickness gradient along the nanowire length. Using X-ray photoelectron spectroscopy (XPS), no measurable carbon or nitrogen was observed in the spectrum following a 1 min Ar sputtering (Fig 1). Because the amidinate ligand contains carbon and nitrogen, the lack of any organic contamination in the film indicates that the ALD surface reaction was complete, and the ligands were completely substituted for by oxygen from the H_2O. TEM analysis of a core-shell $TiO_2|MnO_x$ nanowire after 100 cycles is shown in Fig 2, showing a conformal coating. STEM mode EDS mapping and corresponding line scan of core-shell nanowire after 200 cycles showing confinement of the Mn to the shell of the wire and the Ti in the core.

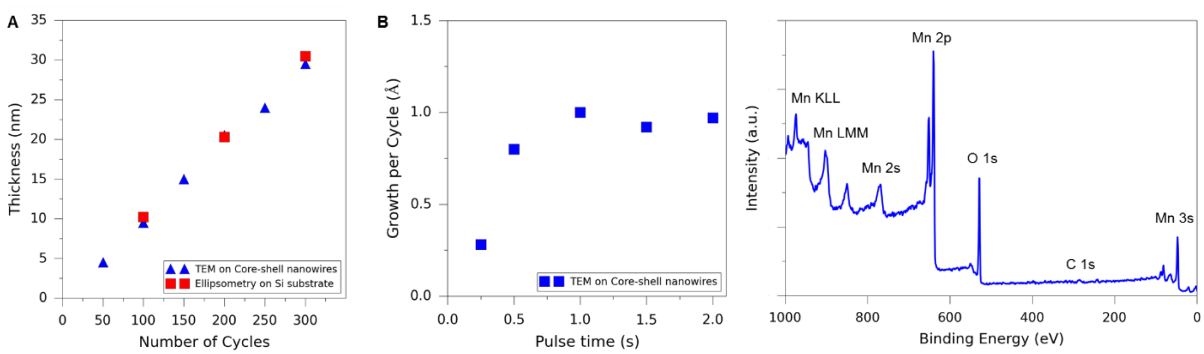

Figure 2.1: Characterization of MnO_x ALD (A) Thickness of MnO_x ALD films measured by TEM and ellipsometry as a function of number of cycles. A linear growth rate of ~1.0 Å/cycle was observed. (B) Growth rate per cycle of MnO_x ALD films under increasing pulse time of the Mn amidinate precursor. Saturation was observed after 1.0 s. (C) XPS survey spectra of MnO_x ALD films deposited using the Manganese bis(N,N'-diisopropylacetamidinate) following a 60 sec Ar sputter. The lack of carbon in the spectrum reflects the thermal stability of the amidinate precursor.

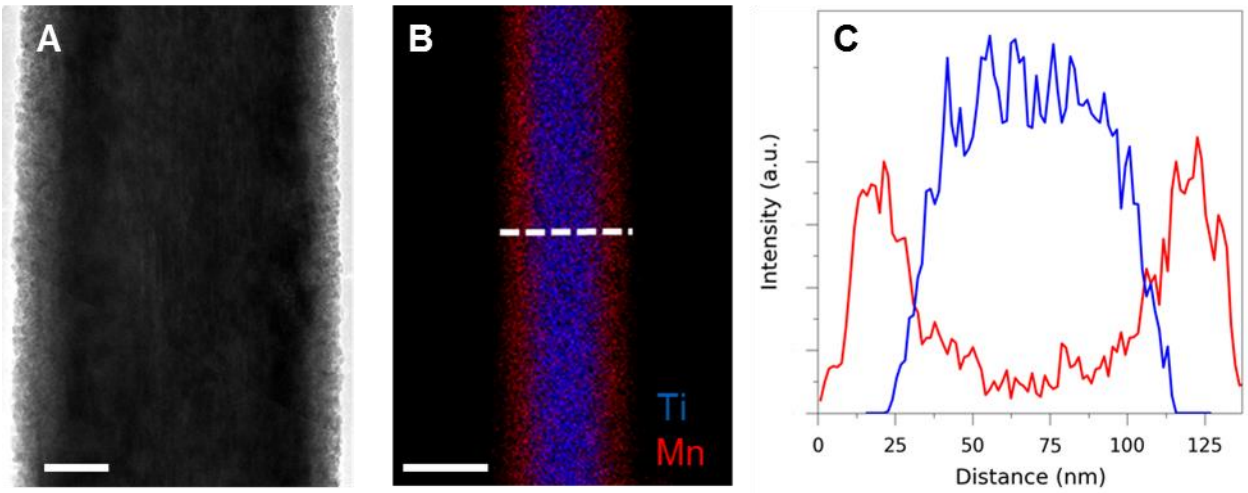

Figure 2.2: Core-shell nanowires produced by MnO_x ALD (A) TEM image of a core-shell $TiO_2|MnO_x$ nanowire after 100 cycles, showing a conformal coating. Scale bar is 20 nm. (B,C) STEM mode EDS mapping and corresponding line scan of core-shell nanowire after 200 cycles showing confinement of the Mn to the shell of the wire and the Ti in the core. Scale bar is 100 nm.

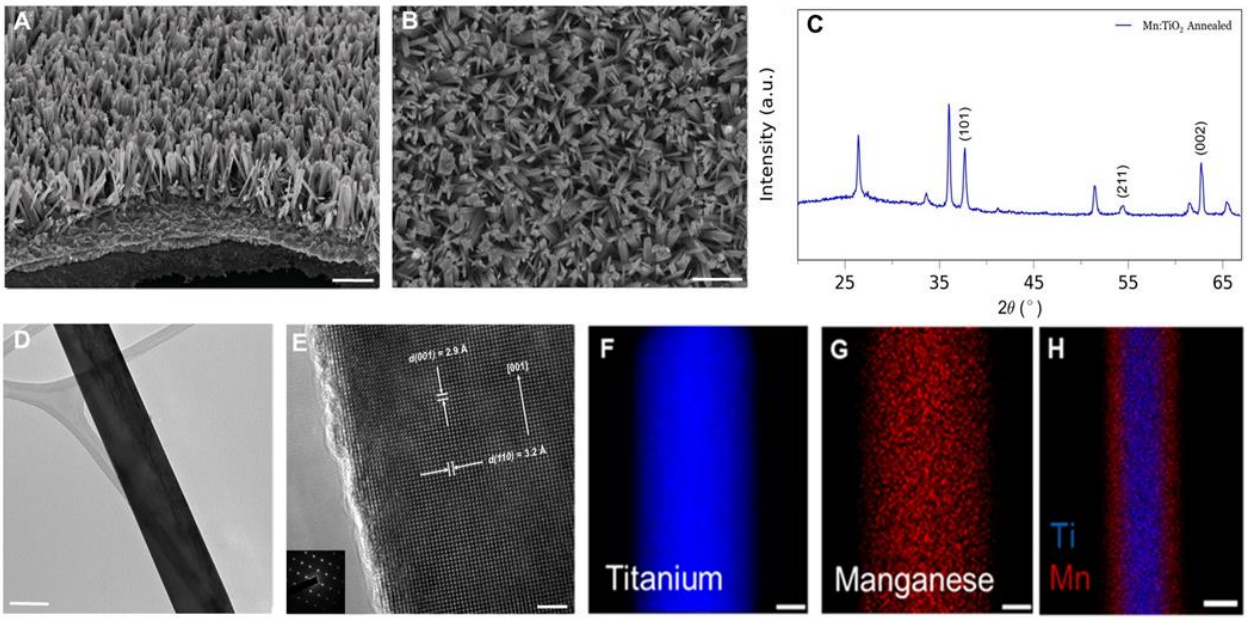

Figure 2.3: Uniformly doped TiO_2 nanowires using conversion chemistry approach (A,B) 45° and top down SEM images of vertically aligned Mn:TiO_2 nanowire array, scale bar is 1μm. (C) XRD pattern of converted nanowires showing only peaks for rutile TiO_2 and peaks corresponding to FTO substrate. Peaks for rutile TiO_2 are indicated. (D,E) TEM and HRTEM image of converted nanowire showing lattice spacing consistent with rutile TiO_2, scale bars are 100 and 2 nm, respectively. (F,G) STEM mode elemental maps of Mn and Ti in converted wire showing homogeneous incorporation of dopant, scale bars are 20 nm. (H) STEM mode elemental map of Mn and Ti in core-shell nanowire before annealing. Scale bar is 50 nm.

This ALD process was used to coat the TiO_2 nanowire arrays with manganese oxide, producing conformal core-shell nanowires with shell thicknesses that could be tuned with ~1Å

precision (Figure 3). The coated nanowire arrays were then annealed in an argon environment to facilitate diffusion of the manganese atoms into the rutile lattice, yielding Mn doped TiO_2 nanowires. The solid state diffusion process maintains the nanowire morphology as observed by scanning electron microscopy (SEM) with an average nanowire diameter ~100 nm and length of ~1.5 µm (Figure 3a,b). Energy dispersive X-ray spectroscopy (EDS) confirms the presence of Mn in the nanowire arrays and allows for quantification of the average Mn content as a function of number of ALD cycles. The average composition of Mn in the nanowire arrays can be precisely tuned by varying the shell thickness, and is in good agreement with calculated values for this nanowire geometry. The concentration of Mn could not be extended above 10%, which is likely due to the solubility limit of Mn in TiO_2. XPS confirmed that the near surface composition of the nanowires is similar to the average composition in the core. The X-ray diffraction (XRD) pattern of the nanowire substrates after annealing only contains peaks corresponding to the rutile phase, with no MnO_x or $MnTiO_x$ ternary phases observed (Figure 3c). With annealing temperatures above 1223 K, the ternary phase $MnTiO_3$ was formed for doped samples with Mn atomic concentrations above 5%. These higher annealing temperatures resulted in axially segmented nanowires with epitaxial interfaces between $MnTiO_3$ and TiO_2 (Figs 4-6). For the remainder of this chapter, discussion will focus on conditions in which ternary phases were not present.

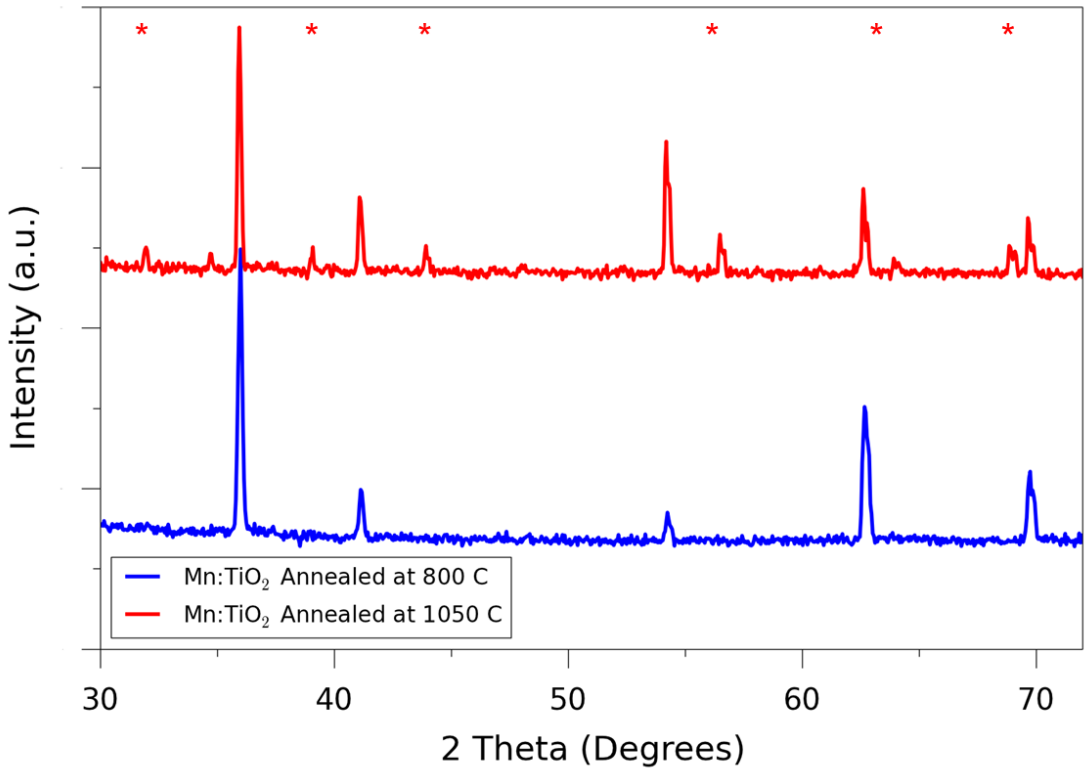

Figure 2.4: Ternary $MnTiO_3$ Phase Formation X-Ray Diffraction patterns for converted wire samples at different annealing temperatures. The ternary phase $MnTiO_3$ is formed at 1050°C. * indicates diffraction lines for $MnTiO_3$.

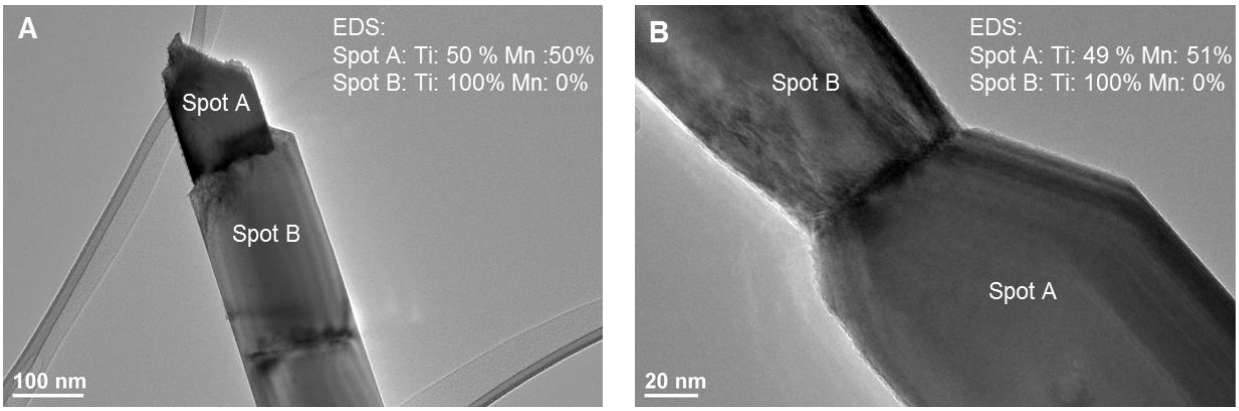

Figure 2.5: Microstructure of ternary phase nanowires (A,B) TEM images of nanowires converted at 1050°C. Nanowires phase segregate to form axial segments of pure $MnTiO_3$ and TiO_2. Axial segmentation is likely due to high diffusion rates of Mn^{2+} along c-axis. EDS confirms relative stoichiometry of Mn and Ti in segments.

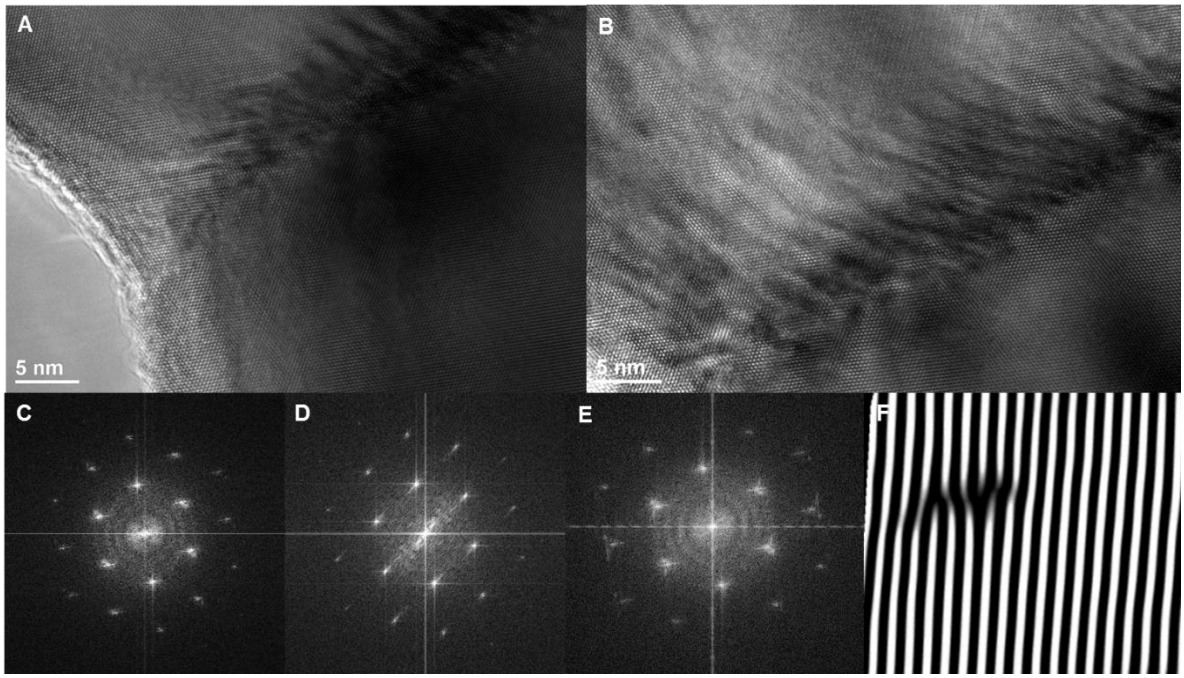

Figure 2.6: Interfaces of ternary phase nanowires (A,B) HRTEM images of nanowires converted at 1050°C, showing the interface between $MnTiO_3$ and TiO_2. (C-E) FFTs of TiO_2 section, $MnTiO_3$ section, and interface respectively. (F) Moiré image shows epitaxial interface between $MnTiO_3$ $1\bar{1}0$ and TiO_2 001 which can form due to the similarity of the oxygen sublattice in the two structures. However, edge dislocations are observed at the interface.

To determine the distribution of the dopant atoms in the TiO_2 nanowires and their effect of the nanowire structure, the converted nanowires were further analyzed by TEM. TEM images of

Mn doped TiO_2 nanowires show no sign of a MnO_x shell after annealing, indicating that the conversion process proceeded to completion. High resolution TEM (HRTEM) analysis was used to investigate the microstructure of the doped nanowires and indicated that the nanowires remained single crystalline after growth. Using HRTEM, we observed lattice spacing consistent with rutile TiO_2 with the nanowire growth axis parallel to the [001] direction. To obtain a visualization of the distribution of the Mn atoms within the TiO_2 lattice, Scanning TEM (STEM) mode EDS mapping was conducted. The elemental maps show a homogeneous incorporation of the Mn atoms, in contrast with the core-shell nanowire prior to annealing. Line scans across the diameter and length of the wire before and after annealing showed the conversion of the core-shell geometry into a homogeneous doped nanowire. The generality of the conversion chemistry approach will be discussed in subsequent chapters, as the method was also applied successfully to synthesize Ta doped TiO_2 using ALD of Ta_2O_5 as a dopant source. No signal from Sn or F was observed by EDS in any of the nanowires tested. The results of the TEM and XRD analyses suggest that this conversion process allows for controlled homogeneous doping of the TiO_2 nanowires while maintaining the original crystal structure.

From single crystal studies on metal ion diffusion in rutile TiO_2, the mechanism of diffusion is suggested to be dependent on the charge state of the ion.[29] Divalent impurity ions diffuse rapidly along open channels parallel to the c-axis and are pushed into substitutional Ti sites by interstitial Ti ions. Divalent ions therefore have a large anisotropy in diffusion coefficient for different crystallographic directions. Trivalent and tetravalent ions dissolve substitutionally and diffuse interstitially. Both mechanisms are important for mixed-valent impurity ions such as Mn. However, in this system, the concentration gradient exists in the radial direction, orthogonal to the c-axis. Therefore it is likely that the diffusion of Mn from the shell into the wire core is driven by Mn atoms dissolving substitutionally and diffusing through an interstitial mechanism. The larger diffusion coefficients observed for conversion in an Ar environment are a result of changes in point defect concentrations, namely oxygen vacancies and interstitial Ti atoms, with partial pressure of oxygen.

The transient diffusion of Mn in the TiO_2 nanowire can be described mathematically by Fick's Second Law:

$$\frac{\partial c_A}{\partial t} = D_{AB}\frac{\partial^2 c_A}{\partial x^2}$$

Where c_A is the concentration of Mn and x is the distance from the edge of the nanowire. The solution for diffusion into a finite medium solution can be obtained numerically and is available in for simple geometric shapes in Gurney-Lurie charts. The numerical solution would predict a more rapid conversion than the solution for a semi-infinite medium but otherwise similar diffusion profiles. Therefore as a simple approximation, the nanowire can be considered a semi-infinite medium to yield an analytical solution:

$$\frac{c_{As} - c_A}{c_{As} - c_{A0}} = \mathrm{erf}\left(\frac{z}{2\sqrt{D_{AB}t}}\right)$$

The surface concentration of Mn (c_{As}) can be taken as unity as the nanowire shell is manganese oxide. The initial concentration of Mn in the nanowire (c_{A0}) is zero. From single

crystal studies the diffusion coefficients of various transition metals in rutile TiO_2 at different partial pressures of oxygen are known.[29] The diffusion coefficients of interest here are those orthogonal to the c-axis, which are lower than those parallel to the c-axis. The diffusion coefficients were also measured to be substantially higher at low partial pressures of oxygen. The diffusion coefficient of Mn in TiO_2 is quite high: $1.1*10^{-10}$ cm^2/s at 900°C in air. As the diffusion distance is quite small as the nanowire diameter is ~100 nm, the nanowires readily become fully converted at high temperature.

To observe the transient diffusion behavior the conversion process was investigated at lower temperatures. The expected distribution of Mn for the semi-infinite medium solution at T=600°C is shown in Figure 7, assuming a diffusion coefficient of $2.7*10^{-12}$ cm^2/s for Mn diffusion orthogonal to the c-axis in an Ar environment. STEM elemental maps for incomplete conversion for different conversion times are shown in Figure 8. We see that at elevated temperatures the conversion is very rapid, and that the expected diffusion profiles are reproduced by the experimental data.

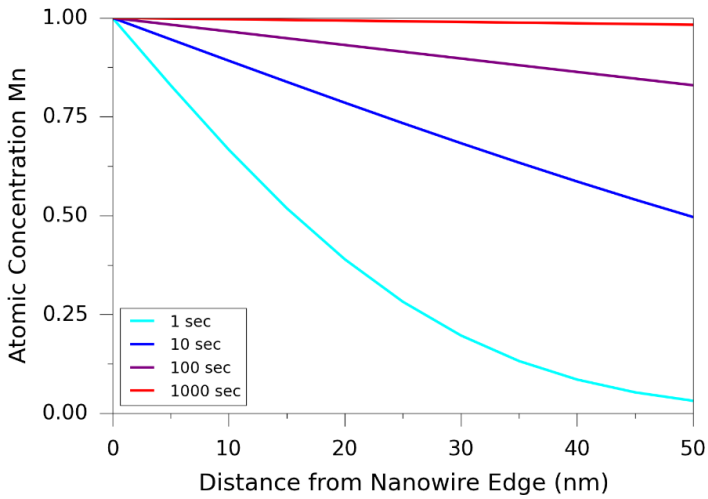

Figure 2.7: Calculated transient diffusion of Mn in TiO_2 nanowires Mn distributions in the TiO_2 nanowire as a function of time for conversion at 600°C in an Ar environment. The nanowire is assumed to be a semi-infinite medium. The nanowire becomes fully converted in a relatively short conversion time.

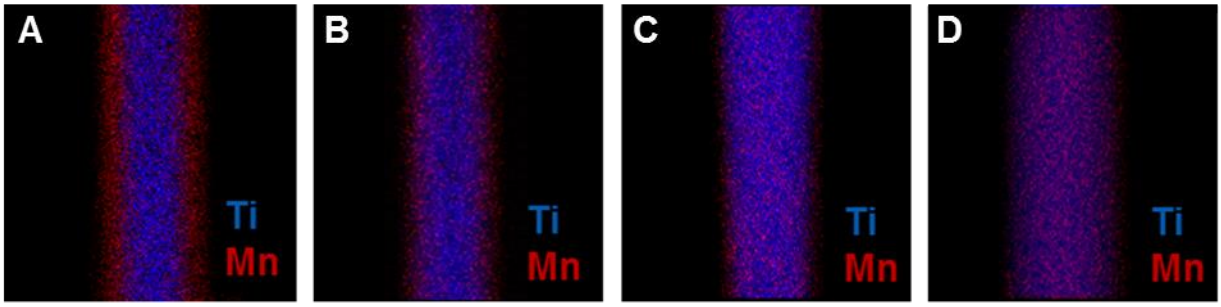

Figure 2.8: Characterization of transient diffusion of Mn in TiO_2 nanowires (A-D) STEM mode EDS elemental maps for transient conversion of nanowire after 0, 1, 10, and 100 min of conversion at 600°C in Ar.

For further insight into the chemical environment and oxidation state of the Mn dopant atoms within the TiO_2 lattice, XPS and X-ray absorption spectroscopy (XANES, EXAFS) were used. XPS was used to study the oxidation state of Mn before and after the conversion process. Assignment of the oxidation state of Mn is not generally possible from the photoelectron peak positions alone, as the binding energies for different oxidation states are quite similar. However, previous studies have shown that comparison of the relative peak position of the $2p_{1/2}$ satellite to its parent peak and the magnitude of the 3s multiplet splitting can be used to determine the oxidation state of manganese.[30-32] The Mn^{2+} oxidation state has a clear satellite peak approximately 6 eV from the parent $2p_{1/2}$ which is absent in the higher oxidation states. Oxides in the higher oxidation states have a weaker peak near 10-11 eV from the $2p_{1/2}$ peak. The multiplet splitting of the 3s peak is also dependent on the oxidation state. An increased oxidation state corresponds to fewer unpaired 3p electrons, leading to a weaker coupling with the unpaired core-level electron formed in the photoionization process, which results in a smaller multiplet splitting. The as deposited film was found to have a $\Delta 2p_{1/2}$ of 10.75 eV and a $\Delta 3s$ of 5.7 eV indicating an average oxidation state between Mn^{3+} and Mn^{4+} as seen in Figure 9. As the metallorganic precursor contains Mn^{2+} cations and surface oxidation of MnO is well known, it is possible that the ALD film deposits in a lower oxidation state and is oxidized in ambient conditions. After annealing, the $\Delta 2p_{1/2}$ was reduced to 6.2 eV and a $\Delta 3s$ of 6.0 eV, matching that of the MnO phase. The annealing process therefore reduces the Mn from a mixed $Mn^{3+/4+}$ valence to a Mn^{2+} oxidation state, possibly due to the formation of oxygen vacancies in the Ar environment. The Ti 2p region of the undoped and doped samples was also investigated, and no change was observed in the binding energies or peak structure.

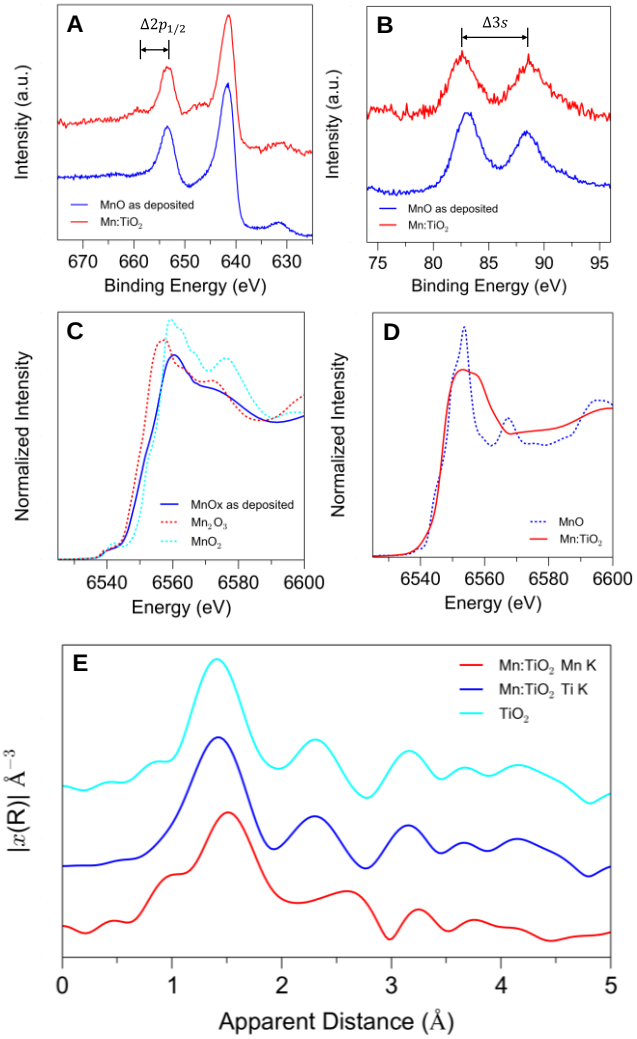

Figure 2.9: Spectroscopic characterization of Mn dopants in TiO_2 nanowires (A,B) XPS spectra of the Mn 2p and 3s regions, indicating the satellite peak distance in the 2p region and the 3s multiplet peak splitting. (C,D) Mn K edge XANES spectra with reference spectra showing the change in Mn valence and fine structure change on annealing. (E) Mn K edge and Ti K edge Fourier Transform EXAFS spectra showing dopant coordination environment.

For further confirmation of the oxidation state of the Mn dopants and determination of their chemical environment within the TiO_2 lattice, near edge and extended X-ray absorption fine structure (XANES, EXAFS) spectroscopy was conducted on the Mn K edge and Ti K edge. The absorption edge position was used to determine the oxidation state, with the position being taken as point of inflection in the absorption edge. The oxidation state was compared with reference samples of Mn^0, Mn^{2+}, Mn^{3+}, and Mn^{4+}. The XANES spectra, as seen in Figure 9, shows the Mn edge energy is 6551.0 eV in the as deposited film indicating the Mn atoms are in a mixed $Mn^{3+/4+}$ oxidation state. The Mn edge energy moves to 6547.5 eV after annealing in Ar corresponding to a reduction of the oxidation state to Mn^{2+}, in agreement with the results of the XPS study. A principal component analysis was performed to fit the experimental spectra with a linear combination of manganese oxide reference samples. The as deposited sample could be described by a linear combination of ~50% Mn_2O_3 and 50% MnO_2, indicating that the chemical environment of the

manganese atoms in the as deposited sample is similar to that in the manganese oxide phases. However, the fine structure of the annealed sample could not be reproduced by the reference spectra, indicating the chemical environment of the Mn in the TiO_2 lattice is quite different to that of the manganese oxide phases, in accordance with the results of the XRD and TEM studies.

The Ti K edge EXAFS spectrum was taken for both the undoped and doped nanowire samples. The nanowires have the rutile structure, in which each Ti atom is octahedrally coordinated and bonded to 6 O atoms. The 6 O atoms are found at two distinct distances of 1.93 and 2.0 Å. The next nearest paths are the Ti-Ti path between the Ti atom at the body center of a rectangular prism and the eight Ti atoms occupying the vertices of the rectangular prism. The effect of the transition metal substitution for Ti should be therefore be seen in the structure of the second and third peaks. However, due to the low concentration of the dopant, the spectra are nearly unchanged, indicating a preservation of the original rutile lattice and a chemical environment for the average Ti atom that is not significantly perturbed by the presence of the Mn dopant. As it is assumed that Mn acts as a substitutional dopant for Ti, the EXAFS spectrum of the dopant taken on the Mn K edge can be qualitatively compared to the Ti K edge EXAFS spectrum, shown in Figure 9. The spectra show clear similarities although the paths dominated by the Mn-O and Mn-Ti bonds appear longer, indicating a structural distortion caused by the larger ionic radius of the Mn^{2+} ion. A fitting of the experimental spectrum was performed using ab initio FEFF calculations, to extract quantitative structural parameters.[21, 22] The structure model used was a rutile cluster with the core atom being replaced with Mn. This structural model provides a good fit to the experimental spectrum, and the bond lengths are observed to be extended, with the Mn-O bonds being 2.03 and 2.15 Å, similar to the Mn-O bond length seen in the Mn^{2+} oxide, and the Mn-Ti path being 3.30 Å.

To evaluate the impact of the Mn doping process on the properties of the nanowires, electrochemical measurements were performed. The electrocatalytic activity of the nanowire substrates for the OER was evaluated across the entire compositional range investigated using cyclic voltammetry in a standard 3-electrode set-up. The relevant figure of merit used for evaluation of electrocatalytic activity for solar water splitting devices is the overpotential required to achieve a current density of 10 mA cm^{-2}.[33] The difference in catalytic activities between different surfaces for the OER is determined by the O* adsorption energy.[34] Rutile TiO_2 lies on the right side of the OER activity volcano, indicating the O* binding is too weak. The introduction of the dopant leads to a stronger interaction between the adsorbate and the surface, resulting in a binding energy nearer the maximum of the activity volcano. The ability to alter the composition while maintaining the original crystal structure allows for access to intermediate binding energies between those of the undoped surface and the dopant in its oxide phase.[18] The overpotential was reduced for all concentrations measured for the converted nanowire substrates (Figure 10a).

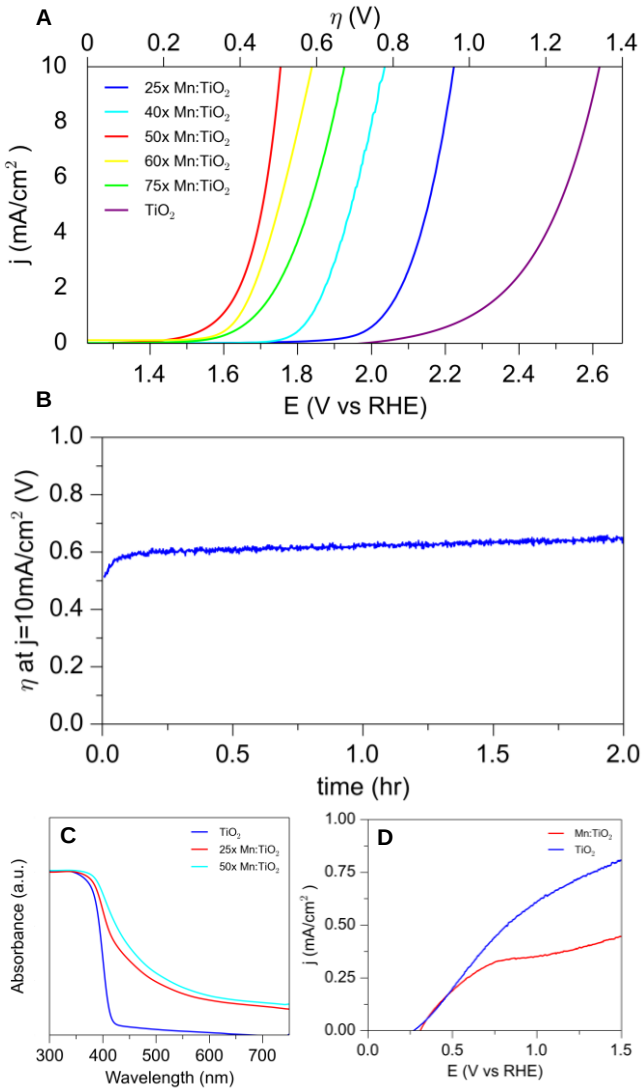

Figure 2.10: Electrochemical characterization of Mn doped TiO_2 nanowires (A) Voltammograms of OER activity for doped and undoped nanowire samples with overpotential required to achieve a benchmark current density of 10 mA/cm^{-2} based on geometric surface area. 25x denotes a sample prepared from 25 cycles of MnO_x ALD. (B) Short term stability test using controlled current electrolysis at 10 mA/cm^{-2} based on geometric surface area. (C) UV-Visible absorption spectra of doped and undoped nanowire samples. (D) Photoelectrochemical performance of undoped and doped nanowire samples using 50x Mn:TiO_2.

The lowest overpotential was measured for Mn:TiO_2 prepared from 50 cycles of ALD, denoted 50x Mn:TiO_2, corresponding to a doping concentration of ~6%, similar to the dopant concentration used for the computational studies of Nørskov and coworkers.[18] It is possible that at higher Mn concentrations the surface becomes too strongly binding. The overpotential required was 0.5 V, or a potential of 1.73 V versus the reversible hydrogen electrode. This value is comparable to previously reported values of 1.77 V and 1.84 V for MnO_x electrocatalysts and ~1.55-1.65 V for high performing electrodeposited catalysts.[24, 33, 35] The improvement observed here is also in agreement with previous studies on transition metal doped TiO_2. The improvement in activity for ~2% dopant concentration relative to the undoped TiO_2 is comparable to that found

by Liu et al, although the current density in the study was limited by the small electrochemically accessible surface area of the submonolayer films.[20] The short term stability of these samples was measured using chronopotentiometry. The catalyst material was held at a constant current density of 10 mA cm^{-2} per geometric area for 2 h while the potential needed to maintain this current density was measured. (Figure 10b) The potential at 2 hours increased to ~1.8 V, indicating the catalyst is relatively stable, in contrast to MnO_x based catalysts, which form MnO_4^- soluble species and dissolve in alkaline conditions and under large applied potentials.[36]

Historically, a variety of transition metals have been explored as dopants in modifying the electronic structure of TiO_2 to improve its visible light photocatalytic activity.[15-17] Previous theoretical studies show that doping TiO_2 with manganese introduces an occupied mid gap state which is very localized and primarily comprised of the Mn t_{2g} orbitals. The visible light absorption in this material is a charge transfer from the dopant mid gap state to the conduction band or an acceptor transition from the valence band to the impurity band.[15] We observe that the doped samples are yellow-brown, departing from the white color of the undoped product. Consequently the light absorption of the Mn doped TiO_2 nanowires extends from the ultraviolet into the visible range as an extended tail, potentially widening the usable range for photocarrier generation for driving the water oxidation reaction. (Figure 10c) It is important to note that the band edge position of the TiO_2 is unchanged, indicating that the tail in the visible range derives mainly from low energy excitations. The mid gap states introduced by the Mn impurity are predicted to be very localized, with little carrier mobility, and could possibly act as recombination centers. The photoelectrochemical performance of the doped TiO_2 films was measured in a 3 electrode set up under simulated solar illumination to determine the effect of the Mn dopant on the photoreactivity. The maximum photocurrent achieved from the doped devices was found to be reduced relative to that of the undoped devices, possibly indicating that the mid gap states formed by the transition metal dopant are acting as recombination centers. (Figure 10d) Although the transition metal doping process allows for visible light absorption, efficient charge collection is required to increase the obtainable photocurrent. This conversion chemistry approach could potentially be applied in such a way that the electronic structure of the light absorber is not negatively affected. This could include the synthesis of ternary metal oxide light absorbers or doping in which the impurity band formed connects with the valence or conduction band allowing for charge carrier extraction. Additionally the ability to precisely tune the composition of mixed metal oxides while maintaining a desired morphology has promise for the development of OER catalysts as demonstrated in this work.

2.5 Conclusions

We have developed a simple and general synthetic method for rationally designing complex metal oxide nanostructures, and demonstrated a novel process for atomic layer deposition of manganese oxide. In this study, we show the utility of this method by investigating the electrocatalytic, optical, and photoelectrochemical properties of Mn doped TiO_2 nanowires as a model system. The Mn dopants are homogeneously incorporated in the rutile TiO_2 lattice without the formation of extraneous crystalline phases. These nanowires show promising electrocatalytic activity for water oxidation, but photoelectrochemical performance of the doped nanowire arrays is negatively affected, possibly owing to the introduction of an impurity band in the band gap of TiO_2. We further demonstrate the generality of this method by extending it to a second

compositional system. Further studies could utilize this simple conversion chemistry approach to investigate functional complex metal oxide nanostructures, such as ternary metal oxide light absorbers or mixed metal oxides for water oxidation electrocatalysis.

2.6 References

1. Dasgupta, N. P.; Sun, J.; Liu, C.; Brittman, S.; Andrews, S. C.; Lim, J.; Gao, H.; Yan, R.; Yang, P. *Adv. Mater.* **2014,** 26, (14), 2137-2184.
2. Liu, C.; Dasgupta, N. P.; Yang, P. *Chem. Mater.* **2014,** 26, (1), 415-422.
3. Warren, E. L.; Atwater, H. A.; Lewis, N. S. *J. Phys. Chem. C* **2014,** 118, (2), 747-759.
4. Liu, C.; Tang, J.; Chen, H. M.; Liu, B.; Yang, P. *Nano Lett.* **2013,** 13, (6), 2989-2992.
5. Boettcher, S. W.; Spurgeon, J. M.; Putnam, M. C.; Warren, E. L.; Turner-Evans, D. B.; Kelzenberg, M. D.; Maiolo, J. R.; Atwater, H. A.; Lewis, N. S. *Science* **2010,** 327, (5962), 185-187.
6. Morales, A. M.; Lieber, C. M. *Science* **1998,** 279, (5348), 208-211.
7. Wu, Y.; Yang, P. *J. Am. Chem. Soc.* **2001,** 123, (13), 3165-3166.
8. Huang, M. H.; Wu, Y.; Feick, H.; Tran, N.; Weber, E.; Yang, P. *Adv. Mater.* **2001,** 13, (2), 113-116.
9. Trentler, T. J.; Hickman, K. M.; Goel, S. C.; Viano, A. M.; Gibbons, P. C.; Buhro, W. E. *Science* **1995,** 270, (5243), 1791-1794.
10. Liu, B.; Aydil, E. S. *J. Am. Chem. Soc.* **2009,** 131, (11), 3985-3990.
11. George, S. M. *Chem. Rev.* **2010,** 110, (1), 111-131.
12. Dasgupta, N. P.; Jung, H. J.; Trejo, O.; McDowell, M. T.; Hryciw, A.; Brongersma, M.; Sinclair, R.; Prinz, F. B. *Nano Lett.* **2011,** 11, (3), 934-940.
13. Dasgupta, N. P.; Liu, C.; Andrews, S.; Prinz, F. B.; Yang, P. *J. Am. Chem. Soc.* **2013,** 135, (35), 12932-12935.
14. Fujishima, A.; Honda, K. *Nature* **1972,** 238, 37.
15. Umebayashi, T.; Yamaki, T.; Itoh, H.; Asai, K. *J. Phys. Chem. Solids* **2002,** 63, (10), 1909-1920.
16. Liu, G.; Wang, L.; Yang, H. G.; Cheng, H.-M.; Lu, G. Q. *J. Mater. Chem.* **2010,** 20, (5), 831-843.
17. Choi, W.; Termin, A.; Hoffmann, M. R. *J. Phys. Chem.* **1994,** 98, (51), 13669-13679.
18. García-Mota, M.; Vojvodic, A.; Metiu, H.; Man, I. C.; Su, H.-Y.; Rossmeisl, J.; Nørskov, J. K. *ChemCatChem* **2011,** 3, (10), 1607-1611.
19. García-Mota, M.; Vojvodic, A.; Abild-Pedersen, F.; Nørskov, J. K. *J. Phys. Chem. C* **2013,** 117, (1), 460-465.
20. Liu, B.; Chen, H. M.; Liu, C.; Andrews, S. C.; Hahn, C.; Yang, P. *J. Am. Chem. Soc.* **2013,** 135, (27), 9995-9998.
21. Newville, M. *J. Synchrotron Radiat.* **2001,** 8, (2), 322-324.
22. Rehr, J. J.; Albers, R. C. *Rev. Mod. Phys.* **2000,** 72, (3), 621-654.
23. Burton, B. B.; Fabreguette, F. H.; George, S. M. *Thin Solid Films* **2009,** 517, (19), 5658-5665.
24. Pickrahn, K. L.; Park, S. W.; Gorlin, Y.; Lee, H.-B.-R.; Jaramillo, T. F.; Bent, S. F. *Adv. Energy Mater.* **2012,** 2, (10), 1269-1277.

25. Strandwitz, N. C.; Comstock, D. J.; Grimm, R. L.; Nichols-Nielander, A. C.; Elam, J.; Lewis, N. S. *J. Phys. Chem. C* **2013,** 117, (10), 4931-4936.
26. Lim, B. S.; Rahtu, A.; Park, J.-S.; Gordon, R. G. *Inorg. Chem.* **2003,** 42, (24), 7951-7958.
27. Lim, B. S.; Rahtu, A.; Gordon, R. G. *Nat. Mater.* **2003,** 2, 749.
28. Au, Y.; Lin, Y.; Kim, H.; Beh, E.; Liu, Y.; Gordon, R. G. *J. Electrochem. Soc.* **2010,** 157, (6), D341-D345.
29. Sasaki, J.; Peterson, N. L.; Hoshino, K. *J. Phys. Chem. Solids* **1985,** 46, (11), 1267-1283.
30. Oku, M.; Hirokawa, K.; Ikeda, S. *J. Electron Spectrosc. Relat. Phenom.* **1975,** 7, (5), 465-473.
31. Di Castro, V.; Polzonetti, G. *J. Electron Spectrosc. Relat. Phenom.* **1989,** 48, (1), 117-123.
32. Gorlin, Y.; Jaramillo, T. F. *ECS Trans.* **2011,** 41, (1), 1701-1707.
33. McCrory, C. C. L.; Jung, S.; Peters, J. C.; Jaramillo, T. F. *J. Am. Chem. Soc.* **2013,** 135, (45), 16977-16987.
34. Man, I. C.; Su, H.-Y.; Calle-Vallejo, F.; Hansen, H. A.; Martínez, J. I.; Inoglu, N. G.; Kitchin, J.; Jaramillo, T. F.; Nørskov, J. K.; Rossmeisl, J. *ChemCatChem* **2011,** 3, (7), 1159-1165.
35. Gorlin, Y.; Jaramillo, T. F. *J. Am. Chem. Soc.* **2010,** 132, (39), 13612-13614.
36. Su, H.-Y.; Gorlin, Y.; Man, I. C.; Calle-Vallejo, F.; Norskov, J. K.; Jaramillo, T. F.; Rossmeisl, J. *Phys. Chem. Chem. Phys.* **2012,** 14, (40), 14010-14022.

Chapter 3

TiO_2|$BiVO_4$ Nanowire Heterostructure Photoanodes based on Type II Band Alignment

This chapter contains material from the following publication:
Resasco, J.; Zhang, H.; Kornienko, N.; Becknell, N.; Lee, H.; Guo, J.; Briseno, A.L.; Yang, P. *ACS Cent. Sci.* **2016,** 2, 80-88.

3.1 Abstract

Metal oxides that absorb visible light are attractive for use as photoanodes in photoelectrosynthetic cells. However, their performance is often limited by poor charge carrier transport. We show that this problem can be addressed by using separate materials for light absorption and carrier transport. Here, we report a Ta:TiO_2|$BiVO_4$ nanowire photoanode, in which $BiVO_4$ acts as a visible light-absorber and Ta:TiO_2 acts as a high surface area electron conductor. Electrochemical and spectroscopic measurements provide experimental evidence for the type II band alignment necessary for favorable electron transfer from $BiVO_4$ to TiO_2. The host−guest nanowire architecture presented here allows for simultaneously high light absorption and carrier collection efficiency, with an onset of anodic photocurrent near 0.2 V vs RHE, and a photocurrent density of 2.1 mA/cm^2 at 1.23 V vs RHE.

3.2 Introduction

Harnessing energy from sunlight is a means of meeting the large global energy demand in a cost effective and environmentally benign manner. However, to provide constant and stable power on demand, it is necessary to convert sunlight into an energy storage medium.[1] An example of such a method is the production of hydrogen by photoelectrochemical (PEC) water splitting. The direct splitting of water can be achieved using a single semiconductor, however, due to the voltage requirement of the water splitting reaction and the associated kinetic overpotentials, only

wide band-gap materials can perform overall water splitting, limiting the efficiency due to insufficient light absorption.[2] To address this issue, a dual-band-gap z-scheme system can be utilized, with a semiconductor photoanode and photocathode to perform the respective oxidation and reduction reactions.[3] This approach allows for the use of lower-band-gap materials that can absorb complementary portions of the solar spectrum and yield higher solar-to-fuel efficiencies.[4, 5] In this integrated system, the charge flux is matched in both light absorbers of the photoelectrochemical cell. Therefore, the overall performance is determined by the limiting component. In most photoelectro-synthetic cells, this limiting component is the semiconductor photoanode.[6]

Metal oxides have been heavily researched as photoanode materials since few conventional light absorber materials are stable at the highly oxidizing conditions required for water oxidation.[7] However, the most commonly studied binary oxide, TiO_2, has a band-gap that is too large to absorb sunlight efficiently (~3.0 eV), consequently limiting its achievable photocurrent.[8] While promising work has recently been done on stabilizing conventional light absorbers such as Si,[9] GaAs,[10] and InP,[11] the photovoltage obtained by these materials thus far has been insufficient to match with smaller band gap photocathode materials such as Si and InP in a dual absorber photoelectro-synthetic cell.[12, 13] Additionally, these materials have high production and processing costs. Small band gap metal oxides that absorb visible light and can be inexpensively synthesized, such as WO_3, Fe_2O_3, and $BiVO_4$, are alternative materials that hold promise to overcome these limitations.[14-16] Among these metal oxides, $BiVO_4$ has emerged as one of the most promising materials due to its relatively small optical band gap of ~2.5 eV and its negative conduction band edge (~0 V versus RHE).[17, 18] Under Air-Mass 1.5 Global (AM1.5G) solar illumination, the maximum achievable photocurrent for water oxidation using $BiVO_4$ is ~7 mA/cm^2.[16] However, the water oxidation photocurrent obtained in practice for $BiVO_4$ is substantially lower than this value, mainly due to poor carrier transport properties, with electron diffusion lengths shorter than the film thickness necessary to absorb a substantial fraction of light.[17]

One approach for addressing this problem is to use two separate materials for the tasks of light absorption and carrier transport. To maximize performance, a conductive and high surface area support material ("host") is used, which is coated with a highly dispersed visible light absorber ("guest"). This architecture allows for efficient use of absorbed photons due to the proximity of the semiconductor liquid junction (SCLJ). This strategy has been employed in dye sensitized (DSSC) and quantum dot sensitized solar cells (QDSSC).[19, 20] Using a host-guest scheme can improve the performance of photoabsorbing materials with poor carrier transport but relies upon appropriate band alignment between the host and guest. Namely, the electron affinity of the host should be larger, to favor electron transfer from guest to host without causing a significant loss in open-circuit voltage.[21] Nanowire arrays provide several advantages for use as the host material as they allow high surface area loading of the guest material, enhanced light scattering for improved absorption, and one-dimensional electron transport to the back electrode.[22] Therefore, nanowire arrays have been used as host materials in DSSCs, QDSSCs, and hybrid perovskite solar cells.[23-25] In photoelectro-synthetic cells, host-guest architectures have been utilized for oxide photoanodes such as $Fe_2O_3|TiSi_2$,[26] $Fe_2O_3|WO_3$,[27] $Fe_2O_3|SnO_2$,[28] and $Fe_2TiO_5|TiO_2$.[29] For $BiVO_4$, it has been studied primarily with $WO_3|BiVO_4$ [30-32], $ZnO|BiVO_4$ [33], and anatase $TiO_2|BiVO_4$.[34] While attractive for its electronic transport properties, ZnO is unstable in aqueous environments, and WO_3 has the disadvantage of having a relatively positive flatband potential (~0.4 V vs RHE)[14]

resulting in potential energy losses for electrons as they are transferred from $BiVO_4$ to WO_3, thereby limiting the photovoltage of the combined system. Performance in the low potential region is critical for obtaining high efficiency in photoelectrosynthetic cells when coupled to typical p-type photocathode materials such as Si or InP.[12, 13] TiO_2 is both stable in a wide range of pH and has a relatively negative flat band potential (~0.2 V vs RHE)[7] which does not significantly limit the photovoltage obtainable from $BiVO_4$, while still providing a driving force for electron transfer. While TiO_2 has intrinsically low mobility, doping TiO_2 with donor type defects could increase the carrier concentration and thus the conductivity. Indeed, niobium and tantalum doped TiO_2 have recently been investigated as potential transparent conductive oxide (TCO) materials.[35, 36] A host material with high carrier concentration could also ensure low contact resistance with the guest material.[37]

Using a solid state diffusion approach based on atomic layer deposition (ALD), we have previously demonstrated the ability to controllably and uniformly dope TiO_2.[38] In this study we demonstrate a host-guest approach using Ta-doped TiO_2 (Ta:TiO_2) nanowires as a host and $BiVO_4$ as a guest material. This host-guest nanowire architecture allows for simultaneously high light absorption and carrier collection efficiency, with an onset of anodic photocurrent near 0.2 V vs RHE, and a photocurrent of 2.1 mA/cm^2 at 1.23 V vs RHE. We show that the synergistic effect of the host-guest structure results in higher performance than either pure TiO_2 or $BiVO_4$. We also experimentally demonstrate thermodynamically favorable band alignment between TiO_2 and $BiVO_4$ using spectroscopic and electrochemical methods, and study the band edge electronic structure of the TiO_2 and $BiVO_4$ using X-ray absorption and emission spectroscopies.

3.3 Experimental methods

3.3.1 Synthesis of titanium dioxide nanowire arrays

Similarly to discussed in Chapter 2, titanium dioxide (TiO_2) nanowires were synthesized by a hydrothermal method.[39] In a typical synthesis, 83 μL of titanium isopropoxide was mixed with 5 mL of 6M hydrochloric acid in a 40 mL Teflon vessel. A fluorine-doped tin oxide (FTO) coated glass substrate was angled against the wall of the Teflon vessel such that the FTO surface was facing down. The Teflon vessel was loaded in a stainless steel autoclave and heated to 180°C for 180 min. After cooling, the substrates were thoroughly rinsed in deionized water. Following growth, the substrates were annealed in a tube furnace in air at 450°C for 30 min following a 30 min ramp from room temperature. The substrates were allowed to cool, after which a 20 nm TiO_2 layer was deposited on the nanowire arrays by ALD.

3.3.2 Atomic layer deposition

Deposition of Ta_2O_5 thin films was performed in a customized thermal ALD reactor. The precursors used for Ta_2O_5 deposition were pentakis(dimethylamido)tantalum (Strem purity 99%) and water.[40] The tantalum precursor was held in a stainless steel cylinder, which was maintained at 105 °C. The water source was maintained at room temperature. The substrate temperature for Ta_2O_5 deposition was 150°C. Typical pulse times for the tantalum precursor and water were 2.0 and 1.0 sec, respectively. The precursors used for TiO_2 deposition were titanium(IV)chloride and

water. The titanium precursor and the water source were both maintained at room temperature. The substrate temperature for TiO_2 deposition was 300°C. Typical pulse times for the titanium precursor and water were 0.2 and 0.1 sec, respectively. Nitrogen was used as a carrier and purge gas in both processes at a flow rate of 10 sccm.

3.3.3 Conversion process

Similarly to discussed in Chapter 2, after the ALD process, the nanowire substrates were loaded into the center of a 1-inch diameter quartz tube and heated in a tube furnace under an Ar atmosphere at 823 K for 12 hrs.[38]

3.3.4 Synthesis of bismuth vanadate

A home-built thermal evaporation system was used to deposit varying amounts of Bi metal as measured by the film thickness of evaporated metal incident on a quartz crystal monitor. To convert the Bi metal to $BiVO_4$, ~50 μL/cm^2 of dimethyl sulfoxide (DMSO) containing 150 mM vanadyl acetylacetonate ($VO(C_5H_7O_2)_2$) was dropcast onto the Bi coated TiO_2 samples to fully cover their surface. The samples were then heated to 450 °C for 2 h in air following a ramp from room temperature at a rate of ~1.8 °C/min. During heating, Bi metal and VO^{2+} ions oxidize and react to form $BiVO_4$. An excess of the vanadium source is used to ensure complete conversion of Bi to $BiVO_4$. Excess V_2O_5 formed during heating can be removed by soaking samples in 1 M KOH solution for 30 min.[41]

3.3.5 Physical and chemical characterization

The morphology of the nanowire substrates was studied using scanning electron microscopy. SEM images were collected using a Zeiss Gemini Ultra-55 Analytical Field Emission Scanning Electron Microscope operating at 10 kV. Phase information was obtained using XRD. XRD patterns were collected using a Bruker D8 Advance diffractometer with Cu Kα radiation. Individual nanowires were imaged by transmission electron microscopy (TEM) using a JEOL 2100-F Field-Emission Analytical TEM operated at 200 kV equipped with an analytical pole piece, a high solid-angle EDS system, and a HAADF (high-angle annular dark field) scanning TEM (STEM) detector. Chemical information was investigated using X-ray photoelectron spectroscopy (XPS). XPS spectra were collected using a PHI 5400 X-ray Photoelectron Spectrometer equipped with a 4 kV Argon ion gun, with Al Kα radiation. The angle between the source and detector was 35°. The measurement chamber was maintained at ~10^{-9} torr during measurement, and measurements were taken at a pass energy of 17.9 eV. All energies were calibrated to spurious carbon at 284.6 eV. Ultraviolet photoelectron spectroscopy measurements were carried out on Omicron SPHERA spectrometer with a He discharge lamp (He I line, 21.22 eV) as the excitation source. To ensure the secondary electron cutoff was captured, a sample bias of −3 V was applied to compensate for the instrument work function difference repelling low-kinetic energy electrons. The base pressure of the analyzer chamber was below 6×10^{-9} torr. APXPS and XPS experiments are performed at Beamline 9.3.2 of the Advanced Light Source, which employs a differentially pumped electrostatic lens system that allows for measurements at pressures on the order of 100 mtorr.[42] Unless otherwise noted, all photoelectron spectra were recorded at photon energies of 490 eV. XAS, XES, and RIXS measurements were performed at beamline 8.0.1 of the Advanced Light Source (ALS) at Lawrence Berkeley National Laboratory (LBNL). Absorption data were collected in total electron yield (TEY), total fluorescence yield (TFY), and partial fluorescence yield (PFY).

The resolution for XAS spectra was better than 0.15 eV at the O K-edge. The spectra were normalized to the incident photon flux monitored by measuring the photocurrent from a clean gold mesh. The instrumental resolution for X-ray emission was 0.4 eV, and the emission energy was calibrated using the positions of the elastic features in the emission spectra.

3.3.6 Electrochemical characterization

Electrochemical properties of the nanowire samples were studied in a three-electrode electrochemical cell using a Bio-Logic potentiostat/galvanostat with a built-in electrochemical impedance spectroscopy (EIS) analyzer. Unless otherwise noted, all measurements were performed at room temperature in 0.5 M potassium phosphate electrolyte buffered to pH 7, using a platinum wire counter electrode and a Ag/AgCl reference electrode. The potential scale was calibrated to a reversible hydrogen electrode. A 300-Watt Xe lamp equipped with an air mass 1.5G filter (Newport) was used as the light source. Prior to measurement, light intensity was standardized using a calibrated silicon photodiode. For IPCE measurements, light from the xenon lamp was dispersed by a monochromator (Newport Corp.), and the photocurrent was recorded at a constant bias with a spectral step of 10 nm. The measured photocurrent was converted to IPCE by normalizing to a standard photodiode with a known quantum efficiency.

3.4 Results and discussion

3.4.1 Development of a nanowire heterostructured photoanode

A schematic of the desired host-guest structure is shown in Figure 1, in which a high surface area TiO_2 nanowire array is used as an electron conductor, and small, highly dispersed $BiVO_4$ nanoparticles coat the surface as visible light sensitizers. The small size of these nanoparticles allows high collection efficiency of electrons by the nanowires, and the proximity of the semiconductor liquid junction allows holes to reach the surface to perform the water oxidation reaction. The Type II band alignment required for electron transfer between TiO_2 and $BiVO_4$ is illustrated, in which electrons produced by photoexcitation in $BiVO_4$ are transferred to the conduction band of TiO_2. Additionally, holes produced in TiO_2 can move through the valence band of $BiVO_4$ and to the semiconductor surface to oxidize water. Scanning electron microscopy (SEM) images of the as-grown nanowire arrays and the optimized Type II photoanode heterostructures are shown in Figure 1b,c. The following sections discuss the development of these optimized structures.

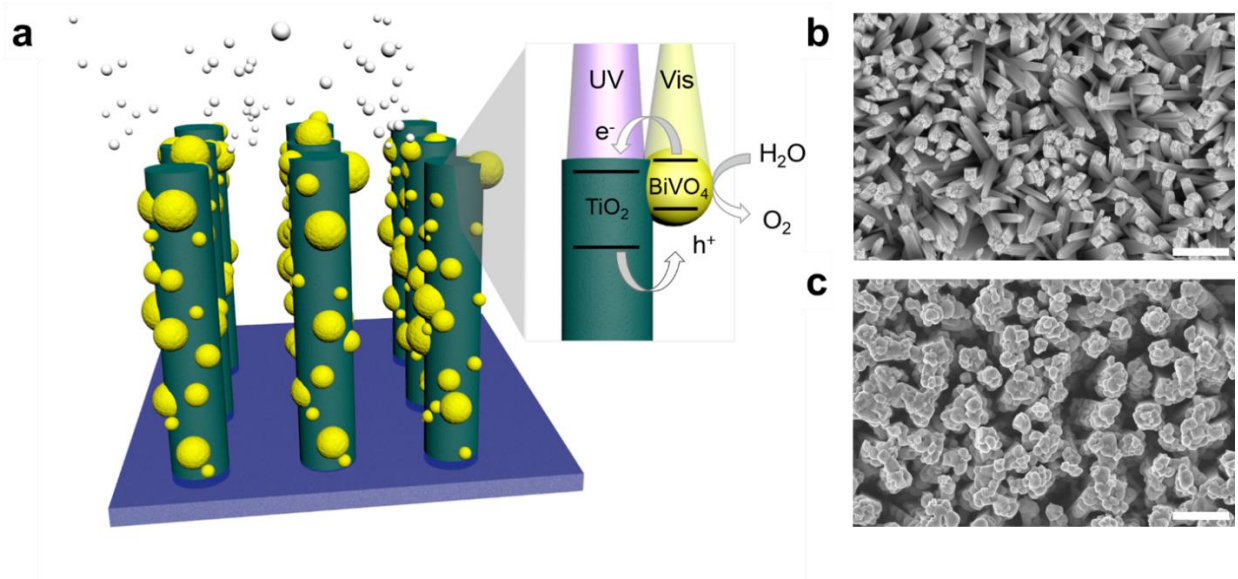

Figure 3.1: Nanowire heterostructure scheme. (a) Schematic of the photoanode architecture. The nanowire morphology provides an increased light absorption path for visible photons by $BiVO_4$ and a pathway for efficient electron transfer while maintaining the proximity of the semiconductor liquid junction for holes to carry out the oxygen evolution reaction. Type II band alignment allows electron transfer from $BiVO_4$ to TiO_2.(b,c) SEM images of designed nanowire heterostructure before and after $BiVO_4$ loading. Scale bar 500 nm.

3.4.2 Synthesis of Ta:TiO_2 conductive nanowire scaffolds

To provide a high surface area scaffold for the $BiVO_4$, rutile TiO_2 nanowire arrays were grown on glass substrates coated with fluorine-doped tin oxide (FTO) by using a hydrothermal method.[39] High resolution transmission electron microscopy (HRTEM) analysis demonstrated that the nanowires are single crystalline and grow along the [001] direction (Figure 2). The nanowires are ~2.0 μm in length and 150 nm in diameter. Again, for use as an electron transporting scaffold, the carrier concentration of the TiO_2 nanowires must be increased. This can be accomplished by doping with Ta^{5+} , which acts as a donor defect when occupying substitutional Ti^{4+} sites.[35] Previously, synthesis of transparent conductive oxides with resistivities of ~2.5×10^{-4} Ω cm have been demonstrated using Ta- and Nb-doped anatase TiO_2 compared to resistivities of ~1×10^{-1} Ω cm for undoped TiO_2.[35, 36] Following a previously developed solid state diffusion method,[38] the doping was accomplished by forming a core-shell $TiO_2|Ta_2O_5$ structure using ALD, followed by high temperature annealing. ALD of Ta_2O_5 was performed using pentakis (dimethylamino)tantalum and water.[40]

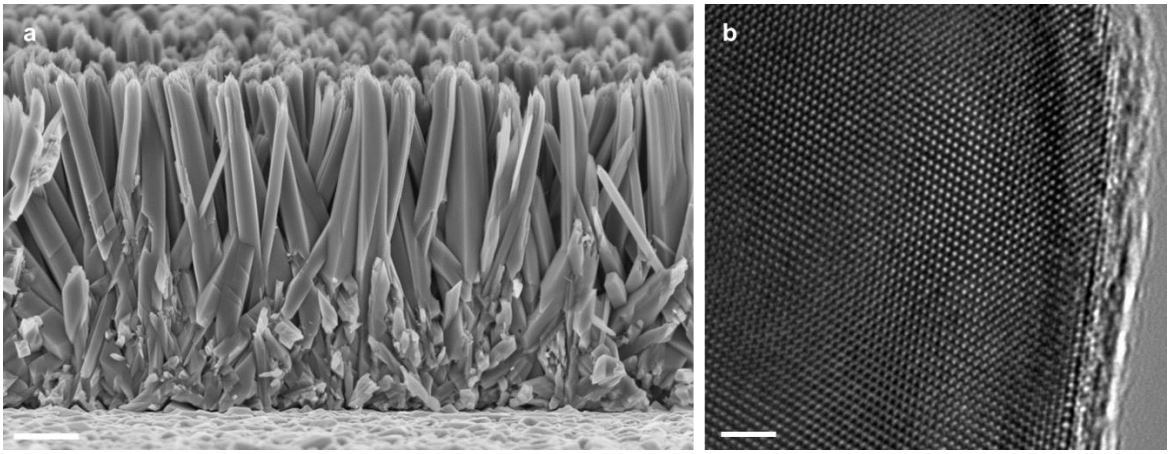

Figure 3.2: Characterization of TiO_2 nanowires (a) Cross-sectional SEM of TiO_2 nanowires (b) HRTEM of TiO_2 nanowires consistent with a single crystal rutile TiO_2 structure and c-axis growth direction.

Two important characteristics of an ALD reaction are the saturation of the surface reaction after each precursor pulse, and a linear relationship between film thickness and number of cycles after a sufficient number of cycles.[43] To measure film thicknesses, ALD Ta_2O_5 was deposited on planar Si substrates and measured by ellipsometry. Saturating, linear growth was demonstrated indicating an ALD growth mode with a growth rate of ~0.6 Å/cycle. Using X-ray photoelectron spectroscopy (XPS), no measurable carbon or nitrogen was observed in the spectrum following 1 min of Ar sputtering. Because the ligands of the Ta precursor contain carbon and nitrogen, the lack of any organic contamination in the film indicates that the ALD surface reaction was complete, and the ligands were completely substituted by oxygen from the H_2O precursor pulse. The TiO_2 nanowire arrays were coated with tantalum oxide using ALD producing conformal core–shell nanowires with uniform shell thicknesses that could be tuned with sub-nanometer precision. Characterization of the ALD process is shown in Figures 3-5.

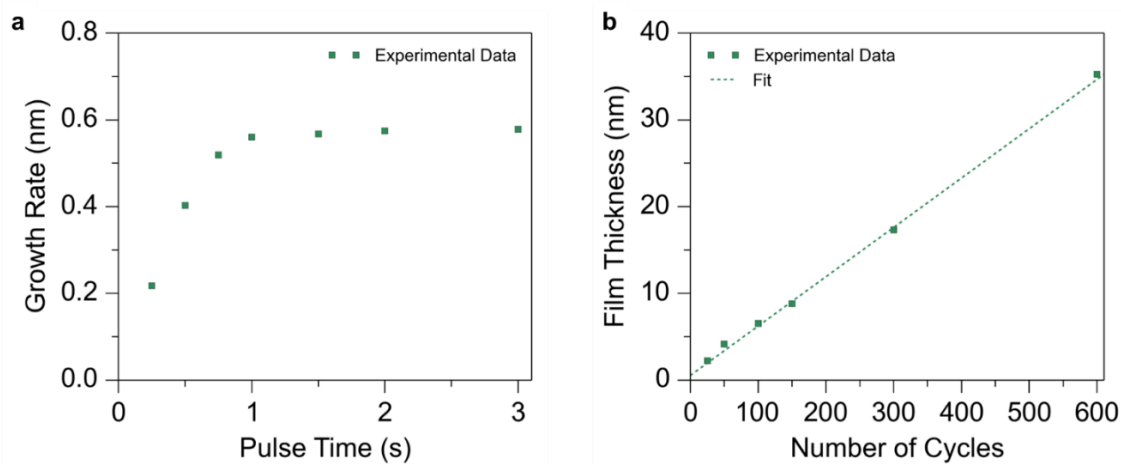

Figure 3.3: Optimization of Ta_2O_5 ALD conditions (a) Growth rate per cycle of Ta_2O_5 ALD films under increasing pulse time of the Ta precursor. Saturation was observed after 1.0 s. (b) Thickness of Ta_2O_5 ALD films measured by ellipsometry as a function of number of cycles. A linear growth rate of ~0.6 Å/cycle was observed.

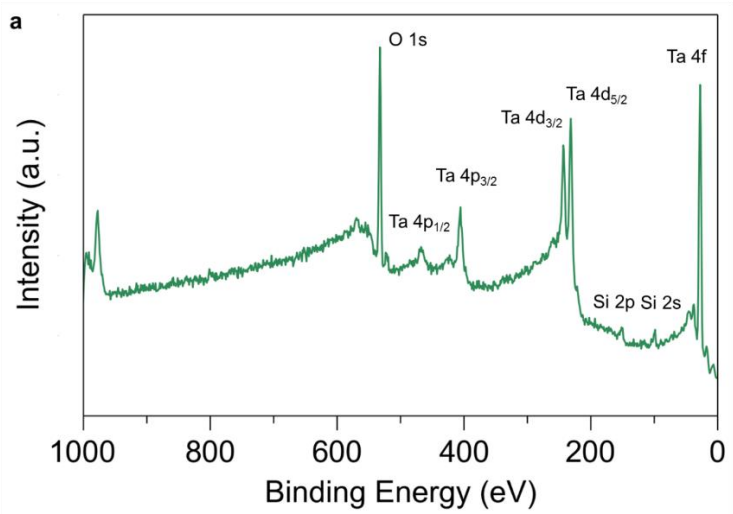

Figure 3.4: X-ray photoelectron spectroscopy of Ta_2O_5 ALD films (a) X-ray photoelectron spectrum of Ta_2O_5 ALD thin film deposited on a Si wafer following a 1 min Ar sputter. The lack of organic contamination signifies complete substitution of ligands by oxygen from the H_2O precursor pulse.

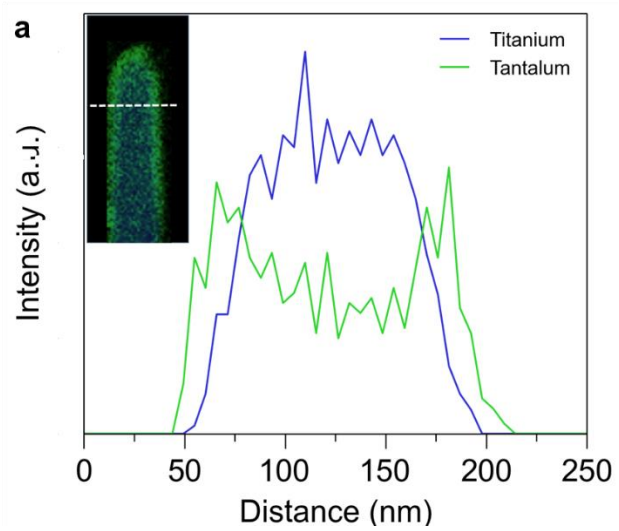

Figure 3.5: Characterization of TiO_2|Ta_2O_5 core-shell nanowires (a) Line scan of TiO_2|Ta_2O_5 core-shell nanowire showing a uniform Ta_2O_5 film coating the high surface area nanowires.

The coated nanowire arrays were then annealed at 600°C in an argon environment to facilitate diffusion of tantalum atoms into the rutile lattice, yielding Ta-doped TiO_2 nanowires. The solid state diffusion process maintains the nanowire morphology and crystallinity as evidenced by X-ray diffraction (XRD) and electron microscopy (Figure 6).

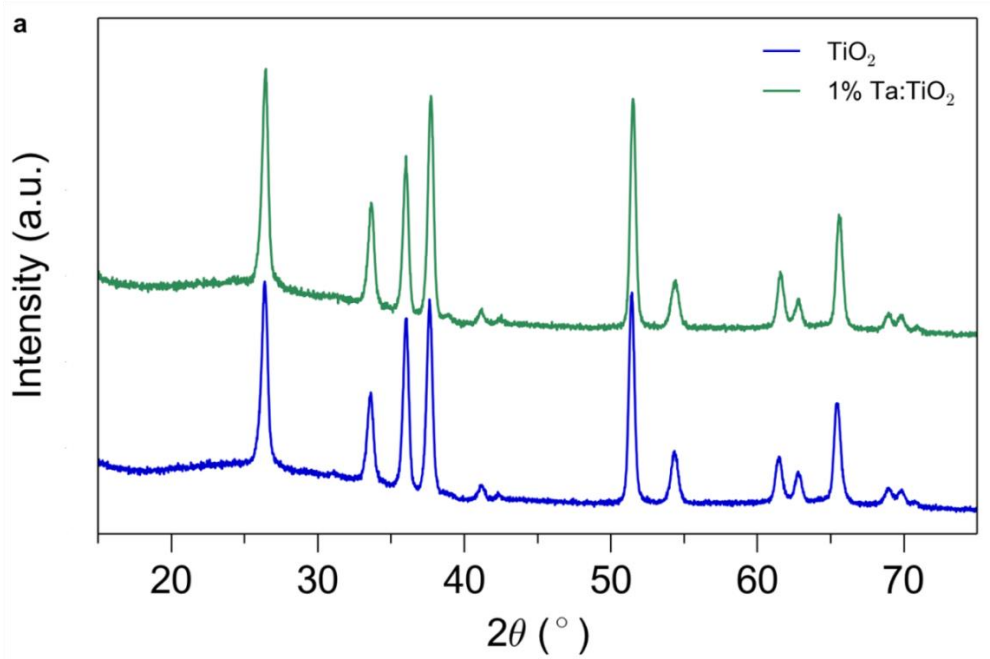

Figure 3.6: X-ray diffraction of TiO_2 and Ta:TiO_2 nanowires (a) X-Ray Diffraction patterns of TiO_2 nanowire samples before and after incorporation of Ta dopants. The crystal structure of the nanowires is unchanged by the doping process.

To confirm the presence of Ta atoms and obtain a visualization of their distribution within the TiO_2 lattice, energy dispersive X-ray spectroscopy (EDS) mapping was conducted using scanning transmission electron microscopy (STEM). The elemental maps show a homogeneous incorporation of the Ta atoms, in contrast with the core–shell nanowires observed prior to annealing (Figure 7). To determine the effect of the Ta doping on the carrier concentration of the nanowires, electrochemical impedance spectroscopy was performed. From the slopes of the Mott–Schottky plots (Figures 2b), carrier densities of undoped and 1% Ta-doped TiO_2 nanowires were estimated to be $\sim 10^{18}$ and $\sim 10^{20}$ cm^{-3}, respectively, using the Mott-Schottky relation:

$$\frac{1}{C_{sc}^2} = \frac{2}{\varepsilon\varepsilon_0 A^2 e N_d}\left(V - V_{fb} - \frac{k_b T}{e}\right)$$

where C_{sc} is the capacitance of the space charge region, e is the elementary charge of an electron, ε_0 is the permittivity of vacuum, ε is the dielectric constant of rutile TiO_2 (ε = 86),[44] A is the electrochemically active surface area, V is the applied voltage, V_{fb} is the flatband potential, and N_d is the donor density.[45] The positive slope indicates n-type behavior of the rutile nanowires. Mott-Schottky plots for varying Ta concentrations showed a monotonic increase in carrier concentration with the amount of Ta (Figure 8).

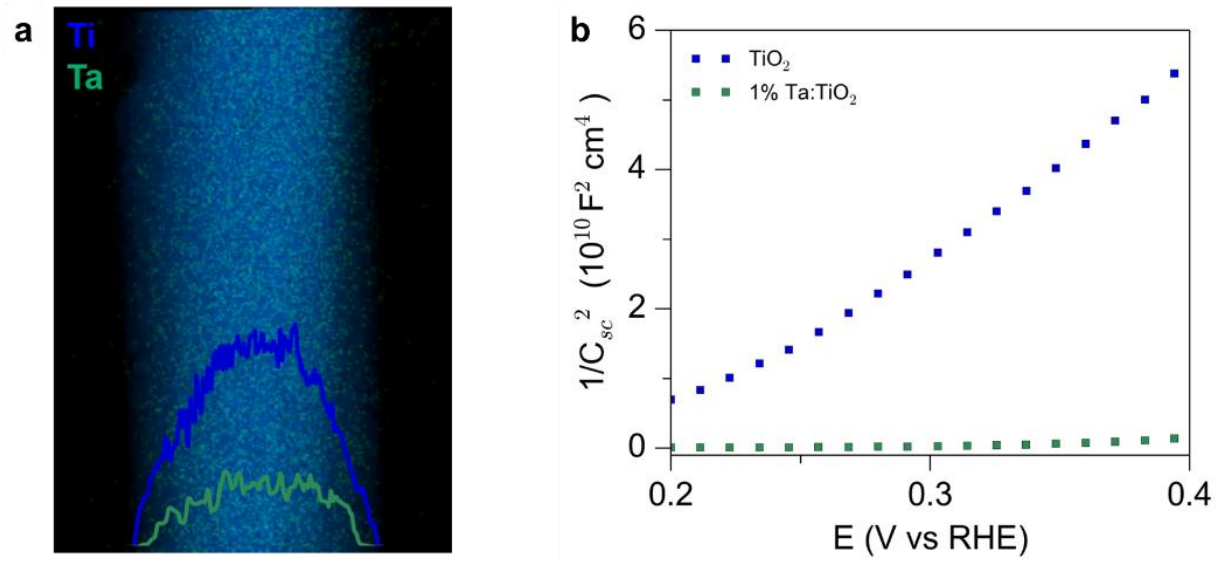

Figure 3.7: Modification of the electronic properties of TiO_2 Nanowires (a) Elemental maps and line scans for Ta:TiO_2 nanowires. Diffusion of Ta yields a uniformly doped nanowire. (b) Mott-Schottky plots of undoped and Ta-doped TiO_2 showing an increase in carrier concentration with doping.

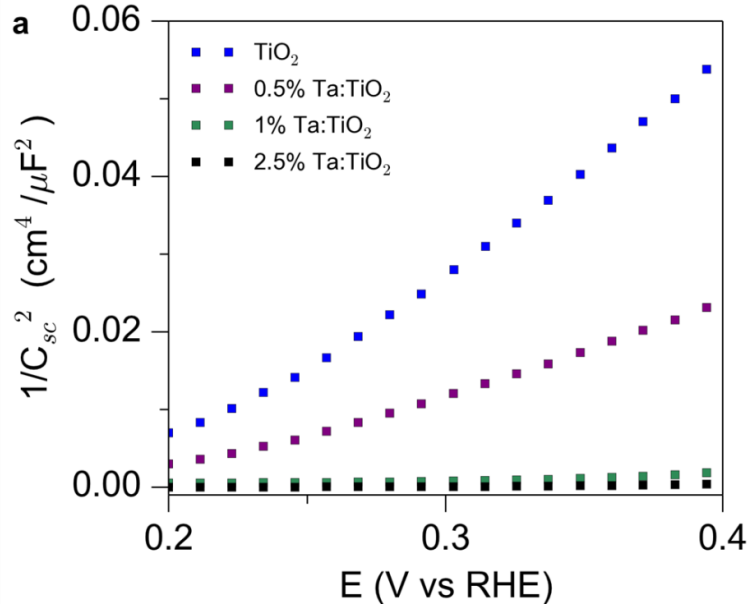

Figure 3.8: Mott-Schottky of Ta:TiO_2 nanowires. Mott-Schottky plots of various levels of Ta doping showing an increase in carrier concentration with increased concentration of Ta.

3.4.3 Coating TiO_2 nanowires with visible light absorber $BiVO_4$

Having obtained a conductive high surface area support, undoped $BiVO_4$ was deposited on the nanowire array by thermal evaporation of Bi metal, followed by heating in the presence of vanadyl acetylacetonate ($VO(C_5H_7O_2)_2$).[41] During heating Bi and VO^{2+} are oxidized and react to form $BiVO_4$. Excess V_2O_5 was dissolved after heating by soaking the substrates in 1M KOH. Based solely on the density of the respective materials, 1 nm of Bi metal is converted to ~2.5 nm of $BiVO_4$. The thermal conversion process yields isolated $BiVO_4$ particles in the size range of 20-100 nm (Figure 10), which is favorable for photoelectrochemical performance due to the short electron diffusion length of $BiVO_4$ (L < 100 nm).[17] The density and size of the $BiVO_4$ particles could be controlled by changing the thickness of the initial Bi seed layer (Figure 10,11). At Bi seed layer thickness greater than a planar equivalent of 100 nm, the nanowire array becomes filled, and $BiVO_4$ that does not infiltrate the array forms a thin film on top of the nanowire array. XRD confirms the monoclinic scheelite $BiVO_4$ phase is formed (Figure 12), and no changes in the original rutile TiO_2 or F:SnO_2 peaks are observed (Figure 9). Elemental mapping also demonstrates that Bi and V signals are observed on the particles and Ti signal is observed on the core of the nanowires (Figure 9b).

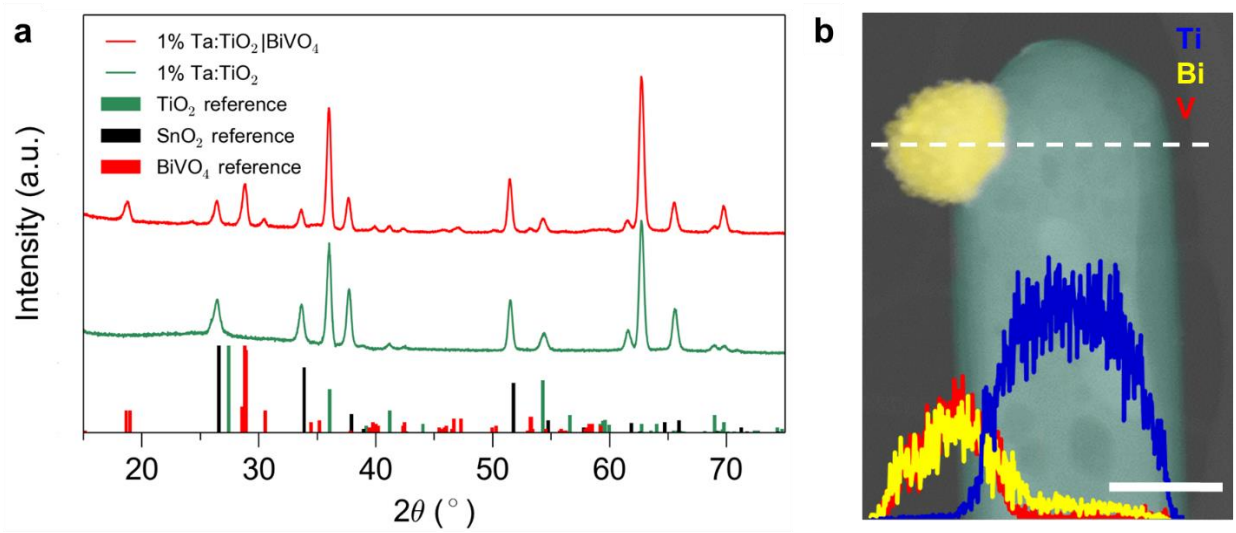

Figure 3.9: Loading of $BiVO_4$ onto TiO_2 (a) XRD patterns for doped TiO_2 nanowire arrays before and after $BiVO_4$ deposition. (b) Elemental mapping of a TiO_2 nanowire decorated with a $BiVO_4$ particle. Scale bar 100 nm.

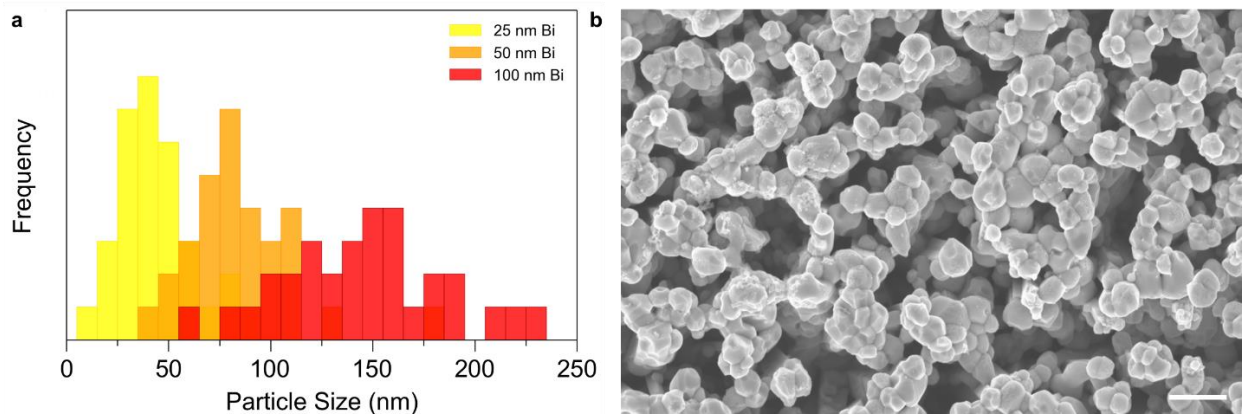

Figure 3.10: Statistic of $BiVO_4$ particle sizes on Ta:TiO_2 nanowires (a,b) Particle size statistics and representative SEM image of Ta:TiO_2|$BiVO_4$ sample with 100 nm Bi planar equivalent loading. Average particle sizes for 25, 50, and 100 nm planar equivalents are 45 nm, 85 nm, and 148 nm, respectively. Scale bar is 500 nm.

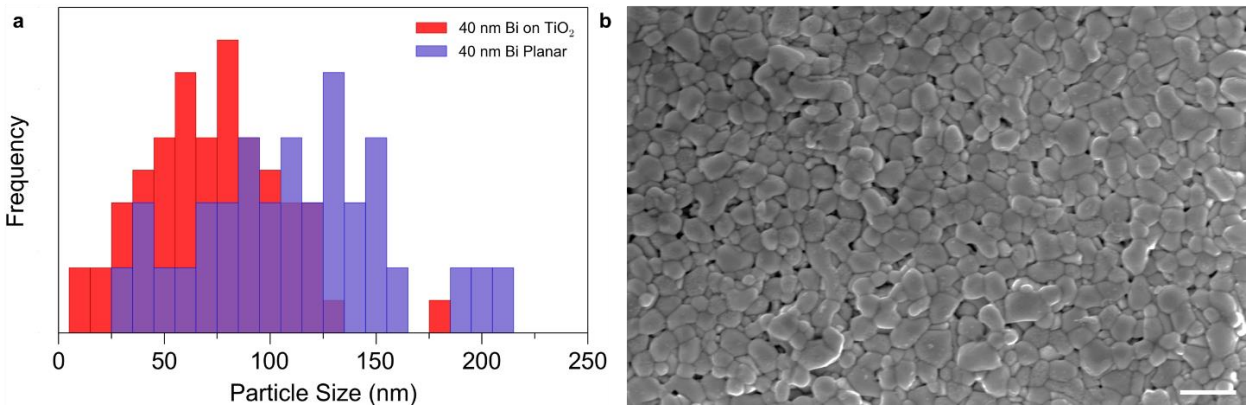

Figure 3.11: Statistics of $BiVO_4$ particle sizes in thin films. (a) Particle size statistics for planar vs nanowire loaded $BiVO_4$. The nanowire array prevents large particle growth. (b) Representative SEM image of a planar $BiVO_4$ sample with 40 nm Bi planar equivalent loading. Average particle sizes for nanowire and planar samples are 72 nm and 117 nm, respectively. Scale bar is 500 nm.

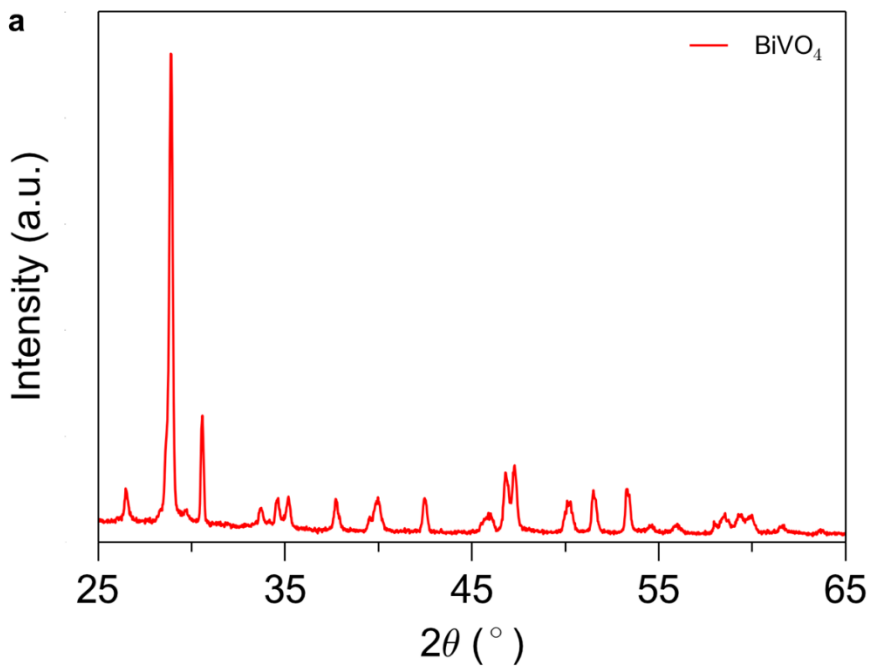

Figure 3.12: Characterization of $BiVO_4$ thin films (a) X-Ray Diffraction patterns of planar $BiVO_4$, showing the diffraction pattern of the monoclinic scheelite $BiVO_4$ phase.

3.4.4 Photoelectrochemistry of nanowire heterostructures

The effect of Ta doping on the photoelectrochemical performance was first investigated without $BiVO_4$ coating by controlling the Ta dopant source via the thickness of the Ta_2O_5 shell. Although series resistance losses are likely decreased due to the higher carrier concentration, the introduction of the Ta dopant is detrimental to the overall performance of the TiO_2 nanowire arrays (Figure 13, 14). As a relatively small fraction of Ta atoms in the rutile structure act as active dopants, it is possible that the high concentration of Ta dopants could result in increased defects in the nanowires and higher rates of carrier recombination. However, when a fixed amount (40 nm planar equivalent Bi seed layer) of $BiVO_4$ is deposited on the wire arrays the doped heterostructures clearly outperform their undoped analogues. Although electron transfer occurs in the desired direction in both cases, undoped TiO_2 coated with $BiVO_4$ actually shows a decrease in performance, possibly indicating that a substantial fraction of charge carriers are lost at the $TiO_2|BiVO_4$ interface (Figure 15). The higher carrier concentration in Ta:TiO_2 could result in a decrease in the depletion width in TiO_2, resulting in improved electron transfer from the $BiVO_4$ to the TiO_2. It is evident that although Ta doping is detrimental to the carrier transport properties of the TiO_2 nanowires, it is necessary to allow favorable electron transfer at the $TiO_2|BiVO_4$ interface. The highest performance was obtained with ~1% Ta doping, which was used for all subsequent measurements for Ta:$TiO_2|BiVO_4$ heterostructures (Figure 14).

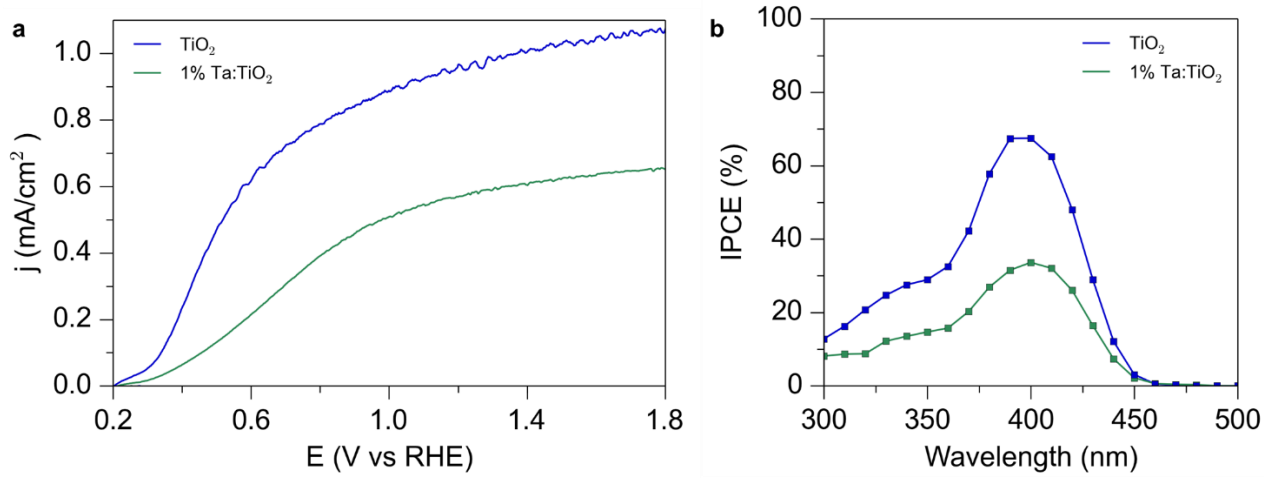

Figure 3.13: Effect of Ta doping on PEC performance (a) Linear sweep voltammograms of TiO_2 and Ta:TiO_2 nanowire samples. Decreased activity for water oxidation is observed after Ta doping. (b) IPCE data for TiO_2 and Ta:TiO_2 nanowire samples.

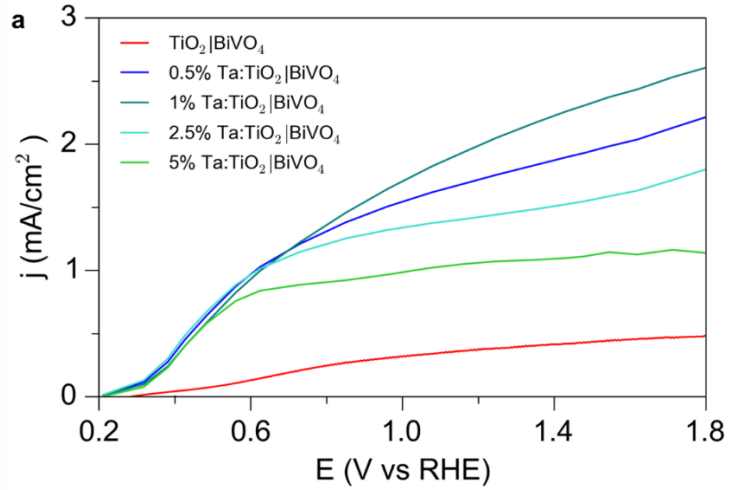

Figure 3.14: Optimization of Ta doping for Ta:TiO_2|$BiVO_4$ (a) Linear sweep voltammograms of TiO_2 and Ta:TiO_2 nanowire samples loaded with 40 nm $BiVO_4$. An optimum in performance is observed for 1% Ta doping.

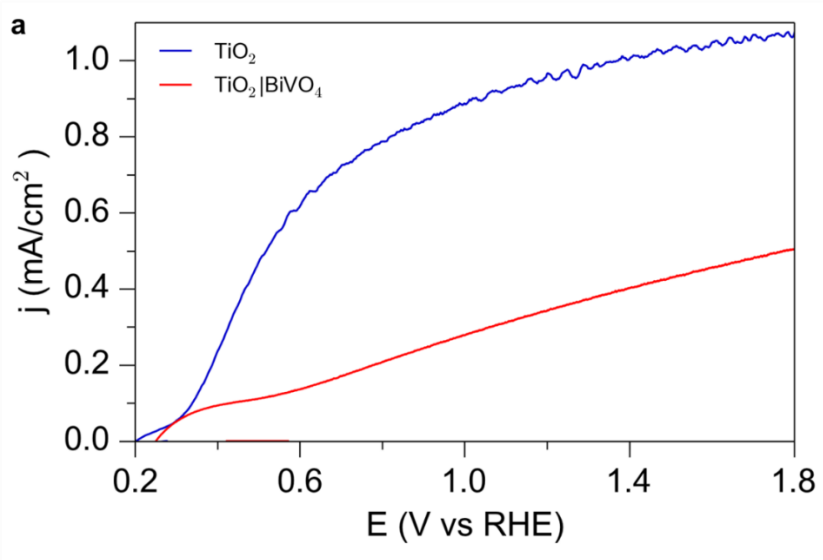

Figure 3.15: PEC performance of TiO_2|$BiVO_4$ nanowire samples (a) Linear sweep voltammograms of TiO_2 and TiO_2|$BiVO_4$ samples. Decreased activity for water oxidation is observed after addition of $BiVO_4$, possibly due to poor electron transport between TiO_2 and $BiVO_4$.

The effect of the $BiVO_4$ loading amount was investigated by controlling the Bi metal seed layer thickness. The addition of the $BiVO_4$ particles extends the absorption of the nanowire structures into the visible light region (Figure 16a). An onset of absorption is observed at ~520 nm, consistent with the 2.5 eV band gap of monoclinic $BiVO_4$ (Figure 17). As the Bi metal thickness is increased from a planar equivalent of 10-50 nm, the absorption in the 400-500 nm region increases, and samples with thickness greater than 40 nm show near unity absorption in this region. This highlights the advantage of the high surface area scaffold, as an identically prepared $BiVO_4$ thin film on FTO shows ~50% absorption at 450 nm. The scaffold also prevents the formation of much larger $BiVO_4$ particles which are detrimental to performance. From voltammetric and incident photon to current efficiency (IPCE) measurements, it can be seen that an optimum thickness exists, with 40 nm Bi thickness having optimal performance. (Figure 16b, 16c, 18) The absorbed photon to current efficiency (APCE) shows similar internal quantum efficiency for low loading amounts, after which the APCE decreases (Figure 19). At higher loadings, the $BiVO_4$ particle sizes become too large and begin to form films that do not penetrate the nanowire array and correspondingly the electron collection efficiency is decreased. The collection efficiency for large particles is particularly low for these undoped $BiVO_4$ nanoparticles. We see that comparatively high APCE values can be obtained for loading amounts which give near unity light absorption. This shows the ability of the host-guest design to decouple light absorption and carrier collection efficiencies, which is not possible with thin film or nanostructured $BiVO_4$ electrodes. However, it is also observed that the APCE values for the $BiVO_4$ deposited on the nanowire arrays is lower than the corresponding thickness of $BiVO_4$ deposited on a FTO substrate. This can be explained by the substantial loss of charge carriers in the TiO_2 nanowire array, due to the defects caused by Ta doping. The higher absorption in the nanowire case compensates this loss in APCE yielding higher activity; however, improving the carrier collection in the nanowire array could result in simultaneously high absorption and collection efficiencies. One potential strategy would be the use of more effective dopants or codopants which have previously been shown to increase the

carrier concentration of TiO_2 nanowires without sacrificing performance.[46, 47] Additionally, the photoelectrochemical performance of the Ta:TiO_2|$BiVO_4$ nanowire photoanodes was investigated in electrolyte containing sodium sulfite (Na_2SO_3), which acts as an efficient hole scavenger. As the efficiency of hole capture by sulfite ions can be assumed to be near unity, measuring photocurrent for sulfite oxidation allows for determination of the photoelectrochemical activity of a photoanode irrespective of its water oxidation kinetics. It is clear that there is a significant difference between the water oxidation and sulfite oxidation photocurrent (Figure 16d), demonstrating that slow kinetics for water oxidation substantially limit the performance of the photoanodes. To address this issue, a cobalt based catalyst was deposited on the Ta:TiO_2|$BiVO_4$ samples by photo-assisted electrodepostion.[48] Cobalt oxides have also shown to have high activity for water oxidation in near neutral pH with near unity charge transfer efficiencies.[49-51] The performance of the Ta:TiO_2|$BiVO_4$ electrodes before and after the deposition of the Co-Pi catalyst are shown in Figure 16d. The performance is greatly enhanced, especially in the low potential region, and the similarity with the performance to sulfite oxidation shows the efficiency of the cobalt catalyst for decreasing surface recombination and improving water oxidation kinetics.

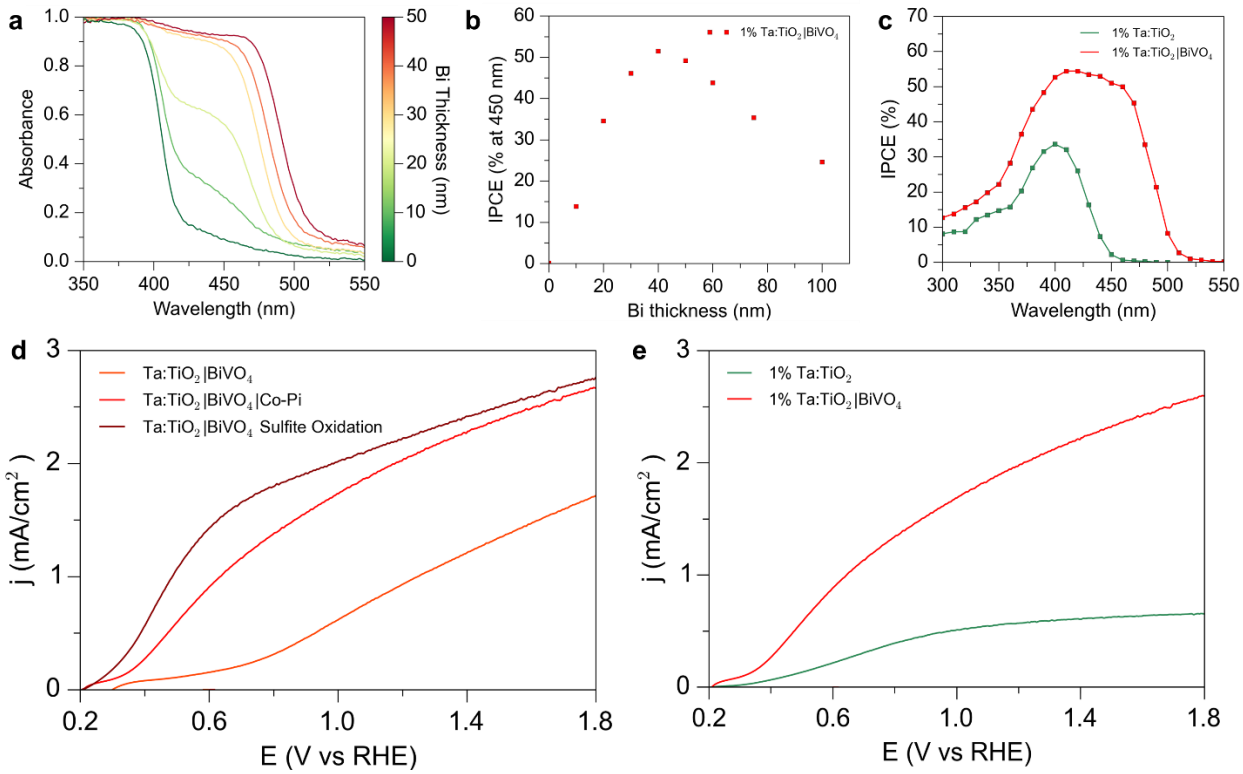

Figure 3.16: Photoelectrochemical performance of the Ta:TiO_2/$BiVO_4$ nanowire heterostructures (a,b) Absorption and IPCE for Ta:TiO_2|$BiVO_4$ samples with increasing loading. Near complete absorption and optimal activity is observed for planar equivalent thickness of 40 nm of Bi. (c) IPCE for Ta:TiO_2 and Ta:TiO_2|$BiVO_4$ showing visible contribution from $BiVO_4$. (d) Current−voltage curves in 0.5 M potassium phosphate electrolyte buffered to pH 7 with and without the presence of a hole scavenger. (b) Current−voltage curves in 0.5 M potassium phosphate electrolyte buffered to pH 7 for Ta:TiO_2 and Ta:TiO_2|$BiVO_4$.

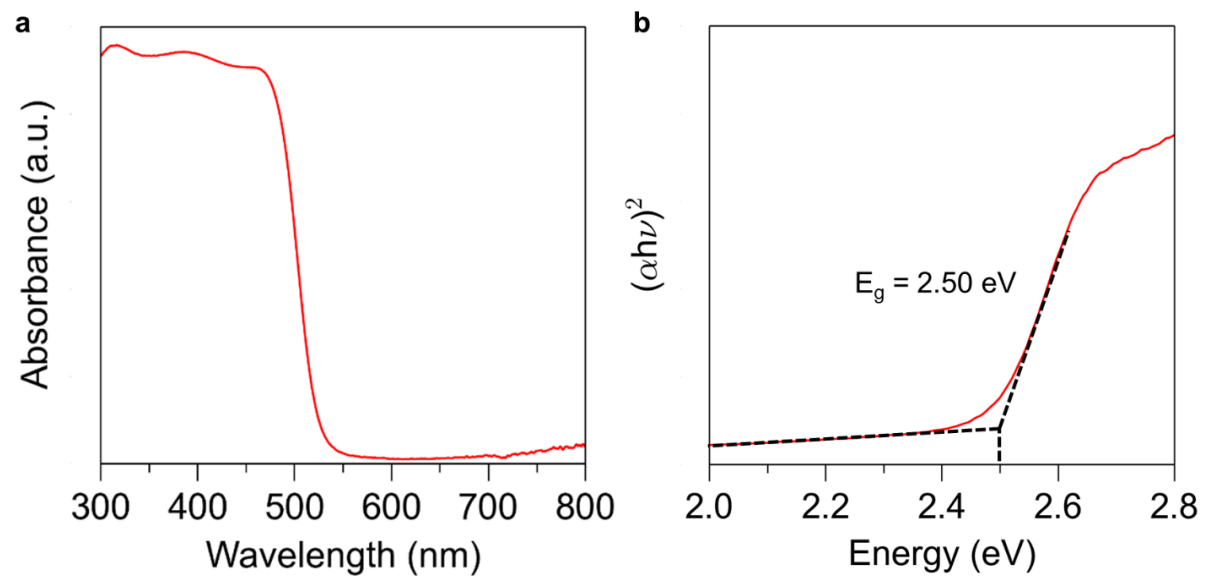

Figure 3.17: Optical characterization of $BiVO_4$ (a) Optical absorption and (b) Tauc plot of a $BiVO_4$ thin film deposited on FTO/glass assuming the optical band gap of $BiVO_4$ is a direct transition.

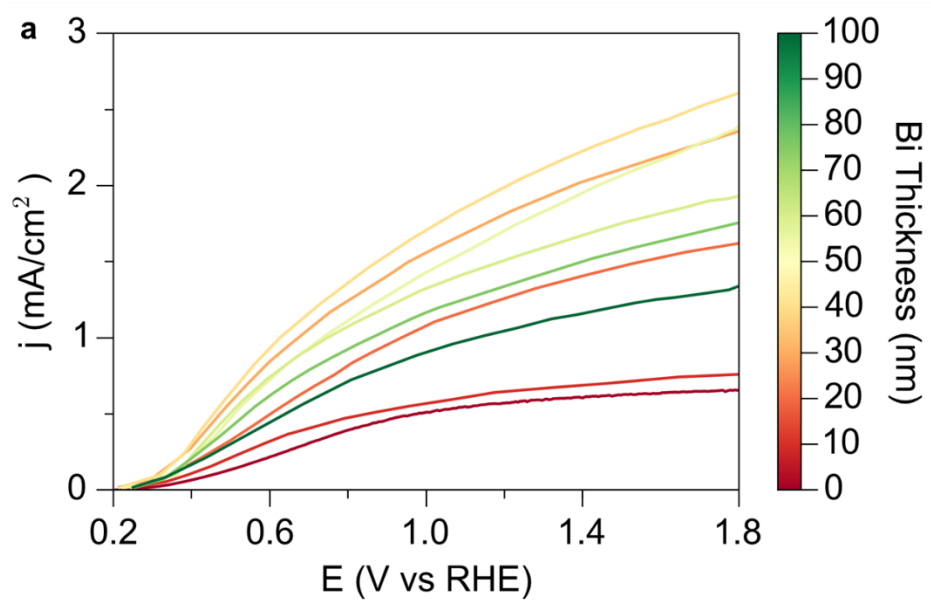

Figure 3.18: Effect of $BiVO_4$ loading on PEC performance. Linear sweep voltammograms of different loadings of $BiVO_4$ on 1% Ta:TiO_2. An optimum is observed for 40 nm Bi.

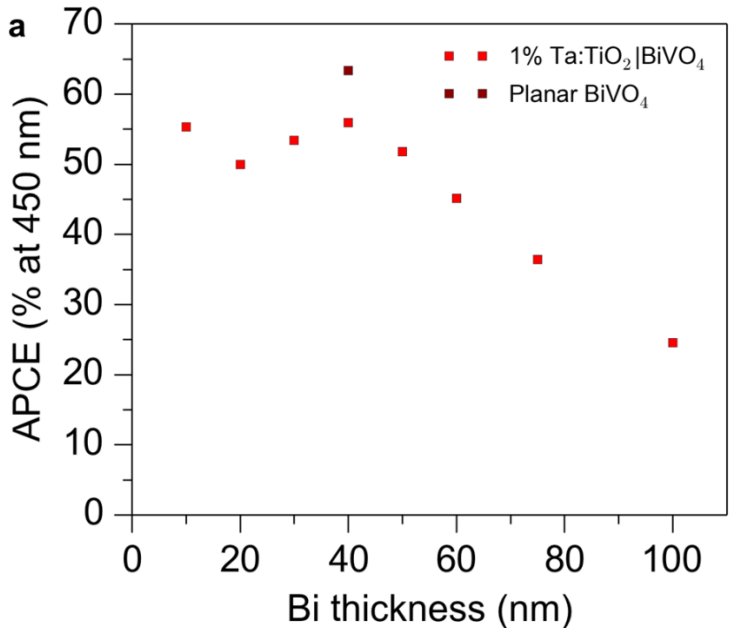

Figure 3.19: APCE data for Ta:TiO_2|$BiVO_4$ and planar $BiVO_4$ (a) APCE for Ta:TiO_2|$BiVO_4$ samples with increasing loading. High APCE values are observed for planar equivalent thickness <60 nm. Planar $BiVO_4$ shows higher APCE than Ta:TiO_2|$BiVO_4$ at equal loading but is limited by insufficient absorption.

The optimized Ta:TiO_2|$BiVO_4$|Co-Pi photoanodes show an onset of photocurrent at a potential near 0.2 V vs RHE, and a photocurrent of 2.1 mA/cm^2 at 1.23 V vs RHE. By comparison, an equal loading of $BiVO_4$|Co-Pi deposited on FTO shows an onset potential of 0.25 V vs RHE and a photocurrent of 1.4 mA/cm^2 at 1.23 V vs RHE. As previously discussed, the planar film is primarily limited by insufficient light absorption, which is substantially increased in the nanowire array. An identically prepared Ta:TiO_2|Co-Pi nanowire array shows an onset potential of 0.25 V vs RHE, and a photocurrent of 0.5 mA/cm^2 at 1.23 V vs RHE. From the IPCE spectra, we can therefore see that the Type II structure allows for $BiVO_4$ to act as a sensitizer for TiO_2 to allow visible light utilization, and that the nanowire array provides a higher path length for light absorption, resulting in much higher light harvesting efficiency than planar $BiVO_4$ (Figure 16c). Improvements to the host material could result in higher collection efficiency from the $BiVO_4$ guest. Additionally, as these $BiVO_4$ particles are undoped, further improvements in performance could be made by taking advantage of the extensive previous studies on improvements in $BiVO_4$ performance by W or Mo doping.[51-53]

3.4.5 Band alignment of TiO_2 and $BiVO_4$

The host-guest photoanode design relies on a Type II band alignment existing between $BiVO_4$ and TiO_2, such that electron transfer from the $BiVO_4$ to the TiO_2 is favorable. To determine the relative band positions of TiO_2 and $BiVO_4$ and experimentally demonstrate this Type II band alignment, electrochemical and spectroscopic measurements were performed.

The flat band potential (V_{fb}) can give an estimate of the band positions of a semiconductor in an aqueous environment. The primary method for determining V_{fb} is based on electrochemical impedance spectroscopy and appears as the x-intercept of the linear portion of a Mott-Schottky plot.[45] In addition, the V_{fb} of a semiconductor will change as a function of pH due to surface charging by adsorption of H^+ and OH^- ions. The V_{fb} was measured as a function of pH and shown to change by approximately 59 mV/pH (Figure 20). Therefore, as shown in Figure 27a, the V_{fb}s of TiO_2 and $BiVO_4$ are determined to be 0.19 V and 0.08 V vs. RHE, respectively. These results are in agreement with previous measurements of the V_{fb} of the two semiconductors.[17, 54] Assuming the gap between the V_{fb} and the bottom edge of the conduction band is small (~0.2 eV) and similar for TiO_2 and $BiVO_4$, this result is consistent with a Type II band alignment between the two semiconductors.[55]

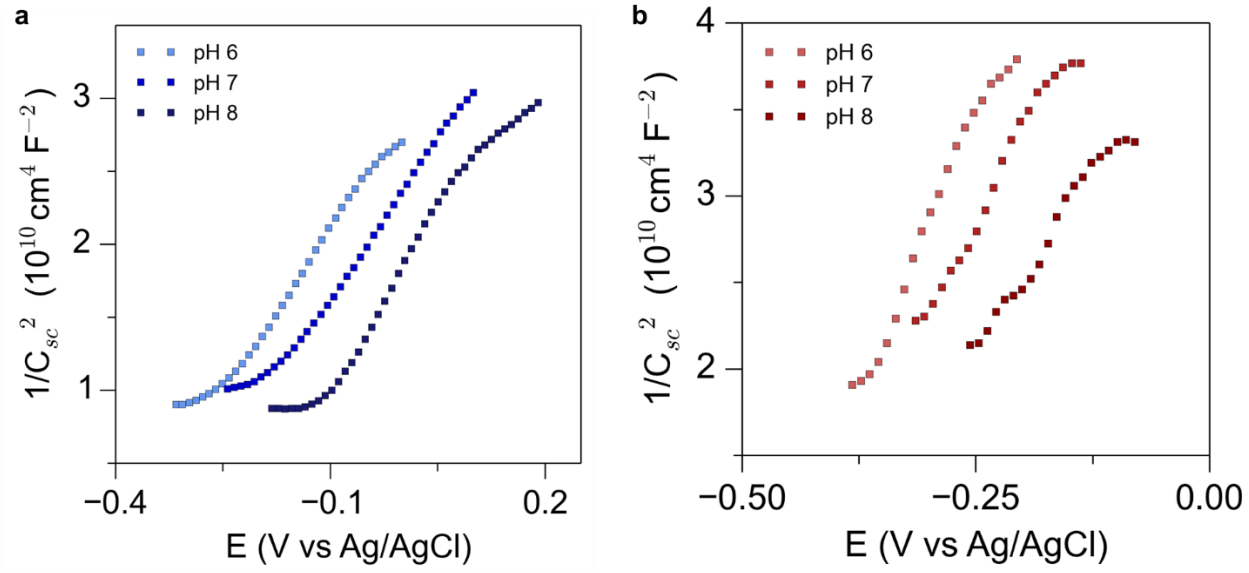

Figure 3.20: Mott-Schottky plots at varying pH for TiO_2 and $BiVO_4$ (a,b) Mott-Schottky plots for TiO_2 and $BiVO_4$. E_{fb} is observed to shift ~59 mV/pH.

For further confirmation of the band positions, ultraviolet photoelectron spectroscopy (UPS) was used in addition to Mott-Schottky measurements. UPS provides high energy resolution (<0.1 eV) due to the small linewidth of the He discharge source and is therefore a powerful tool for investigating the band positions of semiconductors. UPS allows one to obtain both the work function of the material, which is the energetic difference between the photon energy of He I (21.22 eV) and the low kinetic energy cutoff of the spectrum, and the valence band maximum with respect to the Fermi level (E_F).[56] The position of E_F is referenced to a metal standard. The relationship between these energy levels is depicted with the UPS spectrum of TiO_2 and $BiVO_4$ in Figure 27b. Here, we are interested in the position of the band edges of the two semiconductors with respect to the E_{vac}. Thus we plot the spectra for TiO_2 and $BiVO_4$ with E_{vac} at the same position. The positions of the band edges are found using the Fermi level of a reference standard and linear extrapolation of the valence band and secondary electron cutoff regions. The work functions for TiO_2 and $BiVO_4$ were found to be 4.64 and 4.56 eV respectively, and the valence band positions were found to be 7.61 and 6.99 eV vs the E_{vac}, or 3.17 and 2.55 V on the RHE scale.

To give a complete picture of the band alignment of the two semiconductors, the conduction band position was calculated by addition of the band gap to the valence band position. The optical band gap of the two semiconductors was determined by constructing Tauc plots from optical absorption data. (Figures 17, 21, 22). Extrapolation of the Tauc plot onto the x- intercept gives an optical band gap of ~3.0 eV and ~2.5 eV for TiO_2 and $BiVO_4$, respectively (Figures 21, 22).[57] Optical absorption for TiO_2 and Ta:TiO_2 nanowires was identical (Figure 23). Additionally, the band gap was confirmed by measuring the difference between the O-K edge X-ray emission and X-ray absorption edge positions. This analysis yielded values of 2.5 and 3.0 eV, consistent with the optical measurements (Figures 24, 25). Addition of the optical band gap to the valence band position gives the conduction band position and completes the full band diagram (Figure 27c). This analysis yielded conduction band values of 0.17 V vs RHE for TiO_2 and 0.04 V vs RHE for $BiVO_4$. These spectroscopic measurements are consistent with the Type II band alignment between TiO_2 and $BiVO_4$, and the electrochemical flat band potential measurements.

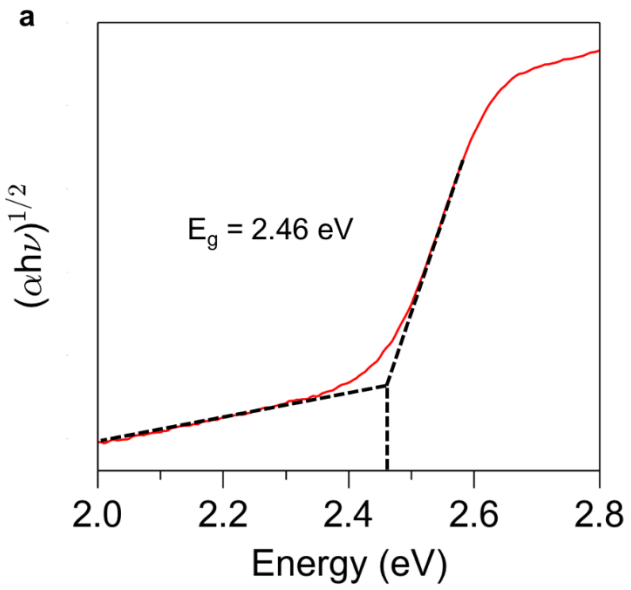

Figure 3.21: Tauc plot for $BiVO_4$ for an indirect transition (a) Tauc plot of a $BiVO_4$ thin film deposited on FTO/glass assuming the optical band gap of $BiVO_4$ is an indirect transition. A smaller band gap is observed consistent with the work of Cooper et al.[58]

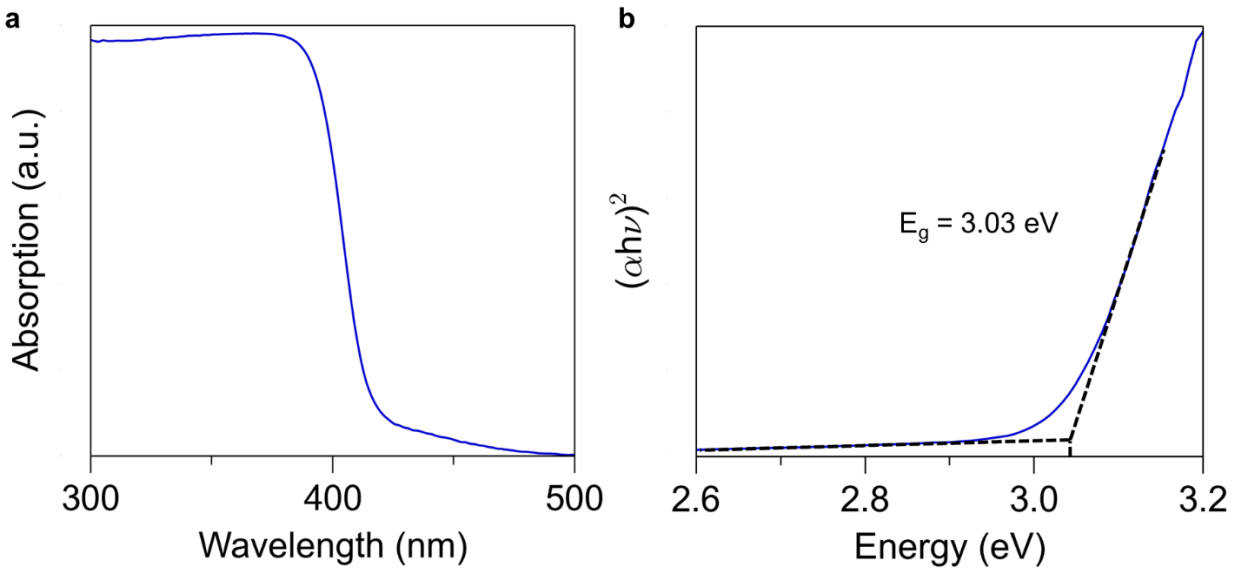

Figure 3.22: Optical characterization of TiO_2 nanowires (a) Optical absorption and (b) Tauc plot of TiO_2 nanowire samples on FTO/glass assuming the optical band gap of TiO_2 is a direct transition.

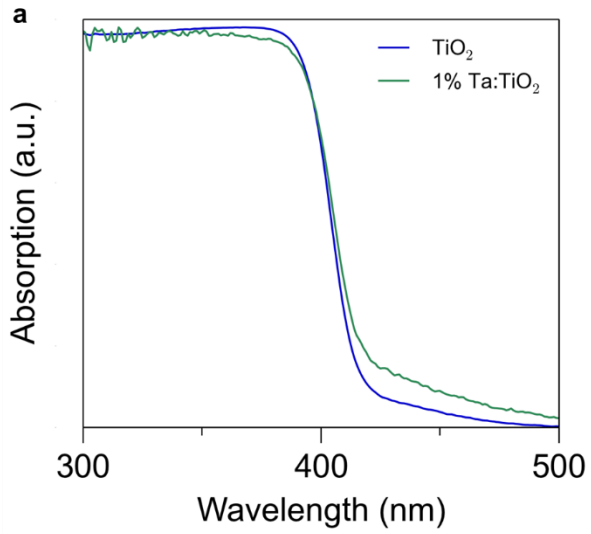

Figure 3.23: UV Vis absorption for TiO_2 and Ta:TiO_2 nanowires (a) Optical absorption of TiO_2 and Ta:TiO_2 nanowire samples demonstrating the optical absorption is not significantly changed by the doping process.

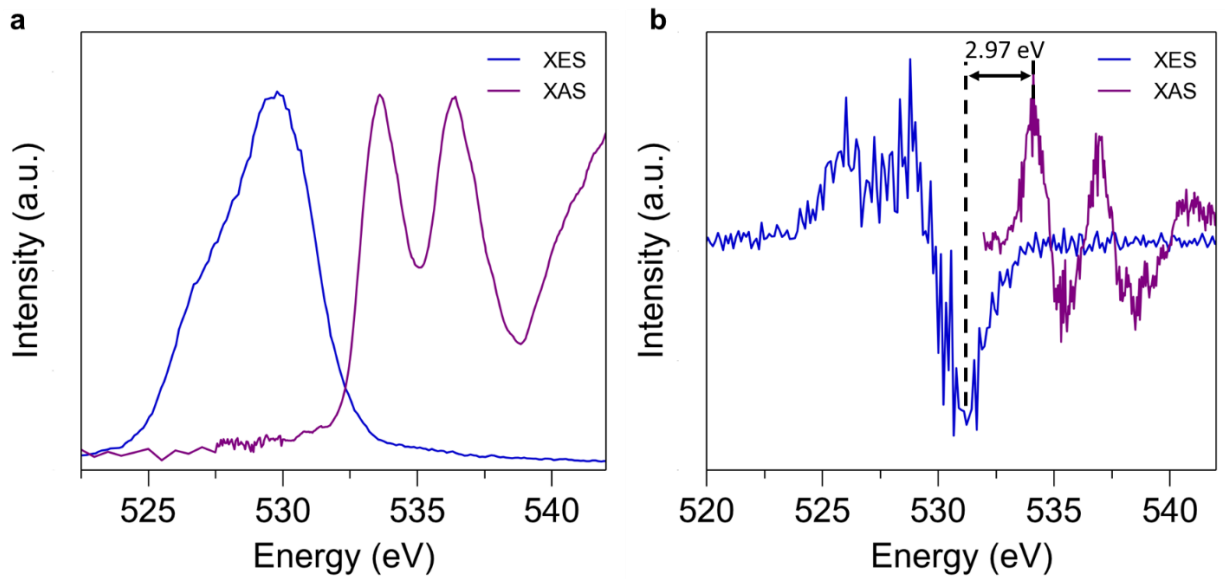

Figure 3.24: Electronic band gap calculation using X-ray absorption and emission for TiO_2 (a) Combined X ray absorption and emission spectra for TiO_2. (b) Derivative spectrum of (a). The difference between the local maximum of the XAS spectrum and local minimum of the XES spectrum gives the electronic band gap.

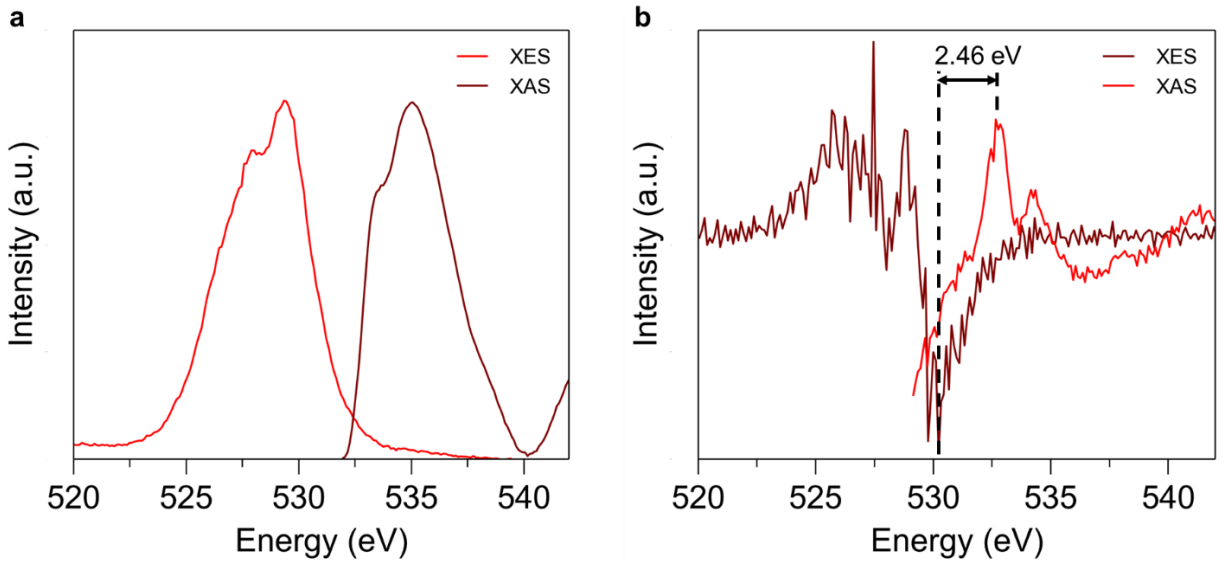

Figure 3.25: Electronic band gap calculation using X-ray absorption and emission for TiO_2 (a) Combined X ray absorption and emission spectra for $BiVO_4$. (b) Derivative spectrum of (a). The difference between the local maximum of the XAS spectrum and local minimum of the XES spectrum gives the electronic band gap.

In addition to the UPS measurements, the work function was also confirmed by ambient pressure photoelectron spectroscopy. Briefly, the binding energy of Ar 2p in the vicinity of the sample surface can be used to measure the local work function. This is an emergent technique for measuring work functions and has been demonstrated to measure work function differences in ligand capped PbS quantum dots.[59] This analysis found the work function of TiO_2 to be ~0.2 eV higher than that of $BiVO_4$, consistent with the previous spectroscopic and electrochemical measurements (Figure 26).

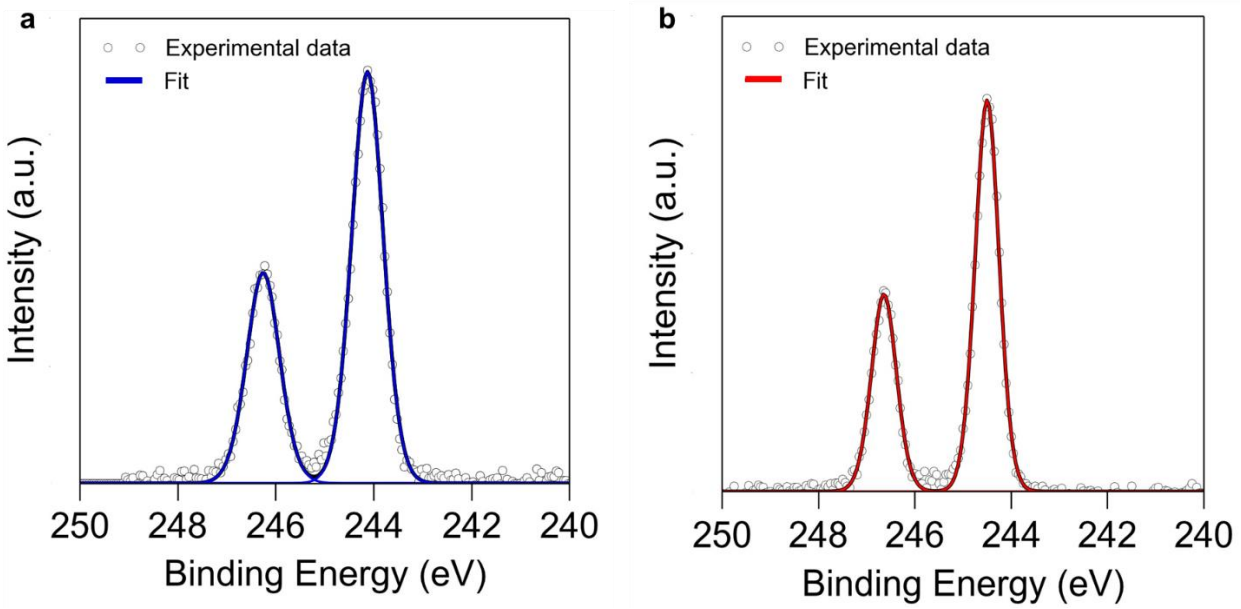

Figure 3.26: Work function measurements for TiO_2 and $BiVO_4$ using Ar APXPS (a,b) Ar 2p XPS spectra taken in the near surface region of TiO_2 and $BiVO_4$. The work function is related to the Ar $2p_{3/2}$ binding energy values. The work function of TiO_2 is estimated to be ~0.2 eV larger than that of $BiVO_4$.

Using these results, we can show the band alignment relative to vacuum of the two semiconductors before contact. Consistent with our photoelectrochemical data, the results of both our spectroscopic and electrochemical measurements demonstrate that TiO_2 and $BiVO_4$ form a Type II band alignment and that electron transfer from $BiVO_4$ to TiO_2 is indeed favorable. After equilibration, band bending at the interface of the two semiconductors will determine the ease with which charge carriers can cross the interface, and unfavorable band bending can create barriers which reduce electron transfer, even if it is energetically favorable overall. We observed this through the reduced photocurrents of TiO_2|$BiVO_4$ samples with low Ta concentrations, indicating significant loss of charge carriers at the TiO_2|$BiVO_4$ interface. Further investigations into the efficiency of electron transfer between the two materials could yield insights to improve the photoelectrochemical performance.

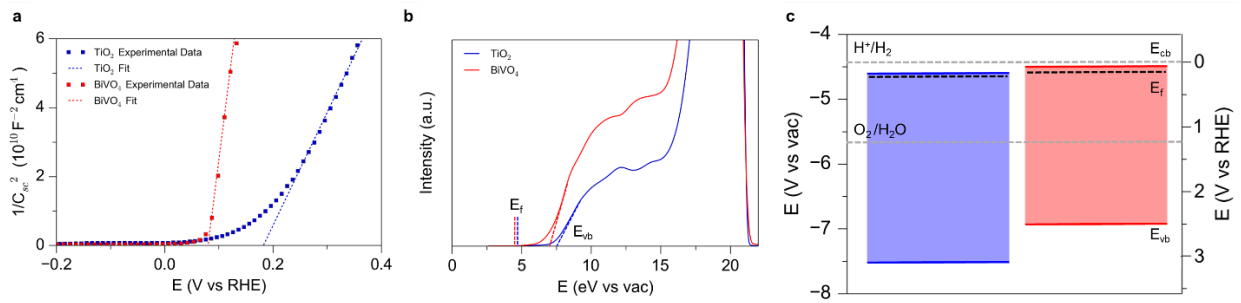

Figure 3.27: Band alignment between TiO_2 and $BiVO_4$ (a) Mott-Schottky plots showing the flat band potential of $BiVO_4$ is more negative than that of TiO_2. (b) UPS spectra of TiO_2 and $BiVO_4$ with a fixed vacuum level. The valence band maximum and Fermi level of the two semiconductors are indicated. (c) Band diagram from electrochemical and spectroscopic data, confirming the Type-II alignment between $BiVO_4$ and TiO_2.

3.4.6 Electron transfer between TiO_2 and $BiVO_4$

X-ray absorption and emission spectroscopy was used to gain insight into the orbital character of the energy levels involved in the electron transfer process. Previous studies indicate the TiO_2 conduction band is composed primarily of Ti 3d orbital contributions while the valence band has primarily O 2p character.[60] For $BiVO_4$, the most important contributions to the conduction band come from V 3d orbitals and O 2p orbitals for the valence band.[57] To further investigate the band edge electronic structure of the two semiconductors, valence band photoemission spectroscopy and resonant inelastic x-ray scattering (RIXS) was used. Our results were in agreement with previous studies indicating the electron transfer occurs via a d-d transition between V 3d states in the conduction band of $BiVO_4$ and Ti 3d states in TiO_2 (Figures 28-34). Further studies to investigate the kinetics of this electron transfer process and how they affect the system performance would be of interest.

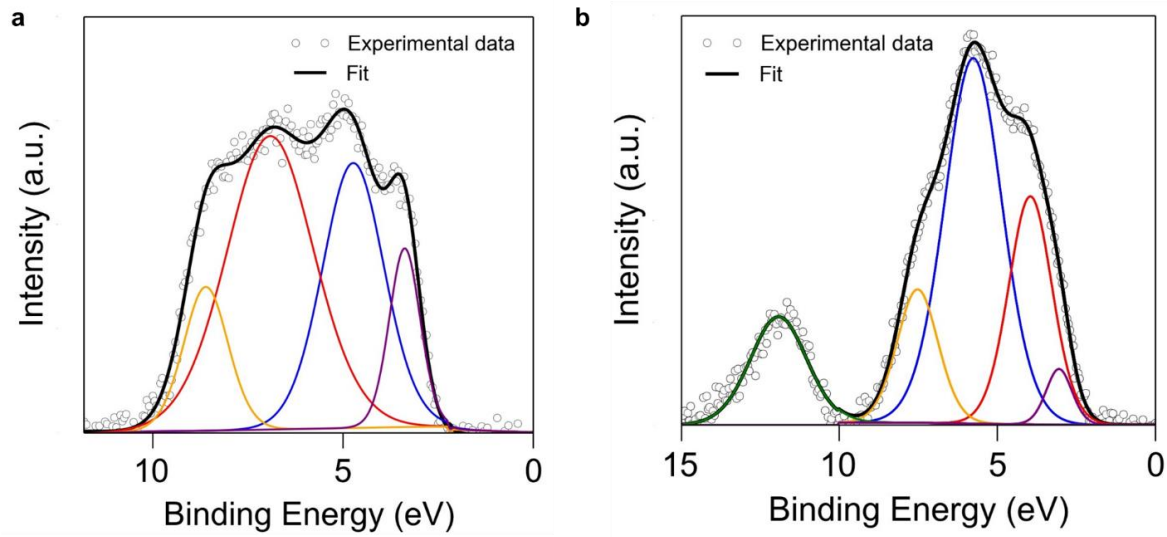

Figure 3.28: Valence band electronic structure of $BiVO_4$ and TiO_2 (a,b) Valence band electronic structure of TiO_2 and $BiVO_4$ measured using XPS.

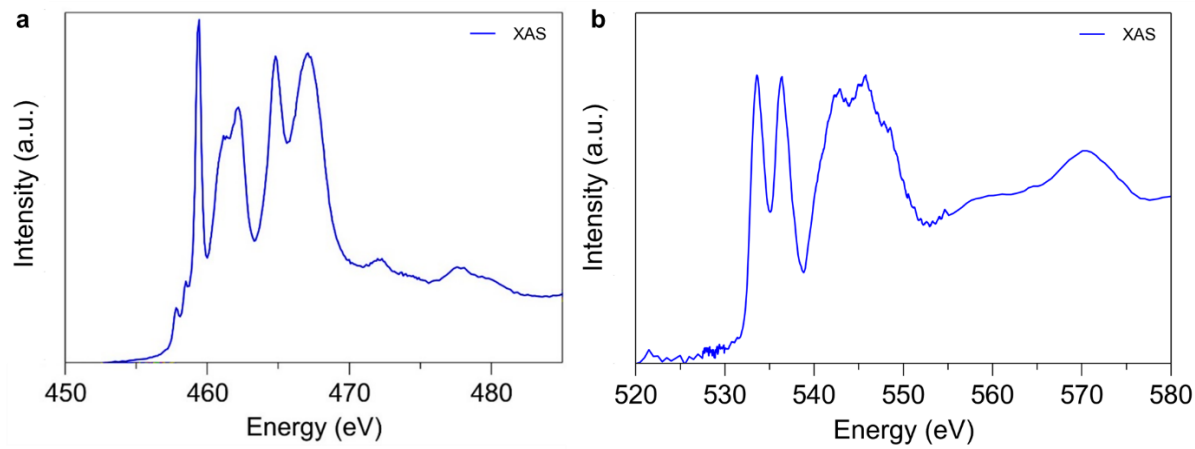

Figure 3.29: Ti L edge and O K edge X-ray absorption spectra of TiO_2 (a,b) Ti L edge and O K edge X-ray absorption spectra for TiO_2. Total electron yield (TEY) data is shown, as no significant differences were observed between TEY and fluorescence yield data.

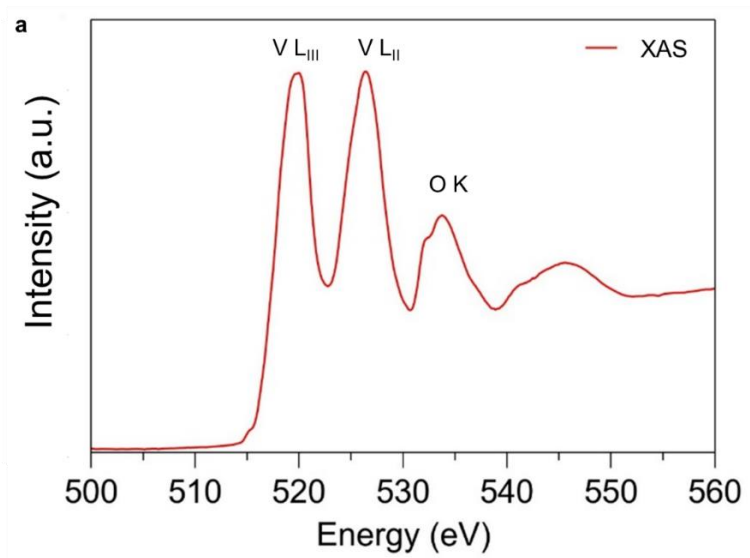

Figure 3.30: V L edge and O K edge X-ray absorption spectra of $BiVO_4$ (a) V L edge and O K edge X-ray absorption spectra for $BiVO_4$. Total electron yield (TEY) data is shown, as no significant differences were observed between TEY and fluorescence yield data.

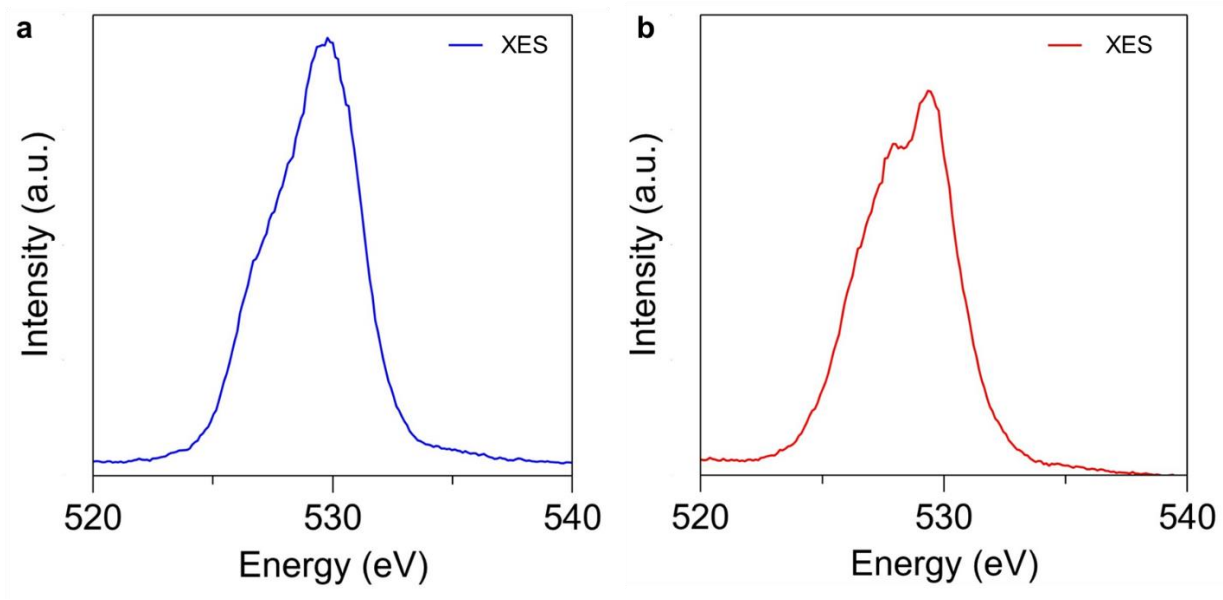

Figure 3.31: X-ray emission spectra of $BiVO_4$ and TiO_2 (a,b) X ray emission spectra of TiO_2 and $BiVO_4$ measured at an excitation energy of 590 eV.

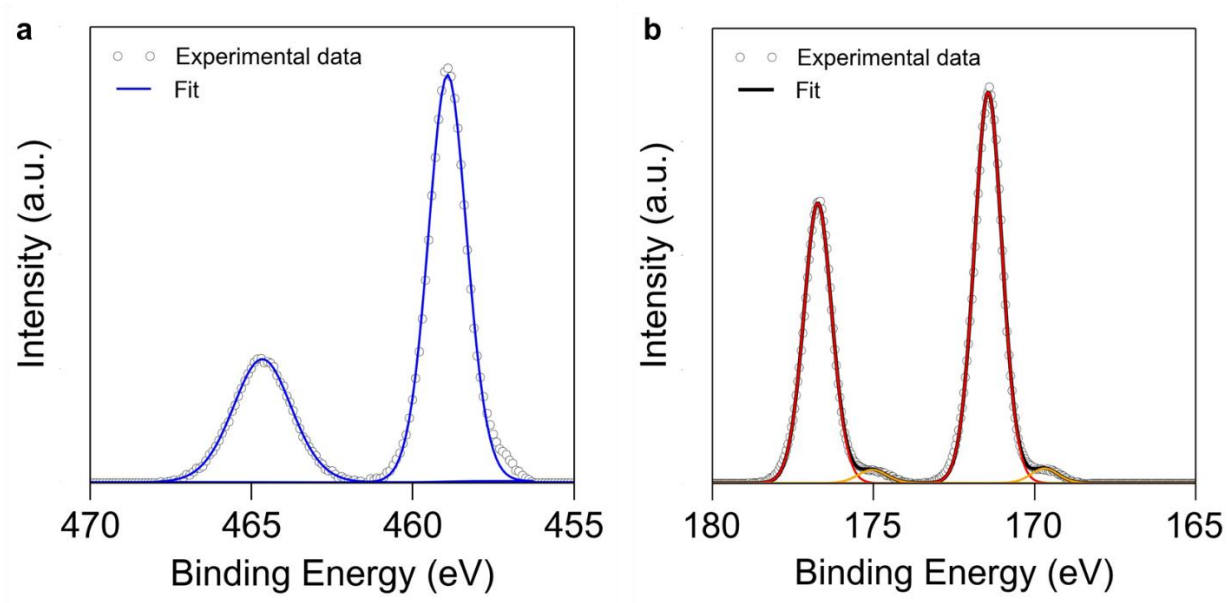

Figure 3.32: Core-level XPS of $BiVO_4$ and TiO_2 (a,b) XPS spectra of the Ti 2p level for TiO_2 and Bi 4f level for $BiVO_4$.

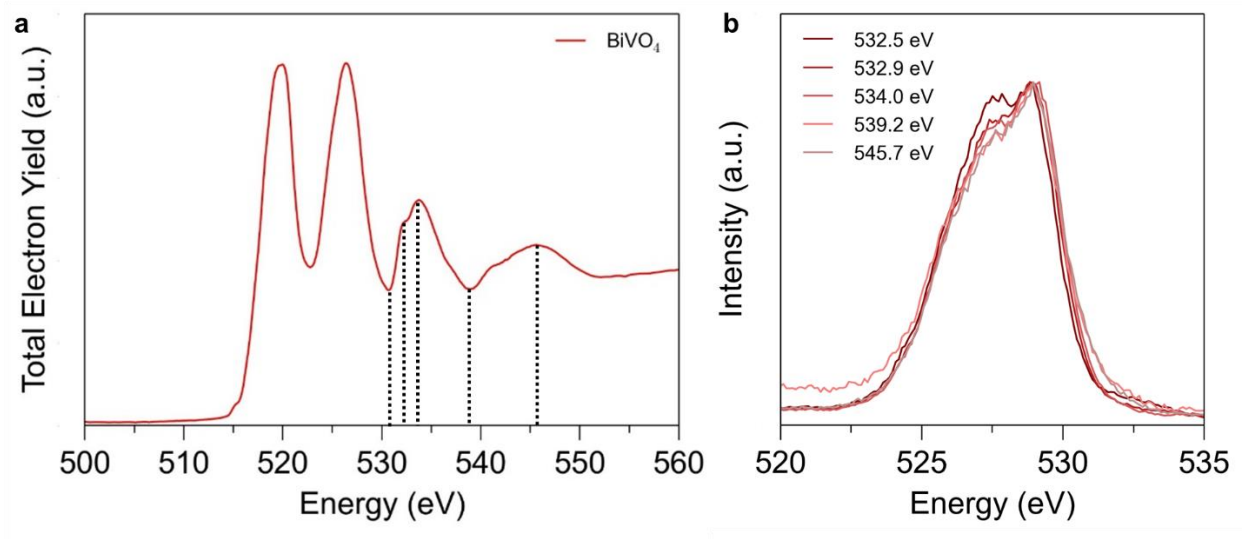

Figure 3.33: Resonant inelastic X-ray scattering of $BiVO_4$ (b) RIXS spectra for $BiVO_4$ on the O K edge. Excitation energies are specified on the XAS spectrum in (a).

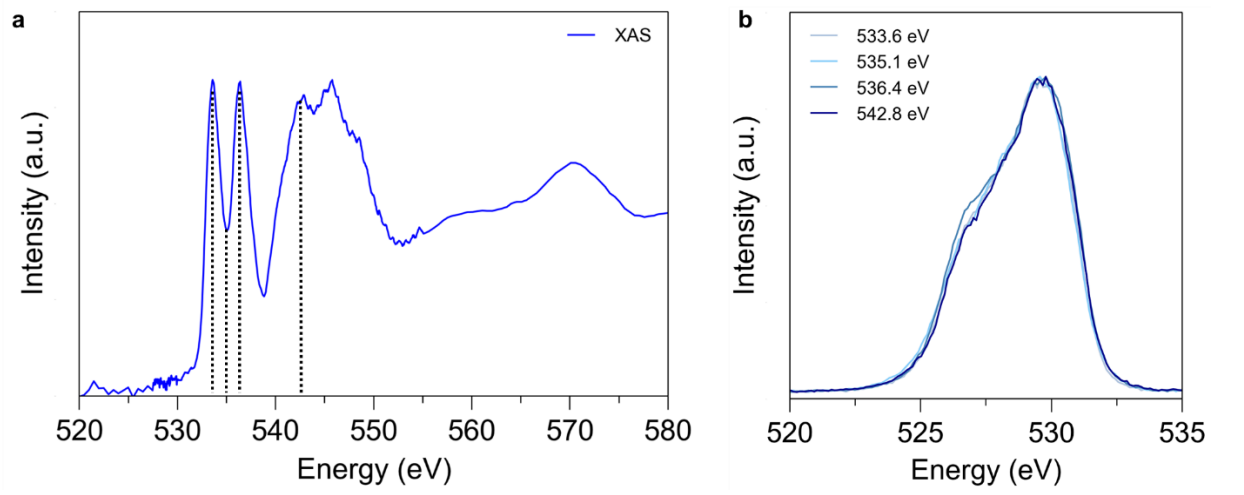

Figure 3.34: Resonant inelastic X-ray scattering of TiO_2 (b) RIXS spectra for TiO_2 on the O K edge. Excitation energies are specified on the XAS spectrum in (a).

3.5 Conclusions

Host-guest systems are useful for achieving high performance in dual absorber photoelectrosynthetic cells when using photoanode materials with poor intrinsic carrier transport properties such as Fe_2O_3 and $BiVO_4$. In this study we have demonstrated the use of TiO_2 as a host material for $BiVO_4$, to provide simultaneous high light absorption and carrier collection efficiency. We have shown how modifications of the host and guest materials can lead to higher performance, namely by doping the TiO_2 guest material, and improving the charge transfer efficiencies of the $BiVO_4$ by addition of a Co-based catalyst. Electrochemical and spectroscopic measurements give evidence for the Type II band alignment necessary for favorable electron transfer from $BiVO_4$ to

TiO_2. We believe this architecture can be extended to improve the performance of related photoanode materials. Achieving higher photocurrents at low potentials will allow for efficient coupling with well-developed photocathode materials for higher bias-free solar to hydrogen efficiencies.

3.6 References

1. Walter, M. G.; Warren, E. L.; McKone, J. R.; Boettcher, S. W.; Mi, Q.; Santori, E. A.; Lewis, N. S. *Chem. Rev.* **2010,** 110, (11), 6446-6473.
2. Bolton, J. R.; Strickler, S. J.; Connolly, J. S. *Nature* **1985,** 316, (6028), 495-500.
3. Nozik, A. J. *Appl. Phy. Lett.* **1977,** 30, (11), 567.
4. Seitz, L. C.; Chen, Z.; Forman, A. J.; Pinaud, B. A.; Benck, J. D.; Jaramillo, T. F. *ChemSusChem* **2014,** 7, (5), 1372-85.
5. Hu, S.; Xiang, C.; Haussener, S.; Berger, A. D.; Lewis, N. S. *Energy Environ. Sci.* **2013,** 6, (10), 2984.
6. Liu, C.; Dasgupta, N. P.; Yang, P. *Chem. Mater.* **2014,** 26, (1), 415-422.
7. Ni, M.; Leung, M. K. H.; Leung, D. Y. C.; Sumathy, K. *Renew. Sust. Energy Rev.* **2007,** 11, (3), 401-425.
8. Chen, Z.; Jaramillo, T. F.; Deutsch, T. G.; Kleiman-Shwarsctein, A.; Forman, A. J.; Gaillard, N.; Garland, R.; Takanabe, K.; Heske, C.; Sunkara, M.; McFarland, E. W.; Domen, K.; Miller, E. L.; Turner, J. A.; Dinh, H. N. *J. Mater. Res.* **2011,** 25, (01), 3-16.
9. Chen, Y. W.; Prange, J. D.; Duhnen, S.; Park, Y.; Gunji, M.; Chidsey, C. E.; McIntyre, P. C. *Nat. Mater.* **2011,** 10, (7), 539-44.
10. Hu, S.; Shaner, M. R.; Beardslee, J. A.; Lichterman, M.; Brunschwig, B. S.; Lewis, N. S. *Science* **2014,** 344, (6187), 1005-1009.
11. Sun, K.; Kuang, Y.; Verlage, E.; Brunschwig, B. S.; Tu, C. W.; Lewis, N. S. *Adv. Energy Mater.* **2015**, 5, 1402276.
12. Boettcher, S. W.; Warren, E. L.; Putnam, M. C.; Santori, E. A.; Turner-Evans, D.; Kelzenberg, M. D.; Walter, M. G.; McKone, J. R.; Brunschwig, B. S.; Atwater, H. A.; Lewis, N. S. *J. Am. Chem. Soc.* **2011,** 133, (5), 1216-9.
13. Lee, M. H.; Takei, K.; Zhang, J.; Kapadia, R.; Zheng, M.; Chen, Y. Z.; Nah, J.; Matthews, T. S.; Chueh, Y. L.; Ager, J. W.; Javey, A. *Angew. Chem. Int. Ed.* **2012,** 51, (43), 10760-4.
14. Liu, X.; Wang, F.; Wang, Q. *Phys. Chem. Chem. Phys.* **2012,** 14, (22), 7894-911.
15. Sivula, K.; Le Formal, F.; Gratzel, M. *ChemSusChem* **2011,** 4, (4), 432-49.
16. Park, Y.; McDonald, K. J.; Choi, K. S. *Chem. Soc. Rev.* **2013,** 42, (6), 2321-37.
17. Rettie, A. J. E.; Lee, H. C.; Marshall, L. G.; Lin, J.-F.; Capan, C.; Lindemuth, J.; McCloy, J. S.; Zhou, J.; Bard, A. J.; Mullins, C. B. *J. Am. Chem. Soc.* **2013,** 135, (30), 11389-11396.
18. Kim, T. W.; Choi, K.-S. *Science* **2014,** 343, (6174), 990-994.
19. Robel, I.; Subramanian, V.; Kuno, M.; Kamat, P. V. *J. Am. Chem. Soc.* **2006,** 128, (7), 2385-2393.
20. Grätzel, M. *J. Photochem. Photobio. C* **2003,** 4, (2), 145-153.
21. Liu, H.; Tang, J.; Kramer, I. J.; Debnath, R.; Koleilat, G. I.; Wang, X.; Fisher, A.; Li, R.; Brzozowski, L.; Levina, L.; Sargent, E. H. *Adv. Mater.* **2011,** 23, (33), 3832-3837.

22. Dasgupta, N. P.; Sun, J.; Liu, C.; Brittman, S.; Andrews, S. C.; Lim, J.; Gao, H.; Yan, R.; Yang, P. *Adv. Mater.* **2014,** 26, (14), 2137-2184.
23. Law, M.; Greene, L. E.; Johnson, J. C.; Saykally, R.; Yang, P. *Nat. Mater.* **2005,** 4, (6), 455-9.
24. Kim, H. S.; Lee, J. W.; Yantara, N.; Boix, P. P.; Kulkarni, S. A.; Mhaisalkar, S.; Gratzel, M.; Park, N. G. *Nano Lett.* **2013,** 13, (6), 2412-7.
25. Leschkies, K. S.; Divakar, R.; Basu, J.; Enache-Pommer, E.; Boercker, J. E.; Carter, C. B.; Kortshagen, U. R.; Norris, D. J.; Aydil, E. S. *Nano Lett.* **2007,** 7, (6), 1793-1798.
26. Lin, Y.; Zhou, S.; Sheehan, S. W.; Wang, D. *J. Am. Chem. Soc.* **2011,** 133, (8), 2398-2401.
27. Sivula, K.; Formal, F. L.; Grätzel, M. *Chem. Mater.* **2009,** 21, (13), 2862-2867.
28. Stefik, M.; Cornuz, M.; Mathews, N.; Hisatomi, T.; Mhaisalkar, S.; Grätzel, M. *Nano Lett.* **2012,** 12, (10), 5431-5435.
29. Liu, Q.; He, J.; Yao, T.; Sun, Z.; Cheng, W.; He, S.; Xie, Y.; Peng, Y.; Cheng, H.; Sun, Y.; Jiang, Y.; Hu, F.; Xie, Z.; Yan, W.; Pan, Z.; Wu, Z.; Wei, S. *Nat. Commun.* **2014,** 5.
30. Pilli, S. K.; Janarthanan, R.; Deutsch, T. G.; Furtak, T. E.; Brown, L. D.; Turner, J. A.; Herring, A. M. *Phys. Chem. Chem. Phys.* **2013,** 15, (35), 14723-14728.
31. Rao, P. M.; Cai, L.; Liu, C.; Cho, I. S.; Lee, C. H.; Weisse, J. M.; Yang, P.; Zheng, X. *Nano Lett.* **2014,** 14, (2), 1099-1105.
32. Shi, X.; Choi, I. Y.; Zhang, K.; Kwon, J.; Kim, D. Y.; Lee, J. K.; Oh, S. H.; Kim, J. K.; Park, J. H. *Nat. Commun.* **2014,** 5, 4775.
33. Moniz, S. J. A.; Zhu, J.; Tang, J. *Adv. Energy Mater.* **2014,** 4, (10), n/a-n/a.
34. Ho-Kimura, S.; Moniz, S. J. A.; Handoko, A. D.; Tang, J. *J. Mater. Chem. A* **2014,** 2, (11), 3948-3953.
35. Furubayashi, Y.; Hitosugi, T.; Yamamoto, Y.; Inaba, K.; Kinoda, G.; Hirose, Y.; Shimada, T.; Hasegawa, T. *Appl. Phys. Lett.* **2005,** 86, (25), 252101.
36. Taro, H.; Yutaka, F.; Atsuki, U.; Kinnosuke, I.; Kazuhisa, I.; Yasushi, H.; Go, K.; Yukio, Y.; Toshihiro, S.; Tetsuya, H. *Jpn. J. Appl. Phys.* **2005,** 44, (8L), L1063.
37. Shockley, W. *Bell Syst. Tech. J.* **1949,** 28, (3), 435-489.
38. Resasco, J.; Dasgupta, N. P.; Rosell, J. R.; Guo, J.; Yang, P. *J. Am. Chem. Soc.* **2014,** 136, (29), 10521-10526.
39. Liu, B.; Aydil, E. S. *J. Am. Chem. Soc.* **2009,** 131, (11), 3985-3990.
40. Hausmann, D. M.; de Rouffignac, P.; Smith, A.; Gordon, R.; Monsma, D. *Thin Solid Films* **2003,** 443, (1–2), 1-4.
41. Kang, D.; Park, Y.; Hill, J. C.; Choi, K.-S. *J. Phys. Chem. Lett.* **2014,** 5, (17), 2994-2999.
42. Grass, M. E.; Karlsson, P. G.; Aksoy, F.; Lundqvist, M.; Wannberg, B.; Mun, B. S.; Hussain, Z.; Liu, Z. *Rev. Sci. Instrum.* **2010,** 81, (5), 053106.
43. George, S. M. *Chem. Rev.* **2010,** 110, (1), 111-131.
44. Parker, R. A. *Phys. Rev.* **1961,** 124, (6), 1719-1722.
45. Gelderman, K.; Lee, L.; Donne, S. W. *J. Chem. Educ.* **2007,** 84, (4), 685.
46. Cho, I. S.; Lee, C. H.; Feng, Y.; Logar, M.; Rao, P. M.; Cai, L.; Kim, D. R.; Sinclair, R.; Zheng, X. *Nat. Commun.* **2013,** 4, 1723.
47. Xu, M.; Da, P.; Wu, H.; Zhao, D.; Zheng, G. *Nano Lett.* **2012,** 12, (3), 1503-1508.
48. McDonald, K. J.; Choi, K.-S. *Chem. Mater.* **2011,** 23, (7), 1686-1693.
49. Zhong, D. K.; Choi, S.; Gamelin, D. R. *J. Am. Chem. Soc.* **2011,** 133, (45), 18370-18377.
50. Kanan, M. W.; Nocera, D. G. *Science* **2008,** 321, (5892), 1072-1075.

51. Abdi, F. F.; Firet, N.; van de Krol, R. *ChemCatChem* **2013,** 5, (2), 490-496.
52. Park, H. S.; Kweon, K. E.; Ye, H.; Paek, E.; Hwang, G. S.; Bard, A. J. *J. Phys. Chem. C* **2011,** 115, (36), 17870-17879.
53. Abdi, F. F.; Han, L.; Smets, A. H.; Zeman, M.; Dam, B.; van de Krol, R. *Nat. Commun.* **2013,** 4, 2195.
54. Cooper, G.; Turner, J. A.; Nozik, A. J. *J. Electrochem. Soc.* **1982,** 129, (9), 1973-1977.
55. Xu, Y.; Schoonen, M. A. A. *Am. Mineral.* **2000,** 85, (3-4), 543-556.
56. Goscinski, O. *Int. J. Quantum Chem.* **1978,** 13, (2), 263-263.
57. Cooper, J. K.; Gul, S.; Toma, F. M.; Chen, L.; Glans, P.-A.; Guo, J.; Ager, J. W.; Yano, J.; Sharp, I. D. *Chem. Mater.* **2014,** 26, (18), 5365-5373.
58. Cooper, J. K.; Gul, S.; Toma, F. M.; Chen, L.; Liu, Y.-S.; Guo, J.; Ager, J. W.; Yano, J.; Sharp, I. D. *J. Phys. Chem. C* **2015,** 119, (6), 2969-2974.
59. Axnanda, S.; Scheele, M.; Crumlin, E.; Mao, B.; Chang, R.; Rani, S.; Faiz, M.; Wang, S.; Alivisatos, A. P.; Liu, Z. *Nano Lett.* **2013,** 13, (12), 6176-6182.
60. Landmann, M.; Rauls, E.; Schmidt, W. *J. Phys. Condens. Matter* **2012,** 24, (19), 195503.

Chapter 4

Standard methods for measuring and reporting catalytic data for electrochemical CO_2 reduction

4.1 Introduction

The electrochemical reduction of carbon dioxide (CO_2) offers an attractive means of utilizing CO_2 as a source of carbon for the production of transportation fuels and commodity chemicals using intermittent renewable electricity, such as that produced by wind or solar energy.[1-3] Extensive efforts have been devoted to identifying electrocatalysts that can selectively and efficiently reduce CO_2 to desired products.[4-7] However, objective evaluation of the activity and selectivity of both standard and novel electrocatalysts is currently hindered by the lack of standardized methods for preparing catalysts and electrolytes and for measuring and reporting electrocatalytic activity. These issues are significant because the performance of electrocatalyts is influenced not only by the composition and morphology of the electrocatalyst itself, but also by the mass transfer of reactants to and products from the cathode of the electrochemical cell, and by the purity of the electrocatalyst and electrolyte.

In this chapter we briefly summarize the variables that influence the measured activity and selectivity of electrocatalysts used for CO_2 reduction with the aim of establishing what should be done to obtain reproducible data that can be attributed to properties of the catalyst itself, and compared with data obtained by other groups. We then mention how we address these issues to ensure that we can obtain meaningful electrocatalytic data.

4.2 Considerations when measuring electrocatalytic activity

4.2.1 Impact of impurities on electrocatalytic activity

To determine the intrinsic properties of a catalyst, its steady-state activity and selectivity must be determined in the absence of significant surface contamination. If surface contamination occurs, it is important to distinguish whether it is the result of catalytic intermediates that poison the surface or whether it is the result of avoidable impurities introduced onto the catalyst surface.[8] The high overpotentials typically utilized to evaluate the activity of CO_2 reduction electrocatalysts are sufficient to reduce nearly any transition metal cations that might be present in the catholyte.[9, 10] In general, transition metal impurities deposited onto the electrocatalyst surface will increase the activity of the electrocatalyst for the H_2 evolution reaction (HER), since the late transition and p-block metals typically utilized as CO_2 reduction electrocatalysts have very low activity for driving HER.[11, 12] Even trace quantities (< 10 μM) of transition metal cations can cause CO_2 reduction electrocatalysts to lose their activity on the timescale of a typical experiment.[11, 12] For this reason, in the experiments throughout the remained of this thesis, all experiments used the purest available water, electrolyte salts, and electrode materials to avoid contaminating the surface of the electrocatalyst. Additionally, unless otherwise noted, metallic anodes were avoided in favor of carbon-based materials. Carbon counter electrodes and all cell components were also cleaned in ultrapure nitric acid before use to remove trace metal impurities.[13, 14]

4.2.2 Impact of mass transport limitations on electrocatalytic activity

The electrochemical reduction of CO_2 is highly susceptible to concentration polarization, wherein Faradaic processes induce concentration gradients at the electrode surface. These concentrations gradients arise due to the weakly buffered near-neutral bicarbonate solutions typically employed as electrolytes as well as the sluggish diffusion coefficient of CO_2 through aqueous solutions.[15, 16] Even modest current densities cause the pH and CO_2 concentration near the cathode surface to vary significantly from the bulk.[17, 18] The magnitude of the concentration gradients depend largely on the hydrodynamics of the electrochemical cell, which should be mixed vigorously to ensure good mass transport to the cathode. Electrolyte mixing in our small electrochemical cell is accomplished by agitation of the electrolyte with a column of CO_2 bubbles.[19-21] Activity data measured in a regime of significant concentration polarization is not intrinsic to the behavior of the catalyst alone and may only provide transferrable knowledge to other researchers if identical hydrodynamic conditions are replicated. Therefore, in our data we demonstrate whether polarization effects are significant, and use continuum modeling to estimate the magnitude of their effects.

4.2.3 Reporting electrocatalytic activity

There are several different ways to report measured electrocatalytic activity. One such commonly used metric is faradaic efficiency, which is defined as the charge passed to produce a specific product divided by the total faradaic charge passed. While this is a useful tool to describe the product distribution produced by a catalyst, it is problematic when comparing different catalysts with drastically different activities. For example, it is tempting to conclude that the catalyst that is more selective for producing a specific product is more active for producing that product. However, an increase in selectivity to a product may or may not be accompanied by an increase in the rate at which that product is produced. In these cases, faradaic efficiencies can obscure the true cause for differences between two catalysts. The rate of production of a product,

which is proportional to its partial current density, is a much less ambiguous descriptor of catalytic activity. For this reason, in the remaining chapter, we will use partial currents when analyzing catalytic data rather than Faradaic efficiencies.

4.2.4 Summary of experimental methods for measuring electrocatalytic activity

The electrochemical experiments in the following chapters were conducted in a gas-tight electrochemical cell machined from polyether ether ketone (PEEK). PEEK provides good chemical and mechanical stability to prevent introduction of unwanted impurities. A schematic of the cell is shown in Fig 4.2. Further experimental details of this cell are described in previous works.[21] The cell is composed of a cathode and anode chamber separated by an anion exchange membrane. The surface area of the electrocatalyst in this cell relative to the electrolyte volume is large to allow sensitive product quantification. Electrolytes are continuously purged with CO_2 in this cell through a gas dispersion frit. The exit gas stream from the cathode chamber feeds directly to a gas chromatograph for quantification of gaseous products, while liquid products are analyzed after electrolysis using high performance liquid chromatography. Further experimental details related to each specific process are included in subsequent chapters.

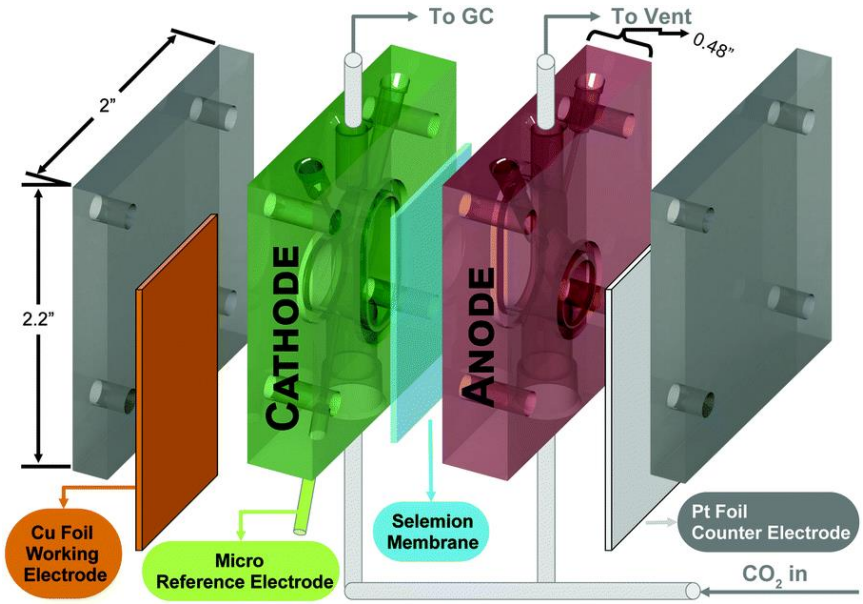

Figure 4.1: Schematic of electrochemical cell used for testing.

4.2.5 Reproducibility in electrocatalytic activity measurements

Consistent and repeatable reports of CO_2 reduction electrocatalysis are critical to advancing the field. By first benchmarking electrochemical systems against standard catalysts, researchers can be more confident that novel results will be repeatable at other sites, and that measured activity can be confidently attributed to the properties of the catalyst itself. The entire electrochemical

system, including catalyst, electrolyte, electrochemical cell, and operating conditions, needs to be considered to make appropriate comparisons with the literature. With careful experimentation, electrocatalyst activity can be accurate and consistently reproduced at different academic institutions. Figure 8 shows the activity toward selected products obtained for polycrystalline silver and epitaxial Cu(100) thin films, prepared and tested at Berkeley and Stanford. The samples were prepared independently and measured in two different electrochemical cells. Similar experimental protocols were used to avoid artifacts from impurities, and a potential range was chosen for comparison in which the effects of concentration polarization were minimized. The close agreement in activity demonstrates the consistency that can be obtained with careful measurements.

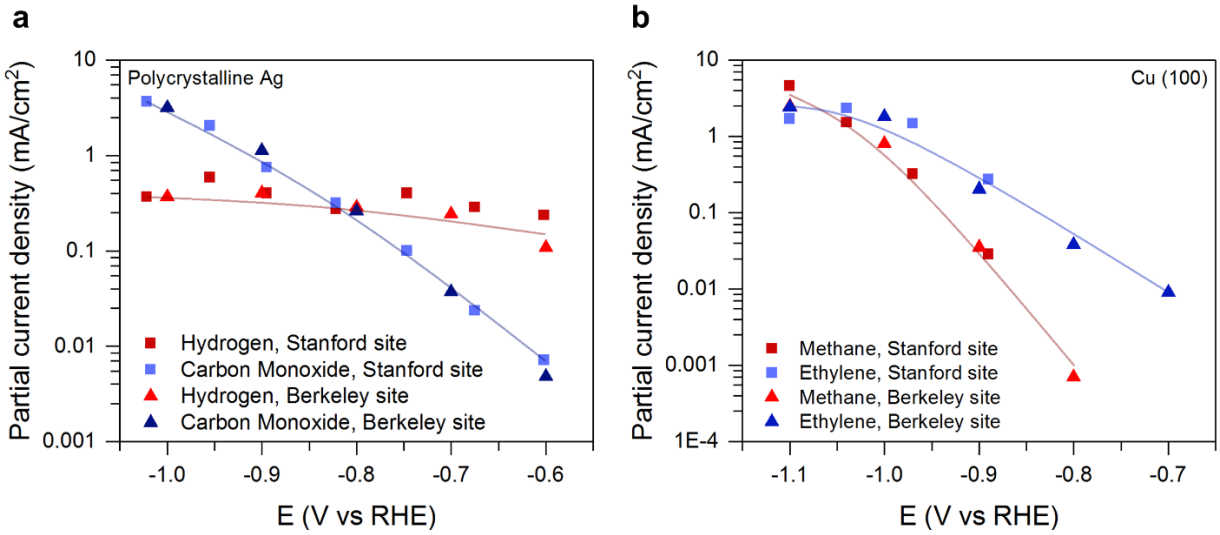

Figure 4.2: Reproducibility of benchmark catalytic activity. Polycrystalline Ag and Cu(100) catalysts prepared and tested independently at two different JCAP sites in 0.1 M $KHCO_3$. Lines are added to guide the eye.

4.3 References

1. Lewis, N. S.; Nocera, D. G. *Proc. Natl. Acad. Sci.* **2006,** 103, (43), 15729-15735.
2. Chu, S.; Majumdar, A. *Nature* **2012,** 488, (7411), 294-303.
3. Seh, Z. W.; Kibsgaard, J.; Dickens, C. F.; Chorkendorff, I.; Nørskov, J. K.; Jaramillo, T. F. *Science* **2017,** 355, (6321).
4. Li, C.; Kanan, M. *J. Am. Chem. Soc.* **2012,** 134, (17), 7231-7234.
5. Kim, D.; Resasco, J.; Yu, Y.; Asiri, A. M.; Yang, P. *Nat. Commun.* **2014,** 5, 4948.
6. Lu, Q.; Rosen, J.; Zhou, Y.; Hutchings, G. S.; Kimmel, Y. C.; Chen, J. G.; Jiao, F. *Nat. Commun.* **2014,** 5, 3242.
7. Mistry, H.; Varela, A. S.; Bonifacio, C. S.; Zegkinoglou, I.; Sinev, I.; Choi, Y.-W.; Kisslinger, K.; Stach, E. A.; Yang, J. C.; Strasser, P.; Cuenya, B. R. *Nat. Commun.* **2016,** 7, 12123.
8. Butt, J. B.; Petersen, E. E., In *Activation, Deactivation, and Poisoning of Catalysts*, Elsevier: 1988; pp 3-26.

9. Hori, Y., Electrochemical CO_2 Reduction on Metal Electrodes. In *Modern Aspects of Electrochemistry*, Vayenas, C. G.; White, R. E.; Gamboa-Aldeco, M. E., Eds. Springer New York: New York, NY, 2008; pp 89-189.
10. Kuhl, K. P.; Hatsukade, T.; Cave, E. R.; Abram, D. N.; Kibsgaard, J.; Jaramillo, T. F. *J. Am. Chem. Soc.* **2014,** 136, (40), 14107-14113.
11. Hori, Y.; Konishi, H.; Futamura, T.; Murata, A.; Koga, O.; Sakurai, H.; Oguma, K. *Electrochim. Acta* **2005,** 50, (27), 5354-5369.
12. Wuttig, A.; Surendranath, Y. *ACS Catal.* **2015,** 5, (7), 4479-4484.
13. Lum, Y.; Kwon, Y.; Lobaccaro, P.; Chen, L.; Clark, E. L.; Bell, A. T.; Ager, J. W. *ACS Catal.* **2016,** 6, (1), 202-209.
14. Wang, L.; Ambrosi, A.; Pumera, M. *Angew. Chem. Int. Ed.* **2013,** 52, (51), 13818-13821.
15. Butler, J. N., *Carbon dioxide equilibria and their applications*. CRC Press: 1991.
16. Haynes, W. M., *CRC handbook of chemistry and physics*. CRC press: 2014.
17. Singh, M. R.; Clark, E. L.; Bell, A. T. *Phys. Chem. Chem. Phys.* **2015,** 17, (29), 18924-18936.
18. Gupta, N.; Gattrell, M.; MacDougall, B. *J. Appl. Electrochem.* **2006,** 36, (2), 161-172.
19. Clark, E. L.; Singh, M. R.; Kwon, Y.; Bell, A. T. *Anal. Chem.* **2015,** 87, (15), 8013-8020.
20. Lobaccaro, P.; Singh, M. R.; Clark, E. L.; Kwon, Y.; Bell, A. T.; Ager, J. W. *Phys. Chem. Chem. Phys.* **2016,** 18, (38), 26777-26785.
21. Kuhl, K. P.; Cave, E. R.; Abram, D. N.; Jaramillo, T. F. *Energy Environ. Sci.* **2012,** 5, (5), 7050-7059.

Chapter 5

Promoter effects of alkali metal cations on the electrochemical reduction of carbon dioxide

This chapter contains material from the following publication:
Resasco, J.; Chen, L.D.; Clark, E.; Tsai, C.; Hahn, C.; Jaramillo, T.F.; Chan, K.; Bell, A.T *J. Am. Chem. Soc.* **2017,** 139, 11277-11287.

5.1 Abstract

The electrochemical reduction of CO_2 is known to be influenced by the identity of the alkali metal cation in the electrolyte; however, a satisfactory explanation for this phenomenon has not been developed. Here we present the results of experimental and theoretical studies aimed at elucidating the effects of electrolyte cation size on the intrinsic activity and selectivity of metal catalysts for the reduction of CO_2. Experiments were conducted under conditions where the influence of electrolyte polarization is minimal in order to show that cation size affects the intrinsic rates of formation of certain reaction products, most notably for $HCOO^-$, C_2H_4, and C_2H_5OH over Cu(100)- and Cu(111)-oriented thin films, and for CO and $HCOO^-$ over polycrystalline Ag and Sn. Interpretation of the findings for CO_2 reduction was informed by studies of the reduction of glyoxal and CO, key intermediates along the reaction pathway to final products. Density functional theory calculations show that the alkali metal cations influence the distribution of products formed as a consequence of electrostatic interactions between solvated cations present at the outer Helmholtz plane and adsorbed species having large dipole moments. The observed trends in activity with cation size are attributed to an increase in the concentration of cations at the outer Helmholtz plane with increasing cation size.

5.2 Introduction

The electrochemical reduction of CO_2 offers a means for storing electrical energy produced by renewable but intermittent resources, such as wind and solar radiation.[1, 2] Hydrocarbons and alcohols, rather than carbon monoxide and formic acid, are the preferred products of CO_2 reduction because of their high energy density. Despite extensive efforts aimed at identifying electrocatalysts that can produce these products, copper (Cu) remains the only material capable of doing so with significant yields.[3-5] Nevertheless, Cu requires a high overpotential (~−1 V versus RHE) and produces a broad spectrum of products.[6,7] Clearly, the discovery of novel means for reducing CO_2 to desirable products with higher efficiency and selectivity is needed. To do so requires understanding the fundamental processes occurring at the electrode surface. In addition to metal-adsorbate interactions, a full description of electrochemical reactions must include the effects of solvation and interfacial electric fields. A number of studies have shown that one way of influencing the product distribution is through changes in the electrolyte cation.[8-13]

The role of cations is particularly interesting because a number of studies have shown that both the activity and selectivity of Ag, Hg, and Cu for the CO_2 reduction reaction (CO_2RR) are influenced significantly by the size of the alkali metal cation in the electrolyte.[8-13] Similar effects have also been observed for the electrochemical reduction of oxygen, the oxidation of hydrogen, and the oxidation of low molecular weight alcohols.[14-18] For Ag and Hg, which are selective for CO_2 reduction to carbon monoxide (CO) and formate anions ($HCOO^-$), respectively, increasing the alkali metal cation size increases the rates of formation of these products.[8, 10, 11] For Cu, increasing alkali metal size leads to higher selectivities to C_2 products, e.g., ethylene and ethanol.[9, 12, 13] Explanations for these phenomena have been attributed to differences in local pH, or differences in kinetic overpotentials due to the electrochemical potential in the outer Helmholtz plane being affected by cation size.[8, 10, 11, 13]

One of the challenges to finding a consistent interpretation for the effects of cation size on the intrinsic kinetics of CO_2 reduction is that many studies are carried out under conditions where mass transport also contributes to the observed activity and product distribution. In recent study, we reported the effects of cation size on the rate of the CO_2RR under strong mass-transport limitations.[13] We showed that the increase in pH and the decrease in CO_2 concentration near the cathode, caused by inadequate mass transfer through the hydrodynamic boundary layer in front of the cathode, could be offset by the hydrolysis of solvated cations. We showed that the increased buffering effect of solvated cations with cation size could be captured theoretically and suggested that this effect is responsible for the observed changes in the overall current density and the distribution of product current densities with cation size. In this work, we present a combined experimental and theoretical study of the effects of electrolyte cation size on the intrinsic activity and selectivity of metal catalysts for the reduction of CO_2. In contrast to earlier studies, experiments were conducted at sufficiently low applied voltages to avoid the effects of concentration polarization of the electrolyte, so that the influence of cation size on the intrinsic activity and selectivity of each catalyst could be observed. Most of our work was conducted using epitaxially grown Cu(100) or Cu(111) thin films; a more limited study was carried out using polycrystalline Ag and Sn films. Density functional theory (DFT) calculations were used to investigate how cations and cation size affect the stabilization of reaction intermediates involved in the reduction of CO_2. These calculations demonstrate that adsorbed species with large dipole

moments oriented away from the solvent are stabilized by electrostatic interactions with solvated cations, while trends in activity with cation size arise from differences in ion concentration at the Helmholtz plane.

5.3 Experimental and computational methods

5.3.1. Electrode preparation

Single-side polished Si(100) or (110) wafers (Virginia semiconductor, 1-10 Ω cm) were diced into ~4 cm^2 sized pieces that were then used as electrode substrates. Prior to Cu deposition, the native oxide was removed from the Si substrates by submerging them in a 10% HF solution for 5 min. Immediately after HF etching, the Si pieces were transferred to a vacuum chamber for sputter deposition of Cu in an AJA ATC Orion-5 sputtering system. The base pressure of the sputtering system prior to deposition was ~$2x10^{-7}$ torr. The flow rate of the sputtering gas (Ar) was 25 sccm and the sputtering pressure was adjusted to $2x10^{-3}$ torr by controlling the speed at which the chamber was pumped, using a variable butterfly valve. Cu (99.999% Kurt Lesker) was deposited at a rate of 1 Å/s, as determined by a calibrated quartz crystal monitor, at ambient temperature. The total film thickness deposited was 100 nm. Polished, polycrystalline foils of Ag and Sn (99.99% Alfa Aesar) were also used as electrodes without further preparation.

5.3.2 Electrode characterization

The structure of the Cu thin films was characterized by X-ray diffraction. The orientation and epitaxial quality of the films were determined using symmetric θ-2θ scans, in plane ϕ scans, ω scans or rocking curves, and pole figures. XRD patterns were taken with a PANanalytical X'Pert diffractometer, which uses a Cu Kα (λ = 1.54056 Å) X-ray source. Symmetric θ-2θ scans were collected on samples fixed onto a flat glass slide in locked-coupled mode with a goniometer resolution of 0.001°. Measured diffraction patterns were compared to known standards taken from the International Center for Diffraction Data (ICDD) PDF4 database (card #71-4610 for Cu).

5.3.3 Electrochemical measurements

All electrochemical experiments were conducted in a gas-tight electrochemical cell machined from polyether ether ketone (PEEK).[19] The cell was cleaned with 20 wt. % nitric acid and oxidized in UV-generated ozone for 15 min prior to the initiation of an experiment. The working and counter electrodes were parallel and separated by an anion-conducting membrane (Selemion AMV AGC Inc.). A gas dispersion frit was incorporated into the cathode chamber to provide vigorous electrolyte mixing. The exposed geometric surface area of each electrode was 1 cm^2 and the electrolyte volume of each electrode chamber was 1.8 mL. The counter electrode was a Pt foil (99.9% Sigma Aldrich) that was flame annealed prior to each experiment. The working electrode potential was referenced against an Ag/AgCl electrode (Innovative Instruments Inc.) that was calibrated against a homemade standard hydrogen electrode (SHE). 0.05 M M_2CO_3 (M referring to an alkali metal cation) solutions were prepared by mixing ultra-pure salts (Sigma Aldrich 99.995%) and 18.2 MΩ DI, and were used as the electrolyte without further purification. The cathode chamber was sparged with CO_2 (99.999% Praxair) at a rate of 5 sccm for 20 min prior to and throughout the duration of all electrocatalytic measurements. Upon saturation with CO_2 the pH of the electrolyte was 6.8, which was maintained throughout the duration of electrolysis.

Electrochemical measurements were performed using a Biologic VSP-300 potentiostat. All electrochemical data were recorded versus the reference electrode and converted to the RHE scale. Potentiostatic electrochemical impedance spectroscopy (PEIS) was used to determine the uncompensated resistance (R_u) of the electrochemical cell by applying voltage waveforms about the open circuit potential with an amplitude of 20 mV and frequencies ranging from 50 Hz to 500 kHz. The potentiostat compensated for 85% of R_u *in situ* and the last 15% was post-corrected to arrive at accurate potentials. The electrocatalytic activity was assessed by conducting chronoamperometry at each fixed applied potential for 70 min.

5.3.4 Product analysis

The effluent from the electrochemical cell was passed through the sampling loop (250 μL) of an Agilent 7890B gas chromatograph equipped with a pulsed-discharge helium ionization detector (PDHID). He (99.9999% Praxair) was used as the carrier gas. The effluent of the electrochemical cell was sampled every 14 min. The gaseous products were separated using a Hayesep-Q capillary column (Agilent) connected in series with a packed ShinCarbon ST column (Restek Co.). The column oven was maintained at 50 °C for 1 min followed by a temperature ramp at 30 °C/min to 250 °C, which was maintained for the duration of the analysis. The signal response of the PDHID to each gaseous product was calibrated by analyzing a series of NIST-traceable standard gas mixtures (Air Gas).

The electrolyte from both electrode chambers was collected after electrolysis and analyzed using a Thermo Scientific UltiMate 3000 liquid chromatograph equipped with a refractive index detector (RID). The electrolyte aliquots were stored in a refrigerated autosampler until analyzed in order to minimize the evaporation of volatile products. The liquid-phase products contained in a 10 μL sample were separated using a series of two Aminex HPX 87-H columns (Bio-Rad) and a 1 mM sulfuric acid eluent (99.999% Sigma Aldrich). The column oven was maintained at 60 °C for the duration of the analysis. The signal response of the RID to each liquid-phase product was calibrated by analyzing standard solutions of each product at a concentration of 1, 10, and 50 mM.

5.3.5 Theoretical calculations

Plane-wave density functional theory (DFT) employing periodic boundary conditions was used for all calculations in this study. The Quantum ESPRESSO[20] code and the Atomic Simulation Environment (ASE)[21] were used, along with ultrasoft pseudopotentials and the Bayesian error estimation exchange-correlation functional with van der Waals interactions (BEEF-vdW).[22] This functional has been optimized for both chemisorption energies and long-range van der Waals interactions. For all calculations, a plane-wave cutoff of 500 eV and a density cutoff of 5000 eV were used, based on convergence tests from previous studies.[23] A Monkhorst-Pack[24] *k*-point grid of (4×4×1) was used for (3×3) cells while a (2×2×1) grid was used for (6×6) cells. All systems were modeled using a periodic Cu(111) slab, two ice-like water bilayers, the solvated ion and at least 12 Å of vacuum perpendicular to the surface. The field effect on various CO_2 adsorbates without ions or solvating waters was also investigated by applying a sawtooth potential in each simulation cell, for moderate field strengths where the vacuum energy remains above the Fermi level.[25]

Constrained minima hopping[26] (CMH) was used for the global optimization of water structures surrounding each solvated ion. CMH enforces molecular identity by constraining the

atomic distances within each molecular entity through Hookean constraints. The atoms are thermalized in a Maxwell-Boltzmann distribution at an initial temperature of 1000 K, then evolved through molecular dynamics and relaxed to locate new local minima. To save computational cost, CMH was performed on two layers of Cu. The Cu atoms were fixed, while all others were allowed to relax. The convergence criterion for the CMH was satisfied when three successive lowest energy minima were found within 0.05 eV of each other. Thereafter, the system was relaxed until the forces on all atoms were less than 0.05 eV/Å. Finally, the third layer of Cu was added back into the system to perform a single point calculation and obtain a more accurate value for the energy.

5.4 Results and discussion

5.4.1 Cation effects on Cu(100) and Cu(111) oriented films

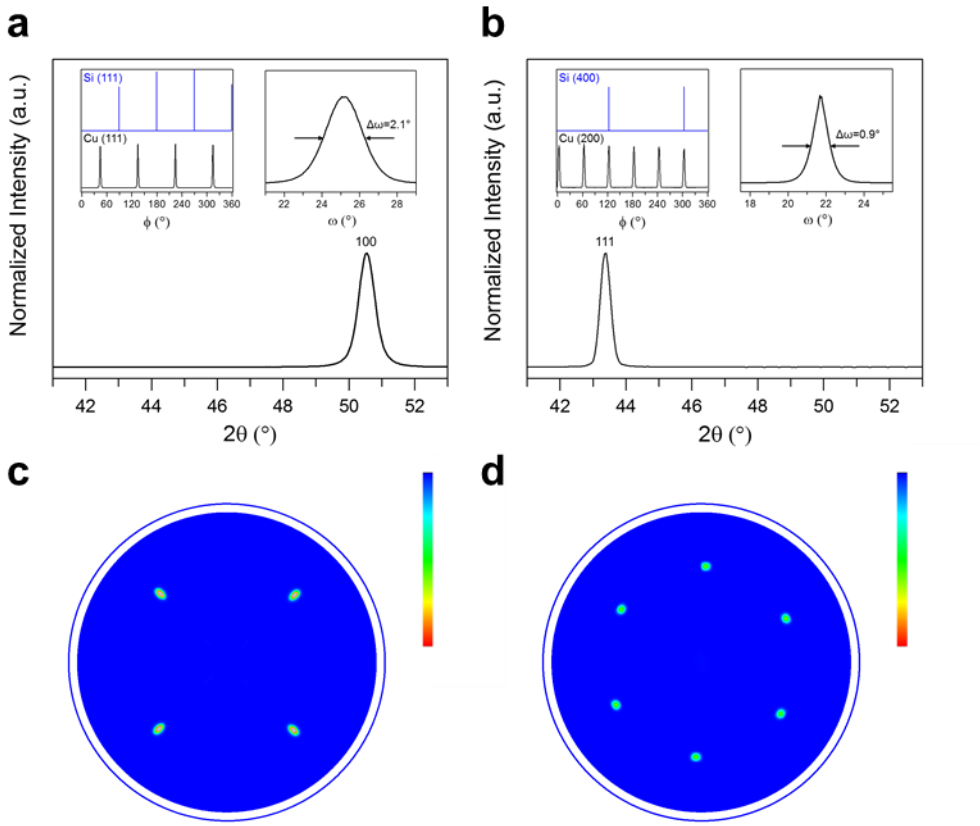

Figure 5.1: Structural characterization of oriented Cu thin films. a) Symmetric θ-2θ, in plane ϕ, and ω rocking curve scans for Cu deposited on Si(100). b) Symmetric θ-2θ, in plane ϕ, and ω rocking curve scans for Cu deposited on Si(110). c) Cu(111) pole figure for Cu deposited on Si(100). d) Cu(200) pole figure for Cu deposited on Si(110).

Epitaxially grown Cu thin films were used as electrocatalysts in order to have well-defined catalytic surfaces.[27] These films were prepared by radio-frequency sputtering of Cu onto silicon (Si) single crystal substrates, taking advantage of the epitaxial relationship between Cu and Si substrates of different orientations.[27-28] Most of our studies were conducted on the Cu(100) surface because it has been shown that polycrystalline Cu consists mostly of (100) oriented crystallites and the Cu(100) surface has a higher selectivity to more desirable products such as C_{2+} hydrocarbons and oxygenates (e.g., ethylene and ethanol).[29-32] Symmetric θ-2θ XRD patterns of 100 nm thick Cu films deposited on Si(100) and Si(110) substrates are shown in Figure 1. The observation of a single Cu(200) diffraction peak for Cu deposited on Si(100) indicates that the film is oriented with the (100) crystallographic direction normal to the film plane. Similarly, for Cu deposited on Si(110) only the diffraction peak associated with Cu(111) is observed.[27-28] While symmetric XRD scans establish the out-of-plane texture relationships, both out-of-plane and in-plane texture analyses are necessary to determine whether the Cu thin films grow epitaxially on Si, as a film with strong fiber texture would show a similar diffraction pattern. To this end, in plane-texture analysis was conducted using X-ray pole figures. Pole figures represent the texture of a material and show the distribution of particular crystallographic directions in a stereographic projection. The Cu(111) X-ray pole figure for Cu(100) on Si(100) exhibits discrete Bragg reflections, indicating cube-on-cube epitaxial growth of Cu on the Si(100) substrate. Four-fold symmetry is observed for the Cu(111) Bragg reflections with an azimuthal angle of 90° apart, which is expected for a Cu (100) single-crystal. For Cu (111) on Si (110), six-fold symmetry is observed for the Cu (200) Bragg reflections, indicating both strong out-of-plane and in-plane texture and thus epitaxial growth on the Si(110) substrate (Figure 1a). Six diffraction spots in the pole figure are seen instead of three because there are two discrete sets of crystallites from twinning with an azimuthal angle of 60° apart. These results demonstrate that Cu thin films can be grown epitaxially with both (100) and (111) orientations.

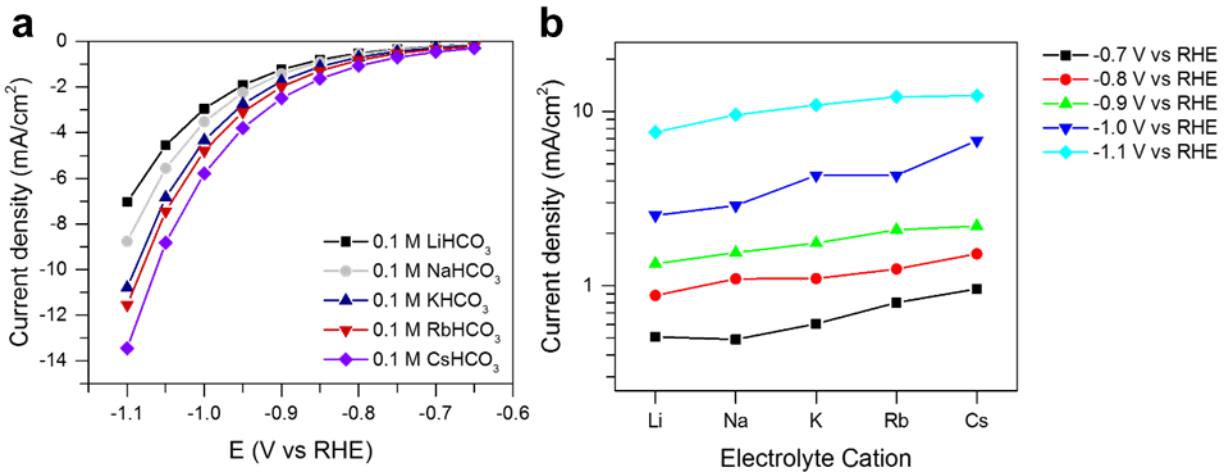

Figure 5.2: Effect of alkali metal cations on the total activity over Cu(100). a) Linear sweep voltammograms for CO_2 reduction on Cu(100) in CO_2 saturated 0.1 M bicarbonate electrolytes containing different metal cations. b) Average current densities obtained during bulk electrolysis as a function of metal cation at different potentials.

The steady state activity and selectivity of the Cu(100) surface was investigated in CO_2-saturated bicarbonate electrolytes containing different alkali metal cations, by using potentiometric electrolysis at potentials from −0.7 to −1.1 V vs the reversible hydrogen electrode (RHE). Figure 2 shows the total current density as a function of electrolyte cation at various potentials. From both steady state potentiostatic and potential sweep measurements, it is clear that the total current density increases with cation size, and this trend is observed at all applied potentials. To identify the contributions to the increase in the total current density, we examined the effects of cation size on the product distribution. As large differences in total current density exist for electrolytes containing different cations, partial currents provide a better representation of trends in product formation rates than faradaic efficiencies.

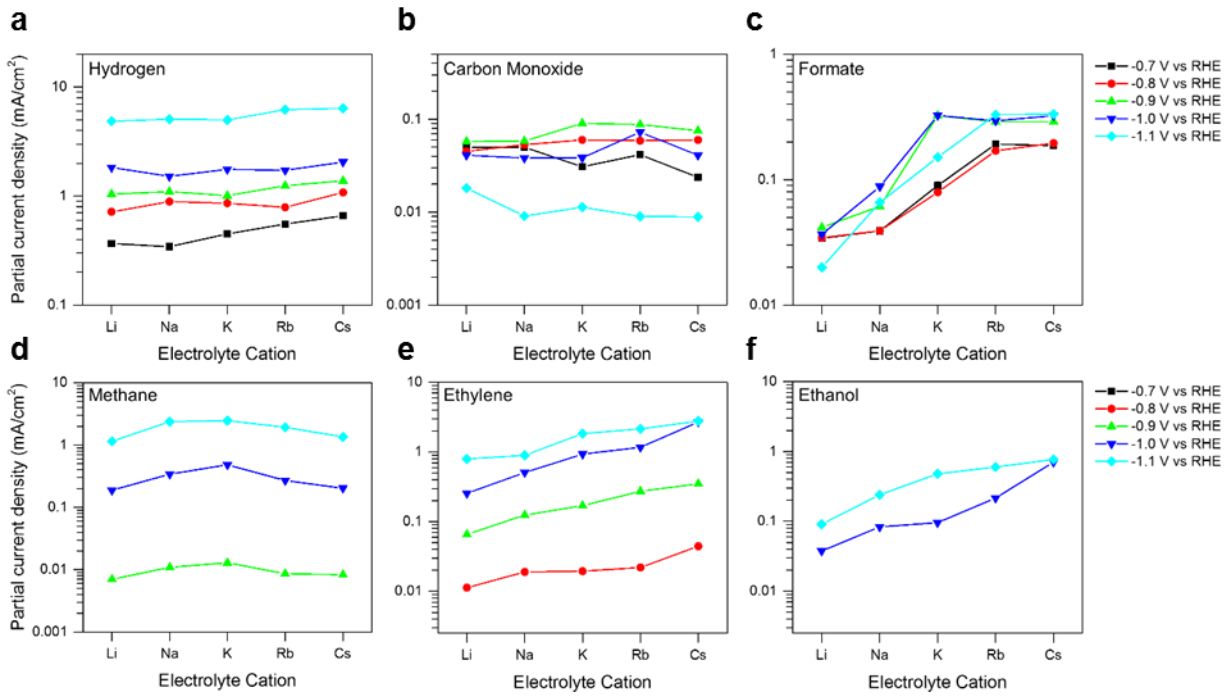

Figure 5.3: Cation effect on the rates of formation of major products of CO_2 reduction over Cu(100). Partial current densities for each of the major products as a function of the electrolyte metal cation on Cu(100). Data are presented at potential between −0.7 to −1.1 V vs RHE.

Figure 3 shows the partial current density for each of the major products as a function of electrolyte cation. Formation rates of minor liquid products can be found in Table 1. A key finding is that the production rates of hydrogen and carbon monoxide are relatively unaffected by increasing cation size, whereas the rates of formate, ethylene, and ethanol formation increase monotonically with increasing cation size. The rate of methane production reaches a maximum for Na^+- and K^+- based electrolytes and is lower in all other electrolytes. The trends seen in Fig. 3 are consistent with previous amperometric measurements.[9] It is notable that these trends are independent of the applied overpotential.

Product/ Cation	Li	Na	K	Rb	Cs
Glyoxal	0	0	4.30E-03	5.59E-03	6.82E-03
Acetate	0	0	1.51E-02	1.42E-02	4.23E-02
Glycolaldehyde	0	0	9.90E-03	4.30E-03	2.87E-02
Acetaldehyde	0	0	2.71E-02	4.52E-02	5.66E-02
Hydroxyacetone	0	0	0	5.59E-03	6.82E-03
Allyl Alcohol	9.89E-03	9.54E-03	8.14E-02	8.65E-02	8.19E-02
Proprionaldehyde	2.23E-02	2.37E-02	6.37E-02	5.08E-02	6.55E-02
Propanol	3.88E-02	7.57E-02	1.68E-01	2.30E-01	3.34E-01

Table 5.1: Partial current densities (mA/cm^2) for minor liquid products for electrochemical reduction of CO_2 on Cu (100). Displayed at a potential of -1.0 V vs RHE

To probe the effects of mass transport limitations, the CO_2 flow rate into the electrochemical cell was varied. As the CO_2 flow rate is increased, the hydrodynamic boundary layer thickness will decrease, resulting in a larger maximum diffusive flux of CO_2 to the electrode surface. At low reaction rates (i.e., low current densities), for which diffusion of CO_2 is sufficiently rapid to prevent depletion at the cathode surface, increasing the flowrate of CO_2 should have no effect on catalyst activity. Whereas under mass transport limited conditions, increased reactant availability will affect the product distribution measured.[13, 32] Figure 4 shows that doubling the CO_2 flow rate from 5 to 10 sccm has no impact on the measured selectivity or activity of Cu (100) at −0.9 V vs RHE and −1.0 V vs RHE. However, at −1.1 V vs RHE, doubling the CO_2 flowrate decreases the faradic efficiency to H_2 and CH_4 and increases the faradaic efficiency for C_{2+} products. As shown previously, these trends are due to the increased rate of mass transfer at higher gas flowrates, which improves the supply of CO_2 to the cathode.[32] Therefore, the effects of cation size on the partial current densities observed in Figure 3 at potentials more positive than ~ −1.0 V vs RHE are ascribable to the influence of cation size on the intrinsic kinetics of Cu(100), particularly for the formation of formate, ethylene, and ethanol, and to a lesser degree, methane.

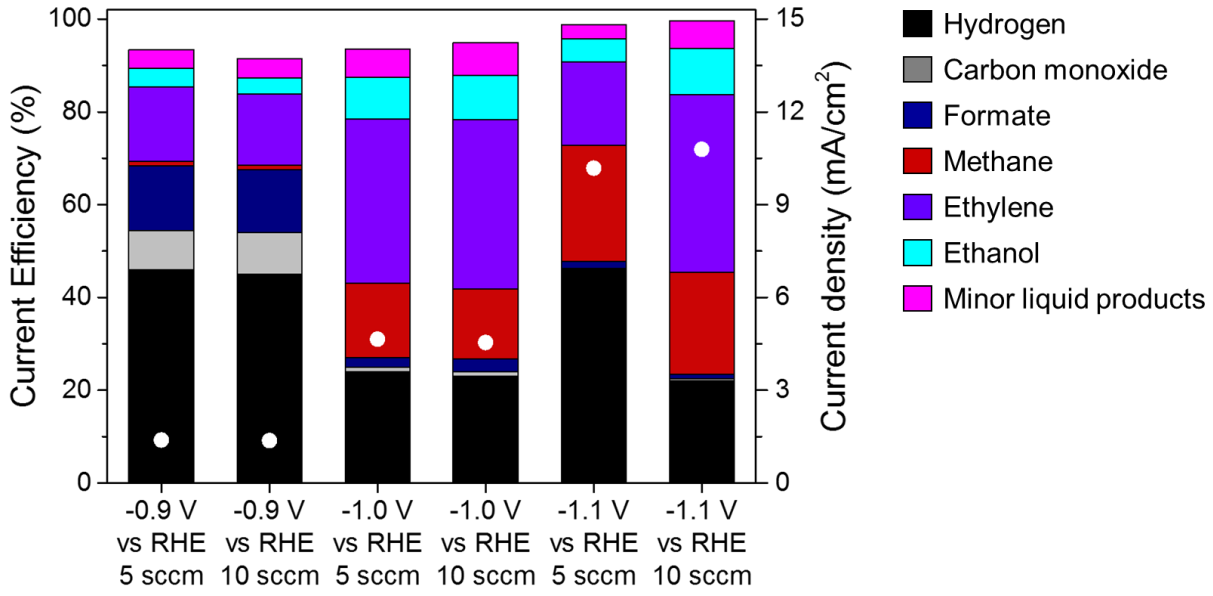

Figure 5.4: CO_2 flow rate studies for probing external mass transport limitations: Current efficiency (bars) and total current density (dots) for CO_2 reduction over Cu(100) at different flow rates of CO_2.

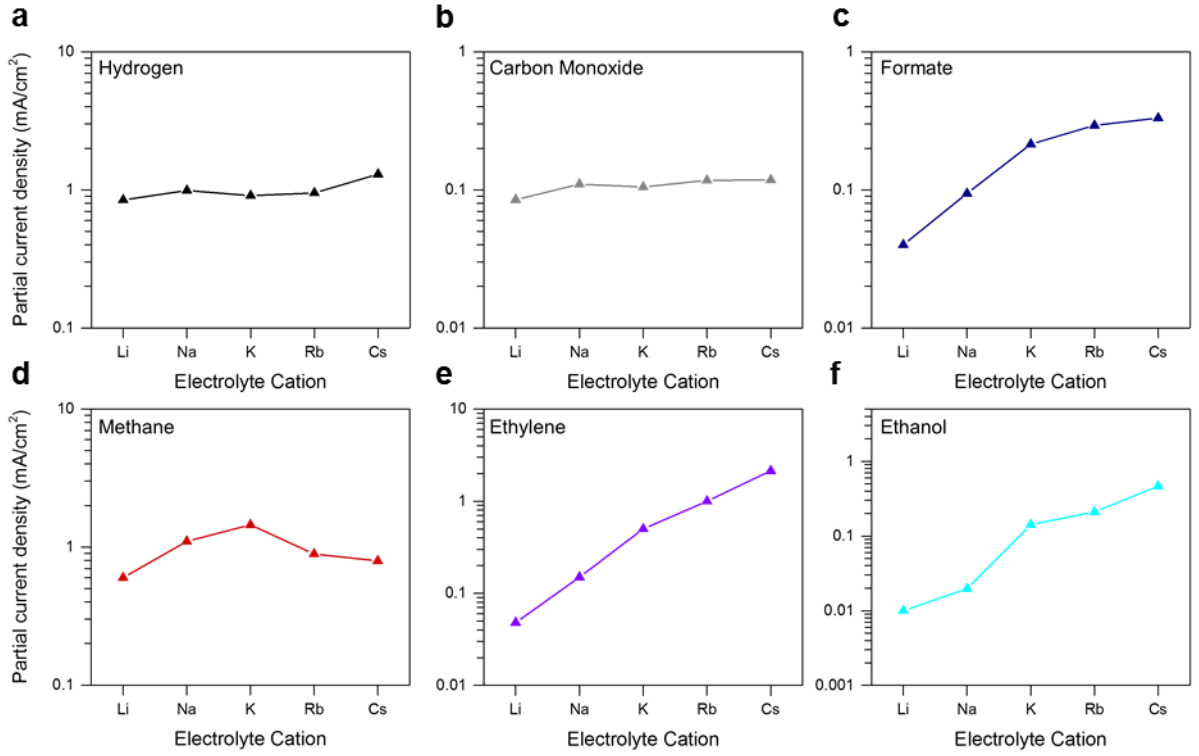

Figure 5.5: Cation effect on the rates of formation of major products of CO_2 reduction over Cu(111). Partial current densities for each of the major products as a function of the electrolyte metal cation on Cu(111). Data are presented for the potential of -1.0 V vs RHE.

The effects of cation size were also investigated for CO_2 reduction over a Cu(111) surface and the results are presented in Fig. 5. The trends with increasing cation size for the close-packed Cu(111) surface are consistent with those observed for the Cu(100) surface. Partial currents to $HCOO^-$, C_2H_4, and C_2H_5OH increase with increasing cation size while rates of formation of H_2, CO, and CH_4 are less affected by cation size. However, the effect of cation size is more pronounced on the close-packed surface, resulting in high selectivity (~40% FE) to C_2H_4 in $CsHCO_3$ even on a Cu(111) surface, which is known to be more selective for producing CH_4 than C_2H_4 in K^+-containing electrolytes.[29, 31, 33-36]

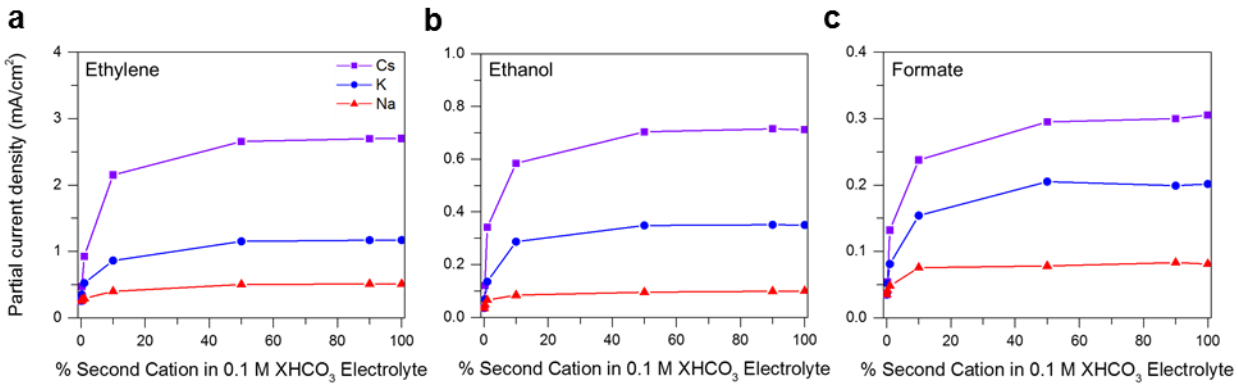

Figure 5.6: Relative effects of alkali metal cations. Partial currents for ethylene, ethanol, and formate formation as a function of the electrolyte composition on Cu(100). Data are presented for a potential of −1.0 V vs RHE. A mixture of $LiHCO_3$ and $XHCO_3$ electrolyte is used with X being Na, K, Cs (second cation). A fixed total salinity of 0.1 M was used in all experiments.

5.4.2 Relative effects of alkali metal cations

To further investigate the effects of the alkali metal cations, electrolysis was performed with mixtures of small (Li^+) and larger (Na^+, K^+, Cs^+) cations in the electrolyte, maintaining the total salinity at 0.1 M. The results are shown in Figure 6. It is evident that the composition of the electrolyte has a noticeable effect on the partial currents for $HCOO^-$, C_2H_4, and C_2H_5OH. No significant effect on the partial currents of H_2, CO, and CH_4, was observed. For the latter three products, the effect of the larger cation dominates that of the Li^+ cation, and even at relatively low percentages of the larger cation. Conversely, an electrolyte mixture that is dilute in the smaller cation results in identical selectivity to a solution that does not contain the small cation. These results suggest that the concentration of larger cations near the cathode surface is larger and/or that the larger cations have a much more significant promotional effect on the production of C_2H_4, C_2H_5OH, and $HCOO^-$.

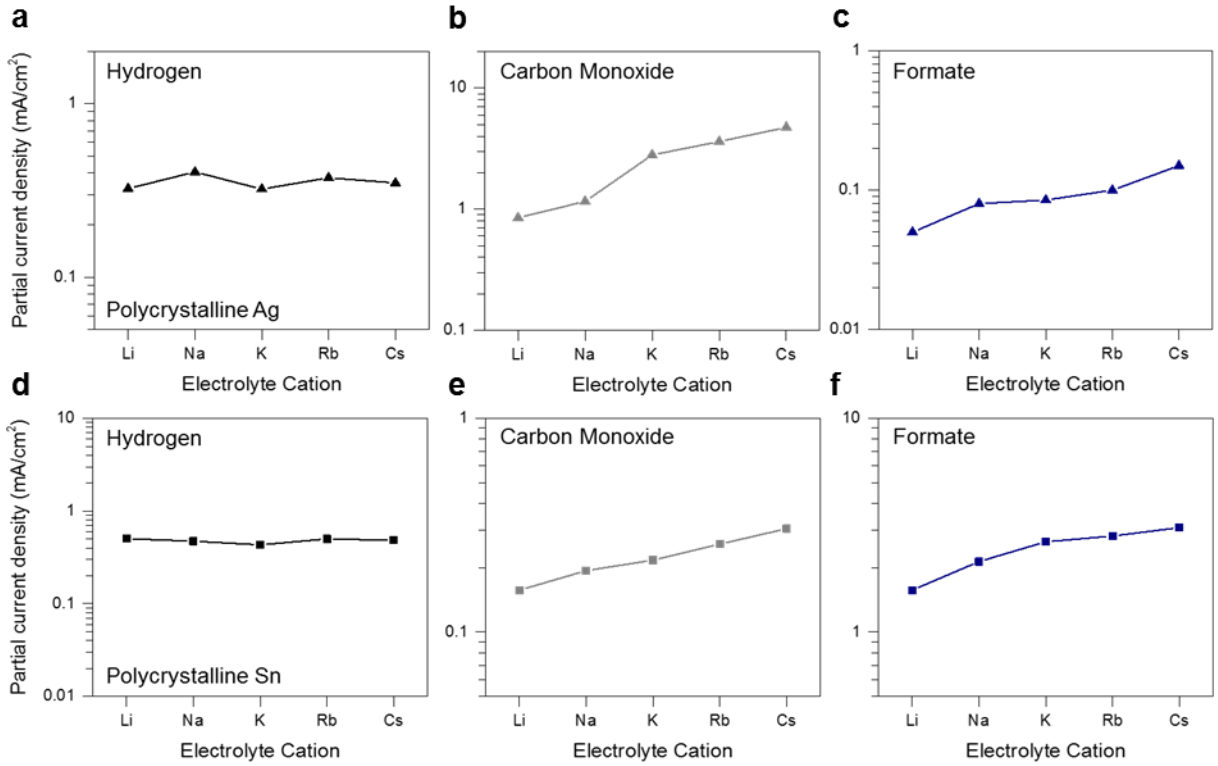

Figure 5.7: Cation effect on two electron products. Partial currents for each of the major products as a function of the electrolyte metal cation on polycrystalline Ag and Sn. Data are presented for a potential of -1.0 V vs RHE.

5.4.3 Cation effect on polycrystalline Ag and Sn

As carbon monoxide is a reaction intermediate which undergoes further reduction on Cu, the production rate of CO itself is less straightforward to interpret than that of the other major products.[37] Therefore, to investigate the effect of cation size on CO production, and to provide further insights into the trends observed for Cu(100) and Cu(111), experiments were conducted on polycrystalline Ag and Sn foils—metals that selectively produce CO and $HCOO^-$, respectively.[3, 38] As seen in Fig. 7, the current densities for CO and $HCOO^-$ production on both metals increases with cation size. This suggests that increasing cation size facilitates activation of CO_2. Here again, we see that as with Cu(100) and Cu(111), the rate of H_2 evolution is unaffected by cation size. These trends are also consistent with previous literature reports.[8-11, 13, 39]

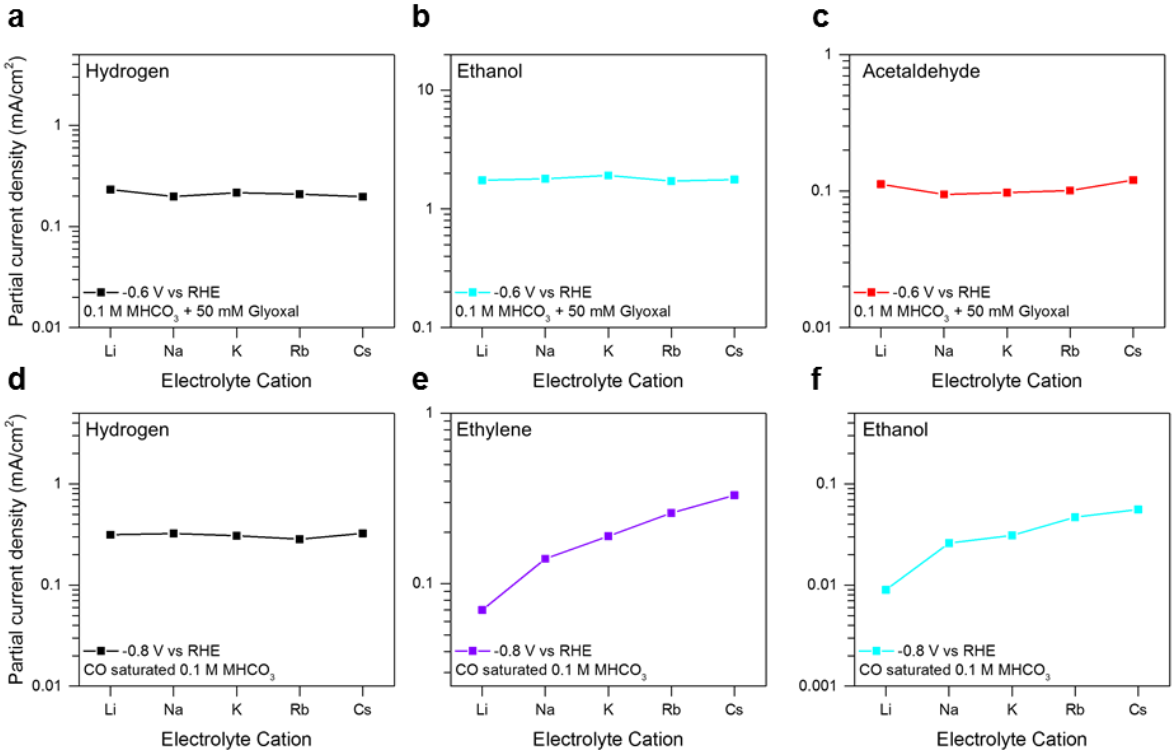

Figure 5.8: Cation effects of the reduction of reaction intermediates. a-c) Partial currents for hydrogen, ethanol, and acetaldehyde formation from the reduction of glyoxal on Cu(100). Data is presented at a potential of -0.6 V vs RHE. d-f) Partial currents for hydrogen, ethylene, and ethanol formation from the reduction of CO on Cu(100). Data is presented at a potential of -0.8 V vs RHE.

5.4.4 Cation effects on elementary reaction steps: reduction of intermediates

As shown above, the size of the electrolyte cation influences the formation of C_2 products. Recent theoretical studies suggest that C-C bonds are formed via the reaction of two molecules of adsorbed CO or by the reaction of adsorbed CO with a formyl group, HCO.[40] A recent study has shown that the latter process dominates at applied potentials near –1 V and leads to the formation of adsorbed HC(O)-C(O) species, which then undergoes hydrogenation to form C_2H_4 or CH_3CHO and C_2H_5OH.[40] Experimental studies suggest that the precursor to CH_3CHO and C_2H_5OH is glyoxal (OHC-CHO).[41] Therefore, to investigate which steps in the formation of C_2 products are affected by the electrolyte cation size, we carried out experiments in electrolyte containing glyoxal. As shown in Figure 8, cation size has no effect on the partial currents of CH_3CHO and C_2H_5OH formation, which in this case require no C-C bond formation as glyoxal is the starting reagent. Consistent with previous observations, no C_2H_4 was observed during the hydrogenation of glyoxal.[41] These findings strongly suggest that the size of the electrolyte cation affects the rate of C-C bond formation, the rate increasing with increasing cation size, but has a negligible effect on the hydrogenation of glyoxal to CH_3CHO and C_2H_5OH.

As larger cations facilitate CO_2 activation, evidenced by the increase in rates to CO and $HCOO^-$ (see Figure 3), experiments were carried out in electrolyte solutions saturated with CO but free of dissolved CO_2, in order to assess whether an increase in the surface coverage of adsorbed CO relative to adsorbed H favors C-C coupling. Consistent with the results for CO_2

reduction over Cu(100), no change in methane activity with cation size was observed from CO reduction at −1 V vs RHE. Figure 8b clearly shows that the rates of C_2H_4 and C_2H_5OH formation increase with increasing cation size. We note that the magnitude of this effect is comparable to that observed during the reduction of CO_2, which shows that the effect of cation size on the formation of multicarbon products cannot be ascribed solely to more facile CO_2 activation.

5.5 Discussion

5.5.1 Cation promoter effects

The data presented in this study demonstrate that the size of the alkali metal cations in the electrolyte affects the intrinsic rates of formation of certain reaction products. On Cu (100) and Cu (111), these effects are most notable for $HCOO^-$, C_2H_4, and C_2H_5OH; over polycrystalline Ag and Sn, the effects of cation size are observed for the formation of CO and $HCOO^-$. It is also shown that larger cations have a stronger effect than smaller cations, and that only a small fraction of the larger cation is needed in the electrolyte to observe its influence. Trends in the partial current densities derived from the studies of the reduction of key reaction intermediates (OHCCHO and CO) suggest that the elementary steps promoted by the presence of metal cations are the activation of CO_2 and the initial C-C coupling, whether through CO dimerization or CO-CHO coupling, and not the hydrogenation of C_2 intermediates leading to ethylene and ethanol.

We propose that the energetics for the formation of $HCOO^-$ and C_2 products are influenced by the presence of hydrated alkali ions located at the edge of the Helmholtz plane, and that the observed effects of cation size are attributable to differences in the cation concentration in the outer Helmholtz plane. This explanation is supported by DFT calculations performed using minimum energy structures of solvated cations at the interface. Since both Cu(100) and Cu(111) surfaces show consistent trends in activity with respect to alkali cation size, the close-packed Cu(111) surface was chosen for the DFT simulations, which has also been frequently used in previous theoretical CO_2R studies[42-45] and where the water structure is more well-defined.[46]

Because the potentials applied during CO_2 reduction are much more negative than the potential of zero charge (PZC) of the low-index facets of Cu ~ $-0.7V_{SHE}$ [47], solvated cations should accumulate near the surface of the electrode during reaction.[40, 48] Given the very negative reduction potentials of alkali ions, they do not chemisorb under CO_2 reduction conditions. There is also evidence from studies of oxygen reduction that the cations remain partially solvated at the interface.[49] The presence of the cation at the metal surface gives rise to high electric fields of ~ −1 V/Å in the vicinity of the ion.[25, 50] In contrast to classical continuum models of the electrochemical interface, the fields are highly localized when the structure of the cation and solvating waters is modeled explicitly. Refs. [25, 50] show that such fields extend roughly 5 Å from the center of the solvated cations and outside of this region decay to zero.

The strength of the adsorbate-field interaction can be probed qualitatively by the application of a uniform field in vacuum. This approach circumvents the challenge of finding a

global minimum in the water and solvated cation structure in the presence of various adsorbates on the surface, which introduces many more degrees of freedom than standard atomistic computations in heterogeneous catalysis. It has also been shown previously that the effect of alkali promoters in heterogeneous catalysis can be modeled approximately by the effect of a uniform field.[51] The interaction energy between an adsorbate and a uniform electric field at the interface is given by[52]

$$\Delta E = \mu\epsilon - \frac{1}{2}\alpha\epsilon^2 + \cdots \quad , \qquad (1)$$

where μ and α are the dipole moment and the polarizability (respectively) of the adsorbate, and ε represents the electric field. Adsorbate dipoles oriented in the opposite direction of the field will be stabilized, and vice versa.

Figure 9 shows the field stabilization for various adsorbates that have been proposed to be involved in the electrochemical reduction of CO_2 on Cu(111).[43, 49, 52] The change in adsorption free energy for each species was determined by applying a uniform field oriented perpendicular to the surface in vacuum.[43] The corresponding values of μ and α, determined by fitting Eq. (1) the calculated data, are given in Table 2. We note that H* does not have a significant value of μ and is not affected by the electric field, which is consistent with previous experimental studies that have shown that hydrogen adsorption is unaffected by the identity of the cation in solution.[14-16] Since the energy for hydrogen adsorption is a descriptor for the hydrogen evolution activity on metals, the rate for hydrogen production should also be relatively insensitive to the identity of the cation, consistent with the experimental data presented here.[53] Recent calculations of the electrochemical barriers for CO_2 reduction using an explicit solvent model have shown that reduction of *CO to form *CHO is the limiting step for CH_4 formation.[43] Since the value of μ for *CHO is zero, the cation-induced field would stabilize *CO and therefore increase the energy barrier for hydrogenation to *HCO, the rate-limiting step on the path to CH_4 formation. Therefore, CH_4 formation should occur in regions of the catalyst that are not strongly influenced by the cations located at the outer Helmholtz plane, and correspondingly the partial current density for CH_4 should not be strongly affected by cation identity, which is consistent with the trend in the experimental data shown above.

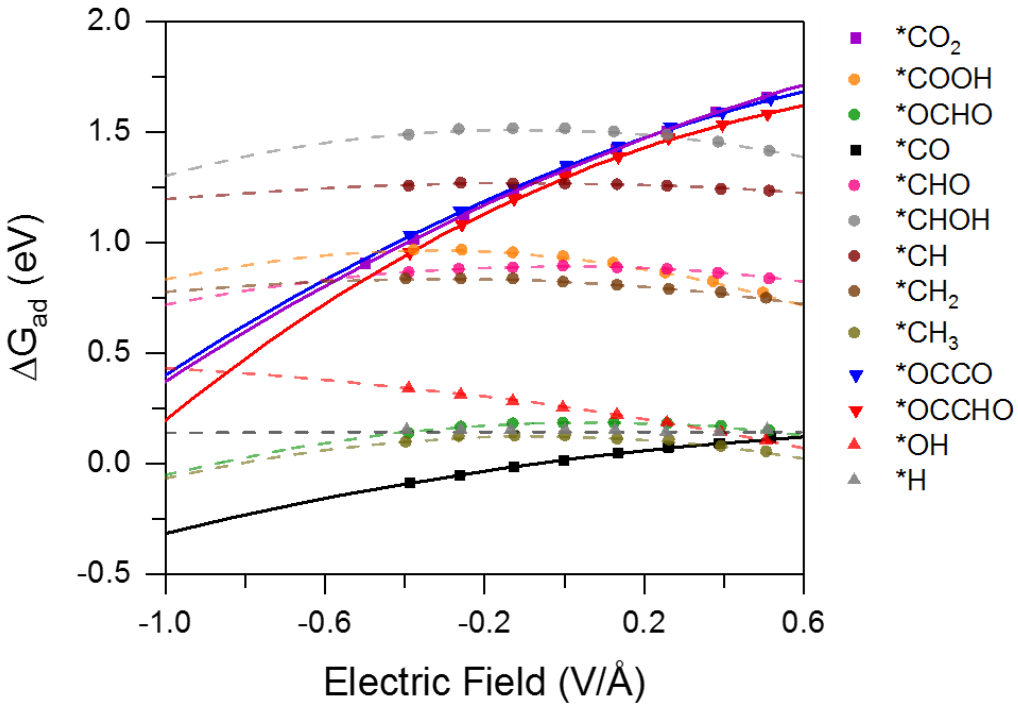

Figure 5.9: Field effects on various CO_2R intermediates on Cu(111). The energy of each adsorbate is plotted as a function of field strength, which is obtained by applying a uniform electric field oriented perpendicular to the slab. The curves are fit to Equation (1) and the corresponding dipole moment μ and polarizability α of the adsorbates are given in Table 2. Solid curves highlight the adsorbates that are most strongly affected by an electric field. Adsorbates with positive dipole moments μ (oriented in the direction opposite to the electric field) are stabilized, while adsorbates with negative μ (aligned with the electric field) are destabilized.

Table 5.2 Dipole moments and polarizabilities of adsorbates on Cu(111), determined with Eq. (1)

Adsorbate	μ (eÅ)	α (eÅ^2/V)
*CO_2	0.76	0.40
*COOH	−0.19	0.60
*OCHO	0.04	0.42
*CO	0.23	0.22
*CHO	0.00	0.36
*OCCO	0.66	0.54
*OCCHO	0.75	0.74
*CHOH	−0.05	0.52
*CH	−0.02	0.18
*CH_2	−0.08	0.26
*CH_3	−0.03	0.44
*OH	−0.26	0.14
*H	0.00	0.00

For adsorbates containing C=O bonds oriented perpendicular to the surface—in particular, *CO_2, *OCCO, and *OCCHO—the field stabilization should be large, ~ 1 eV for fields of ~ −1 V/Å in the vicinity of the cations. As shown in Table 2, these species have the largest dipole moments. Previous theoretical calculations have shown that on weakly binding metals such as Ag, the field-induced stabilization of *CO_2 is crucial for the activation of CO_2 to form CO.[25] The barrier for the hydrogenation of *CO_2 to *COOH is generally very small,[54] so stabilization of *CO_2 should increase the coverage of *COOH. The *COOH species can undergo further hydrogenation to form HCOOH or *CO. The chemical hydrogenation barriers for *COOH to form HCOOH are surmountable at 0.69 eV and 0.75 eV on Cu(111) and Cu(211) respectively, and 0.46eV on Ag(211),[23] consistent with increased HCOOH production observed on all of the surfaces investigated. For weakly binding metals such as Ag and Sn, the field effect would promote $CO_{(g)}$ production, whereas for moderate to strongly binding metals such as Cu and Pt, *CO produced in the vicinity of a cation would also be field stabilized, thereby decreasing its desorption rate and increasing its *CO coverage there.

On Cu surfaces, formation of the initial intermediates to C_2 products are also field-assisted. The greater stabilization of the *OCCO relative to 2**CO in the presence of a cation is due to the differences in the dipole moments of the product and reactant species,[36] which has the effect of lowering the barrier to C-C bond formation. In the absence of the cation-created electrostatic field and effects of solvation by water, the barrier for this process is not surmountable at room temperature.[55] At higher overpotentials, where *CHO can be produced, *CO-*CHO coupling would also be a feasible route towards C_2 products, and the corresponding barrier should be similarly field-stabilized due to the large dipole on *OCCHO, as shown in Figure 9.[40] Since the formation of glyoxal via addition of a hydrogen atom to *OCCHO is the first step along the path to forming ethylene and ethanol, the observation (see Figure 8) that the selectivity of products derived from glyoxal is independent of cation size suggests that the rate-determining step in formation of C_2 products occurs at the point of C-C bond formation and prior to formation of glyoxal.[54] The net effect of increased CO production, CO coverage and C-C coupling on Cu on field-stabilized sites results in a net non-monotonic trend in the partial current density for CO with cation size.

While the influence of the cation-induced field at the catalyst surface can explain the role of cations in promoting elementary steps in the reduction of CO_2 that involve strong dipole moments, it does not explain the observed trend with cation size. We therefore explored the possibilities that this effect is due to disparities in the magnitude of the electrostatic field induced by cations of different size and/or an increase in the concentration of solvated cations at the outer Helmholtz plane as a function of size.

Constrained minima hopping[26] (CMH) was used to obtain the optimized structure of water surrounding each solvated ion on Cu(111). Figure 10 shows that the calculated fields in the vicinity of adsorbed CO (*CO) do not show a systematic variation with cation size. Moreover, any differences in the binding energy of intermediates induced by cations would give rise to exponential differences in current density, which we do not observe.

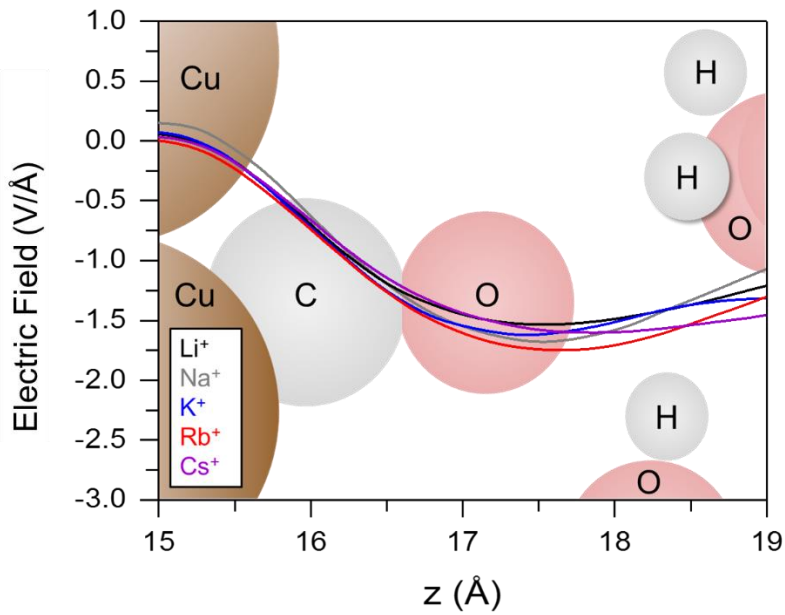

Figure 5.10. Electric field distribution near the center of the adsorbate plotted as a function of the *z*-coordinate of the simulation cell for the 2 *CO initial state. The geometry of an example structure is overlaid to clearly illustrate the position of the adsorbate. The cell is viewed from the side and rotated 90°. The minimum *z* value is taken at the Cu surface and the *z*-position of the solvated cations is roughly at 20 Å and not included in the overlay.

We hypothesize, therefore, that the ion specificity arises from an increase in the concentration of cations at the outer Helmholtz plane with increasing cation size. To determine the driving force for each cation toward the Helmholtz plane from bulk solution, we used these globally optimized solvation structures for each cation and calculated the energy required to move a solvated cation from the bulk of the electrolyte to a fixed distance of 6.25 Å above the Cu(111) surface the (see the SI for details). Figure 11 shows this energy change with the cathode potential relative to that for Li^+, $\Delta\Delta E$. The potential U vs SHE is determined through:

$$U = \frac{\Phi - \Phi_{SHE}}{e} \qquad (2)$$

where Φ is the work function of the interface and Φ_{SHE} is that corresponding to the standard hydrogen electrode, determined experimentally to be ~4.4eV.[56] The value of $\Delta\Delta E$ becomes more negative with increasing cation size, its magnitude increasing in the order $Li^+ < Na^+ < K^+ < Rb^+ < Cs^+$. Therefore, the driving force for each cation to be at the Helmholtz plane relative to the bulk electrolyte increases with cation size. This trend suggests that the concentration of cations at the outer Helmholtz plane should increase with increasing cation size, leading to increased product current densities. Consistent with this reasoning, we observed (see Figure 6) that at a constant cation concentration, replacement of even a small fraction of Li^+ by Cs^+ results in a shift in the product distribution from one characteristic for Li^+ to one characteristic for Cs^+. This supports the hypothesis that there is a stronger driving force for Cs^+ to be at the Helmholtz plane compared to Li^+. Without this stronger driving force on Cs+ to be in the Helmholtz plane, the trends in Figure 6 would be linear.

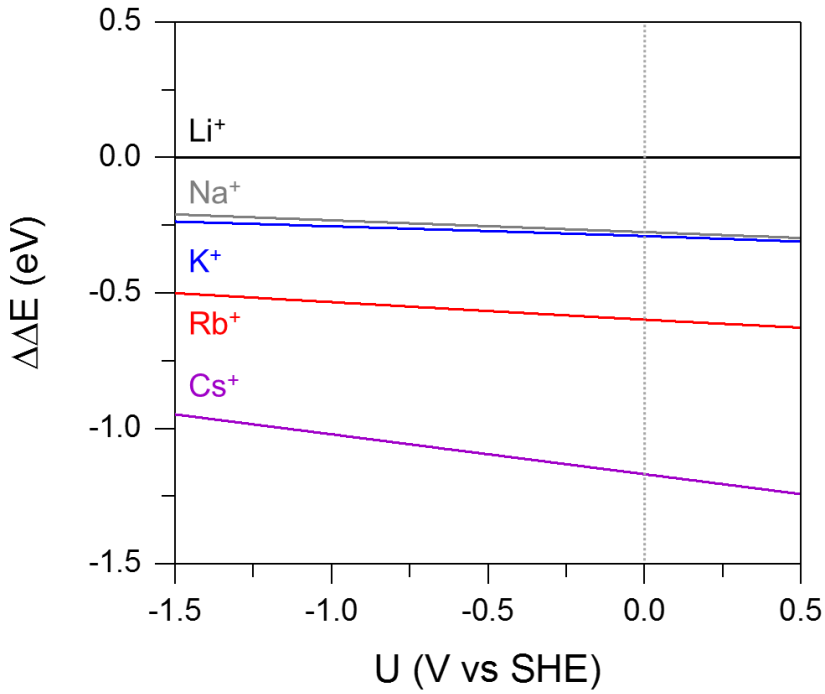

Figure 5.11: The change in energy for bringing a solvated cation from bulk electrolyte to the outer Helmholtz plane at the Cu (111) facet for different cations shown as a function of the standard hydrogen electrode (SHE) potential. All energies are referenced to that for the Li^+ cation. The dependence of these energies on cathode potential results from the partial electron transfer to the ion upon migration from the bulk to the Helmholtz plane, and is reflected in Eq. 5. This energy becomes more negative with increasing ion size, suggesting a greater concentration of larger cations in the outer Helmholtz plane and giving rise to increased product current densities. The vertical dotted line indicates the potential for the standard hydrogen electrode.

5.6 Conclusions

The present study investigated the effects of electrolyte cation size on the activity and selectivity of metal catalysts used for the electrochemical reduction of CO_2. The experimental work was conducted under conditions where the influence of electrolyte concentration polarization was negligible in order to avoid the additional influence of changes in pH and the consequent effects on the concentration of CO_2 near the cathode surface. For polycrystalline Ag and Sn, increasing the size of the alkali metal cation in the electrolyte increases the partial current densities for $HCOO^-$ and CO, but has no effect on the partial current density for H_2. Similar experiments conducted using Cu(100) and Cu(111) oriented films deposited on crystalline Si(100) and(111) surfaces show an increase in the current densities for $HCOO^-$, C_2H_4, and C_2H_5OH but little to no effect on the partial current densities for H_2, CO, and CH_4 as the size of the electrolyte cation is increased.

The observed effects are interpreted on the basis of DFT calculations. Hydrated alkali metal cations in the outer Helmholtz plane create a dipole field of the order 1 V/Å, which can stabilize the adsorption of surface intermediates having significant dipole moments (e.g., *CO_2, *CO, *OCCO). This field stabilization decreases the energy for the reduction of *CO_2 adsorption, the precursor to two-electron products, and C-C coupling to form *OCCO or *OCCHO, the precursor to C_2H_4 and C_2H_5OH. Calculations of the stability of the solvated cation in the Helmholtz plane indicate that larger hydrated cations are more energetically favored at the outer Helmholtz plane than smaller ones, which suggest a larger coverage of cations as cation size increases. This result is consistent with the experimental observation that a small percentage of larger cations has a large effect on product distribution.

These findings are consistent with the trends in partial current for C_1 products observed on polycrystalline Ag and Sn and on Cu(100) and Cu(111) surfaces, and for C_2 products observed on Cu(100) and Cu(111) surfaces. Also consistent with the conclusions drawn from the theoretical analysis is that cation size affects the partial currents for C_2H_4 and C_2H_5OH produced during the electrochemical reduction of CO over Cu(100) but has no influence on formation of these products upon reduction of glyoxal. The absence of cation size effect on the partial current for H_2 produced on Ag, Sn, Cu(100), and Cu(111) is attributed to the absence of a dipole for *H. Similarly, no effect of cation size on the formation of CH_4 on Cu(100) and Cu(111) surfaces is expected since the field of a cation would tend to stabilize *CO more than *CHO, thereby increasing the energy for *CO hydrogenation to *CHO, the rate-limiting step leading to CH_4.

Finally, we note that differences in the effects of electrolyte cation size on the formation of CO on Ag and Sn vs. Cu(100) and Cu(111) are attributable to the following considerations. For Ag and Sn, CO is a final product, and therefore only influenced by its formation by hydrogenation of *COOH which should have an increased coverage from the field-stabilization of *CO_2. In contrast, for Cu(100) and Cu(111), *CO is an intermediate in the formation of CH_4. Since the dipole electrostatic field created by hydrated cations accelerates both the formation and consumption of *CO, there is no observable effect of cation size on the partial current for CO on Cu(100) and Cu(111).

5.7 References

1. Lewis, N. S.; Nocera, D. G. *Proc. Natl. Acad. Sci.* **2006,** 103, (43), 15729-15735.
2. Chu, S.; Majumdar, A. *Nature* **2012,** 488, (7411), 294-303.
3. Hori, Y., Electrochemical CO_2 Reduction on Metal Electrodes. In *Modern Aspects of Electrochemistry*, Vayenas, C. G.; White, R. E.; Gamboa-Aldeco, M. E., Eds. Springer New York: New York, NY, 2008; pp 89-189.
4. Kuhl, K. P.; Hatsukade, T.; Cave, E. R.; Abram, D. N.; Kibsgaard, J.; Jaramillo, T. F. *J. Am. Chem. Soc.* **2014,** 136, (40), 14107-14113.
5. Hori, Y.; Wakebe, H.; Tsukamoto, T.; Koga, O. *Electrochim. Acta* **1994,** 39, (11), 1833-1839.
6. Hori, Y.; Murata, A.; Takahashi, R. *J. Chem. Soc. Faraday Trans. 1* **1989,** 85, (8), 2309-2326.
7. Kuhl, K. P.; Cave, E. R.; Abram, D. N.; Jaramillo, T. F. *Energy Environ. Sci.* **2012,** 5, (5), 7050-7059.
8. Frumkin, A. N. *Trans. Faraday Soc.* **1959,** 55, (0), 156-167.

9. Akira, M.; Yoshio, H. *Bull. Chem. Soc. Jpn.* **1991,** 64, (1), 123-127.
10. Thorson, M. R.; Siil, K. I.; Kenis, P. J. A. *J. Electrochem. Soc.* **2013,** 160, (1), F69-F74.
11. Paik, W.; Andersen, T. N.; Eyring, H. *Electrochim. Acta* **1969,** 14, (12), 1217-1232.
12. Kaneco, S.; Iiba, K.; Katsumata, H.; Suzuki, T.; Ohta, K. *J. Solid State Electrochem.* **2007,** 11, (4), 490-495.
13. Singh, M. R.; Kwon, Y.; Lum, Y.; Ager, J. W.; Bell, A. T. *J. Am. Chem. Soc.* **2016,** 138, (39), 13006-13012.
14. Subbaraman, R.; Tripkovic, D.; Strmcnik, D.; Chang, K.-C.; Uchimura, M.; Paulikas, A. P.; Stamenkovic, V.; Markovic, N. M. *Science* **2011,** 334, (6060), 1256-1260.
15. Stoffelsma, C.; Rodriguez, P.; Garcia, G.; Garcia-Araez, N.; Strmcnik, D.; Marković, N. M.; Koper, M. T. M. *J. Am. Chem. Soc.* **2010,** 132, (45), 16127-16133.
16. Strmcnik D.; Kodama K.; van der Vliet, D.; Greeley J.; Stamenkovic, V. R.; Marković, N. M. *Nat. Chem.* **2009,** 1, (6), 466-472.
17. Suntivich, J.; Perry, E. E.; Gasteiger, H. A.; Shao-Horn, Y. *Electrocatalysis* **2013,** 4, (1), 49-55.
18. Angelucci, C. A.; Varela, H.; Tremiliosi-Filho, G.; Gomes, J. F. *Electrochem. Comm.* **2013,** 33, 10-13.
19. Lobaccaro, P.; Singh, M. R.; Clark, E. L.; Kwon, Y.; Bell, A. T.; Ager, J. W. *Phys. Chem. Chem. Phys.* **2016,** 18, (38), 26777-26785.
20. Giannozzi, P.; Baroni, S.; Bonini, N.; Calandra, M.; Car, R.; Cavazzoni, C.; Ceresoli, D.; Chiarotti, G.; Cococcioni, M.; Dabo, I.; Dal Corso, A.; de Gironcoli, S.; Fabris, S.; Fratesi, G.; Gebauer, R.; Gerstmann, U.; Gougoussis, C.; Kokalj, A.; Lazzeri, M.; Martin-Samos, L.; Marzari, N.; Mauri, F.; Mazzarello, R.; Paolini, S.; Pasquarello, A.; Paulatto, L.; Sbraccia, C.; Scandolo, S.; Sclauzero, G.; Seitsonen, A.; Smogunov, A.; Umari, P.; Wentzcovitch, R. *J. Phys. Condens. Matter* **2009,** 21, (39).
21. Bahn, S. R.; Jacobsen, K. W. *Comput. Sci. Eng.* **2002,** 4, (3), 56--66.
22. Wellendorff, J.; Lundgaard, K. T.; Møgelhøj, A.; Petzold, V.; Landis, D. D.; Nørskov, J. K.; Bligaard, T.; Jacobsen, K. W. *Phys. Rev. B* **2012,** 85, (23), 235149.
23. Yoo, J. S.; Abild-Pedersen, F.; Nørskov, J. K.; Studt, F. *ACS Catal.* **2014,** 4, (4), 1226-1233.
24. Monkhorst, H.; Pack, J. *Phys. Rev. B* **1976,** 13, (12), 5188-5192.
25. Chen, L. D.; Urushihara, M.; Chan, K.; Nørskov, J. *ACS Catal.* **2016**.
26. Peterson, A. A. *Top. Catal.* **2013,** 57, (1-4), 40-53.
27. Hahn, C.; Hatsukade, T.; Kim, Y. G.; Vailionis, A.; Baricuatro, J. H.; Higgins, D. C.; Nitopi, S. A.; Soriaga, M. P.; Jaramillo, T. F. *Proc. Natl. Acad. Sci.* **2017,** 114, (23), 5918-5923.
28. Jiang, H.; Klemmer, T. J.; Barnard, J. A.; Payzant, E. A. *J. Vac. Sci. Technol. A* **1998,** 16, (6), 3376-3383.
29. Hori, Y.; Takahashi, I.; Koga, O.; Hoshi, N. *J. Phys. Chem. B* **2002,** 106, (1), 15-17.
30. Schouten, K. J. P.; Qin, Z.; Gallent, E. P.; Koper, M. T. M. *J. Am. Chem. Soc.* **2012,** 134, (24), 9864-9867.
31. Roberts, F. S.; Kuhl, K. P.; Nilsson, A. *ChemCatChem* **2016,** 8, (6), 1119-1124.
32. Kim, Y.-G.; Baricuatro, J. H.; Javier, A.; Gregoire, J. M.; Soriaga, M. P. *Langmuir* **2014,** 30, (50), 15053-15056.
33. Durand, W. J.; Peterson, A. A.; Studt, F.; Abild-Pedersen, F.; Nørskov, J. K. *Surf. Sci.* **2011,** 605, (15–16), 1354-1359.

34. Schouten, K. J. P.; Pérez Gallent, E.; Koper, M. T. M. *ACS Catal.* **2013,** 3, (6), 1292-1295.
35. Montoya, J. H.; Shi, C.; Chan, K.; Nørskov, J. K. *J. Phys. Chem. Lett.* **2015,** 6, (11), 2032-2037.
36. Sandberg, R. B.; Montoya, J. H.; Chan, K.; Nørskov, J. K. *Surf. Sci.* **2016,** 654, 56-62.
37. Hori, Y.; Murata, A.; Yoshinami, Y. *J. Chem. Soc. Faraday Trans.* **1991,** 87, (1), 125-128.
38. Hatsukade, T.; Kuhl, K. P.; Cave, E. R.; Abram, D. N.; Jaramillo, T. F. *Phys. Chem. Chem. Phys.* **2014,** 16, (27), 13814-13819.
39. Kyriacou, G. Z.; Anagnostopoulos, A. K. *J. Appl. Electrochem.* **1993,** 23, (5), 483-486.
40. Goodpaster, J. D.; Bell, A. T.; Head-Gordon, M. *J. Phys. Chem. Lett.* **2016,** 7, (8), 1471-1477.
41. Schouten, K. J. P.; Kwon, Y.; van der Ham, C. J. M.; Qin, Z.; Koper, M. T. M. *Chem. Sci.* **2011,** 2, (10), 1902-1909.
42. Akhade, S. A.; McCrum, I. T.; Janik, M. J. *J. Electrochem. Soc.* **2016,** 163, (6), F477-F484.
43. Liu, X.; Xiao, J.; Peng, H.; Hong, X.; Chan, K.; Nørskov, J. K. *Nat. Commun.* **2017**.
44. Shi, C.; Hansen, H. A.; Lausche, A. C.; Nørskov, J. K. *Phys. Chem. Chem. Phys.* **2014,** 16, (10), 4720-4727.
45. Xiao, H.; Cheng, T.; Goddard, W. A.; Sundararaman, R. *J. Am. Chem. Soc.* **2016,** 138, (2), 483-486.
46. Ogasawara, H.; Brena, B.; Nordlund, D.; Nyberg, M.; Pelmenschikov, A.; Pettersson, L. G. M.; Nilsson, A. *Phys. Rev. Lett.* **2002,** 89, (27), 276102.
47. Łukomska, A.; Sobkowski, J. *J. Electroanal. Chem.* **2004,** 567, (1), 95-102.
48. Cheng, T.; Xiao, H.; Goddard, W. A. *J. Am. Chem. Soc.* **2016,** 138, (42), 13802-13805.
49. Strmcnik, D.; van der Vliet, D. F.; Chang, K. C.; Komanicky, V.; Kodama, K.; You, H.; Stamenkovic, V. R.; Marković, N. M. *J. Phys. Chem. Lett.* **2011,** 2, (21), 2733-2736.
50. Montoya, J. H.; Shi, C.; Chan, K.; Norskov, J. K. *J. Phys. Chem. Lett.* **2015,** 6, (11), 2032-2037.
51. Mortensen, J. J.; Hammer, B.; Nørskov, J. K. *Phys. Rev. Lett.* **1998,** 80, (19), 4333-4336.
52. Nørskov, J. K. N.; Studt, F.; Abild-Pedersen, F.; Bligaard, T., *Fundamental Concepts in Heterogeneous Catalysis*. Wiley, Hoboken, New Jersey: 2014.
53. Nørskov, J. K.; Bligaard, T.; Logadottir, A.; Kitchin, J. R.; Chen, J. G.; Pandelov, S.; Stimming, U. *J. Electrochem. Soc.* **2005,** 152, (3), J23-J26.
54. Shi, C.; O'Grady, C. P.; Peterson, A. A.; Hansen, H. A.; Nørskov, J. K. *Phys. Chem. Chem. Phys.* **2013,** 15, (19), 7114.
55. Montoya, J. H.; Peterson, A. A.; Nørskov, J. K. *ChemCatChem* **2013,** 5, (3), 737-742.
56. Trasatti, S. *Pure Appl. Chem.* **1986,** 58, (7).

Chapter 6

Effects of anion identity and concentration on electrochemical reduction of CO_2

6.1 Abstract

The electrochemical reduction of CO_2 is known to be influenced by the concentration and identity of the anionic species in the electrolyte; however, a full understanding of this phenomenon has not been developed. Here we present the results of experimental and computational studies aimed at understanding the role of electrolyte anions on the reduction of CO_2 over Cu surfaces. Experimental studies were done to show the effects of bicarbonate buffer concentration and the composition of other buffering anions on the partial currents of the major products formed by reduction of CO_2 over Cu. It was demonstrated that the composition and concentration of electrolyte anions has relatively little effect on the formation of CO, $HCOO^-$, C_2H_4, and CH_3CH_2OH, but has a significant effect on the formation of H_2 and CH_4. Continuum modeling was used to assess the effects of buffering anions on the pH at the electrode surface. The influence of pH on the activity of Cu for producing H_2 and CH_4 was also considered. Changes in the pH near the electrode surface were insufficient to explain the differences in activity and selectivity observed with changes in anion buffering capacity observed for the formation of H_2 and CH_4. Therefore, it is proposed that these differences are the result of the ability of buffering anions to donate hydrogen directly to the electrode surface and in competition with water. The effectiveness of buffering anions to serve as hydrogen donors is found to increase with decreasing pKa of the buffering anion.

6.2 Introduction

The electrochemical reduction of CO_2 offers a means for storing electrical energy produced by intermittent renewable resources, such as wind and solar radiation.[1-2] Hydrocarbons and alcohols are the preferred products of the CO_2 reduction reaction (CO2RR) because of their high energy density. To date, the only electrocatalyst that can produce these products with significant yields is copper (Cu).[3-5] While a large fraction of the total current used for the CO2RR over Cu yields desirable products, such as ethylene (C_2H_4) and ethanol (CH_3CH_2OH), a significant fraction of the total current goes to producing undesired products, such as hydrogen (H_2), methane (CH_4), carbon monoxide (CO), and formate anions ($HCOO^-$).[6-7] Since H_2 is the largest component of the undesired products, it is desirable to identify means for enhancing the fraction of the total current use to produce desired products of CO_2 reduction by mitigating the production of H_2. To do so requires understanding of how the composition and concentration of the electrolyte influence the mechanism of the CO2RR. We have previously demonstrated that alkali metal cations influence the distribution of products formed as a consequence of electrostatic interactions between solvated cations present at the outer Helmholtz plane and adsorbed species having large dipole moments (e.g., $*CO_2$, *CO, *OCCO).[8] This field stabilization decreases the energy for $*CO_2$ adsorption, the precursor to two-electron products, and C-C coupling to form *OCCO or *OCCHO, the precursor to C_2H_4 and C_2H_5OH.[8] As a consequence, the partial currents for forming H_2 and CH_4 are unaffected by the size of the alkali metal cation (Li^+ through Cs^+), whereas the partial currents for forming $HCOO^-$, C_2H_4, and CH_3CH_2OH increase monotonically with increasing alkali metal cation size.

A number of studies have also shown the distribution of products formed by CO_2 reduction over Cu is influenced by changes in the composition of the electrolyte anions.[7-9] Hori and coworkers have demonstrated that non-buffering anions (Cl^-,ClO_4^-, SO_4^{2-}) give high selectivities to C_2H_4 and CH_3CH_2OH, and lower selectivity to CH_4 and H_2 compared to bicarbonate anions (HCO_3^-), whereas phosphate anions ($H_2PO_4^-$) result in a higher selectivity to H_2 and CH_4.[7] The effects of bicarbonate concentration have also been investigated, and it was observed that with increasing anion concentration the rates of hydrogen evolution and methane production increased.[7, 9-10] The observed differences in selectivity with buffer concentration and buffer capacity were attributed to changes in the pH at the electrode surface; however, these changes in pH were not quantified nor was it explained how the electrolyte pH might cause the observed changes in product distribution.[7, 9-10] Given the lack of a clear interpretation of the effects of anion composition on the activity and selectivity of Cu for the CO2RR, we undertook an effort to develop a complete picture of the role of anionic species on the electrochemical reduction of CO_2. Our studies show that changes in pH in the vicinity of the electrode surface are insufficient to explain the differences in activity and selectivity observed with changes in anion buffering capacity, and we propose that these differences are the result of the ability of buffering anions to donate hydrogen directly to the electrode surface.

6.3 Experimental and computational methods

6.3.1. Electrode preparation

Cu thin films with specific crystal orientations were prepared by rf sputtering of Cu onto silicon (Si) single crystal substrates. This approach is based on previous studies demonstrating the epitaxial relationship between Cu and Si substrates of different orientations.[8, 11, 12] The present study utilizes Cu(100)-oriented thin films because it has been shown that this surface exhibits a high selectivity to the desired C_{2+} hydrocarbons and oxygenates (e.g., C_2H_4 and CH_3CH_2OH).[13] Single-side polished Si(100) wafers (Virginia semiconductor, 1-10 Ω cm) were diced into ~4 cm^2 sized pieces that were then used as electrode substrates. Prior to Cu deposition, the native oxide was removed from the Si substrates by submerging them in a 10% HF solution for 5 min. Immediately after HF etching, the Si pieces were transferred to a vacuum chamber for sputter deposition of Cu in an AJA ATC Orion-5 sputtering system. The base pressure of the sputtering system prior to deposition was ~$2x10^{-7}$ torr. The flow rate of the sputtering gas (Ar) was 25 sccm and the sputtering pressure was adjusted to $2x10^{-3}$ torr by controlling the speed at which the chamber was pumped, using a variable butterfly valve. Cu (99.999% Kurt Lesker) was deposited at a rate of 1 Å/s, as determined by a calibrated quartz crystal monitor, at ambient temperature. The total film thickness deposited was 100 nm.

6.3.2 Electrode characterization

The structure of the Cu thin films was characterized by X-ray diffraction. The orientation and epitaxial quality of the films were determined using symmetric θ-2θ scans, in plane ϕ scans, ω scans or rocking curves, and pole figures. XRD patterns were taken with a PANanalytical X'Pert diffractometer, which uses a Cu Kα (λ = 1.54056 Å) X-ray source. Symmetric θ-2θ scans were collected on samples fixed onto a flat glass slide in locked-coupled mode with a goniometer resolution of 0.001°. Measured diffraction patterns were compared to known standards taken from the International Center for Diffraction Data (ICDD) PDF4 database (card #71-4610 for Cu). X-ray diffraction analysis using both in plane and out of plane techniques demonstrate that Cu thin films can be grown epitaxially with in the (100) orientation from Si(100) (Chapter 5).[8]

6.3.3 Electrolyte preparation

Electrolyte solutions were prepared by mixing ultra-pure salts and 18.2 MΩ DI, and were used as the electrolyte without further purification. Bicarbonate buffered electrolytes were prepared from K_2CO_3 (99.995% Sigma Aldrich) which upon saturation gave $KHCO_3$ electrolytes of concentrations of 0.05, 0.10, and 0.20 M. To maintain constant salinity, K_2SO_4 (Sigma Aldrich 99.99%) was added to these solutions to a total salinity of 0.2 M. The pH of these solutions after CO_2 saturation was 6.4, 6.8, and 7.0 respectively. Phosphate buffered electrolytes were prepared from 0.05 M KH_2PO_4 (Sigma Aldrich 99.99%) and 0.05 M K_2HPO_4 (Sigma Aldrich 99.99%). The pH of this solution after CO_2 saturation was 6.8. Borate buffered electrolyte was prepared from .05 M $K_2B_4O_7$ (Sigma Aldrich 99.9%). The pH of this solution after CO_2 saturation was 6.7. Unbuffered solutions were prepared from 0.05 M K_2SO_4 and 0.1 M $KClO_4$ (Sigma Aldrich 99.99%). The pH's of these solutions after CO_2 saturation were 4.5 and 4.0 respectively.

6.3.4 Electrochemical measurements

All electrochemical experiments were conducted in a gas-tight electrochemical cell machined from polyether ether ketone (PEEK).[14] The cell was cleaned with 20 wt. % nitric acid

and oxidized in UV-generated ozone for 15 min prior to the initiation of an experiment. The working and counter electrodes were parallel and separated by an anion-conducting membrane (Selemion AMV AGC Inc.). A gas dispersion frit was incorporated into the cathode chamber to provide vigorous electrolyte mixing. The exposed geometric surface area of each electrode was 1 cm^2 and the electrolyte volume of each electrode chamber was 1.8 mL. The counter electrode was a Pt foil (99.9% Sigma Aldrich) that was flame annealed prior to each experiment. The working electrode potential was referenced against an Ag/AgCl electrode (Innovative Instruments Inc.) that was calibrated against a homemade standard hydrogen electrode (SHE). 0.05 M M_2CO_3 (M referring to an alkali metal cation) solutions were prepared by mixing ultra-pure salts (Sigma Aldrich 99.995%) and 18.2 MΩ DI, and were used as the electrolyte without further purification. The cathode chamber was sparged with CO_2 (99.999% Praxair) at a rate of 5 sccm for 20 min prior to and throughout the duration of all electrocatalytic measurements. Upon saturation with CO_2 the pH of the electrolyte was 6.8, which was maintained throughout the duration of electrolysis.

Electrochemical measurements were performed using a Biologic VSP-300 potentiostat. All electrochemical data were recorded versus the reference electrode and converted to the RHE scale. Potentiostatic electrochemical impedance spectroscopy (PEIS) was used to determine the uncompensated resistance (R_u) of the electrochemical cell by applying voltage waveforms about the open circuit potential with an amplitude of 20 mV and frequencies ranging from 50 Hz to 500 kHz. The potentiostat compensated for 85% of R_u *in situ* and the last 15% was post-corrected to arrive at accurate potentials. The electrocatalytic activity was assessed by conducting chronoamperometry at each fixed applied potential for 70 min.

6.3.5 Product analysis

The effluent from the electrochemical cell was passed through the sampling loop (250 μL) of an Agilent 7890B gas chromatograph equipped with a pulsed-discharge helium ionization detector (PDHID). He (99.9999% Praxair) was used as the carrier gas. The effluent of the electrochemical cell was sampled every 14 min. The gaseous products were separated using a Hayesep-Q capillary column (Agilent) connected in series with a packed ShinCarbon ST column (Restek Co.). The column oven was maintained at 50 °C for 1 min followed by a temperature ramp at 30 °C/min to 250 °C, which was maintained for the duration of the analysis. The signal response of the PDHID to each gaseous product was calibrated by analyzing a series of NIST-traceable standard gas mixtures (Air Gas).

The electrolyte from both electrode chambers was collected after electrolysis and analyzed using a Thermo Scientific UltiMate 3000 liquid chromatograph equipped with a refractive index detector (RID). The electrolyte aliquots were stored in a refrigerated autosampler until analyzed in order to minimize the evaporation of volatile products. The liquid-phase products contained in a 10 μL sample were separated using a series of two Aminex HPX 87-H columns (Bio-Rad) and a 1 mM sulfuric acid eluent (99.999% Sigma Aldrich). The column oven was maintained at 60 °C for the duration of the analysis. The signal response of the RID to each liquid-phase product was calibrated by analyzing standard solutions of each product at a concentration of 1, 10, and 50 mM.

6.3.6 Numerical simulations

To understand the effects of transport phenomena on the measured rates of CO_2 reduction, we used a diffusion-reaction model based on the work of Gupta et al. to determine the

pH and buffering anion concentration at the cathode.[15] We can consider the bulk of the electrolyte to be a well-mixed solution with concentrations of all species to be at their equilibrium values. This assumption is based on the vigorous agitation of the electrolyte by a stream of bubbles of CO_2. We assume that near the cathode surface there is a mass transfer boundary layer within which concentrations of each species change from that in the bulk to that at the cathode surface. CO_2 will diffuse through this boundary layer towards the electrode surface while hydroxide ions will diffuse away from the surface. Simultaneously, acid-base reactions consume and generate these species in the boundary layer, while CO_2 is consumed and OH^- is produced at the electrode surface. The reactions governing the acid base equilibria for bicarbonate electrolytes are shown below:

$$CO_{2(g)} \leftrightarrow CO_{2(aq)} \tag{1}$$

$$CO_{2(aq)} + OH^-_{(aq)} \leftrightarrow HCO^-_{3(aq)} \tag{2}$$

$$HCO^-_{3(aq)} + OH^-_{(aq)} \leftrightarrow CO^{2-}_{3(aq)} + H_2O_{(l)} \tag{3}$$

Dissolved CO_2 can also be hydrated to form carbonic acid; however, its concentration is ~10^{-3} of the concentration of dissolved CO_2. Therefore, the hydrated and dissolved CO_2 may be considered as a single species.[16] The associated rate and equilibrium constants for these reactions are taken from previous literature reports:[16-18] $K_1 = 3.35x10^{-2}\ M\ atm^{-1}$, $K_2 = 4.44x10^{7}\ M^{-1}$, $k_{2f} = 5.93x10^{3}\ M^{-1}\ s^{-1}$, $k_{2r} = 1.34x10^{-4}\ s^{-1}$, $K_3 = 4.66x10^{3}\ M^{-1}$, $k_{3f} = 1.00x10^{8}\ M^{-1}\ s^{-1}$, $k_{2r} = 2.15x10^{4}\ s^{-1}$. For the case in which biphosphate anion are used, the following acid-base reactions must be included:

$$H_3PO_{4(aq)} + OH^-_{(aq)} \leftrightarrow H_2PO^-_{4(aq)} + H_2O_{(l)} \tag{4}$$

$$H_2PO^-_{4(aq)} + OH^-_{(aq)} \leftrightarrow HPO^{2-}_{4(aq)} + H_2O_{(l)} \tag{5}$$

$$HPO^{2-}_{4(aq)} + OH^-_{(aq)} \leftrightarrow PO^{3-}_{4(aq)} + H_2O_{(l)} \tag{6}$$

The equilibrium constants for these reactions are taken from previous literature reports:[17] $K_4 = 6.92\ x\ 10^{11}\ M^{-1}$, $K_5 = 6.17x10^{6}\ M^{-1}$, $K_6 = 4.79x10^{1}\ M^{-1}$.

The concentrations of the relevant species at different reaction conditions are governed by the following set of coupled partial differential equations, which account for the simultaneous diffusion and reaction of all species but neglect their migration:

$$\frac{\partial(CO_{2(aq)})}{\partial t} = D_{CO_{2(aq)}} \frac{\partial^2(CO_{2(aq)})}{\partial x^2} - k_{2f}\left(CO_{2(aq)}\right)\left(OH^-_{(aq)}\right) + k_{2r}(HCO^-_{3(aq)}) \tag{7}$$

$$\frac{\partial(HCO^-_{3(aq)})}{\partial t} = D_{HCO^-_{3(aq)}} \frac{\partial^2(HCO^-_{3(aq)})}{\partial x^2} + k_{2f}\left(CO_{2(aq)}\right)\left(OH^-_{(aq)}\right) - k_{2r}\left(HCO^-_{3(aq)}\right) - k_{3f}\left(HCO^-_{3(aq)}\right)\left(OH^-_{(aq)}\right) + k_{3r}\left(CO^{2-}_{3(aq)}\right) \tag{8}$$

$$\frac{\partial(CO_{3(aq)}^{2-})}{\partial t} = D_{CO_{3(aq)}^{2-}} \frac{\partial^2(CO_{3(aq)}^{2-})}{\partial x^2} + k_{3f}\left(HCO_{3(aq)}^{-}\right)\left(OH_{(aq)}^{-}\right) - k_{3r}\left(CO_{3(aq)}^{2-}\right) \quad (9)$$

$$\frac{\partial(OH_{(aq)}^{-})}{\partial t} = D_{OH_{(aq)}^{-}} \frac{\partial^2(OH_{(aq)}^{-})}{\partial x^2} - k_{2f}\left(CO_{2(aq)}\right)\left(OH_{(aq)}^{-}\right) + k_{2r}\left(HCO_{3(aq)}^{-}\right) - k_{3f}\left(HCO_{3(aq)}^{-}\right)\left(OH_{(aq)}^{-}\right) + k_{3r}\left(CO_{3(aq)}^{2-}\right) \quad (10)$$

The boundary conditions for eqns. 7-10 are set at the electrode surface ($x = 0$) and at the edge of the boundary layer ($x = \delta$). A boundary layer thickness of 100 μm was assumed. This value is comparable to that measured previously under the same flow conditions in the electrochemical cell used for the present studies.[19] At the edge of the boundary layer, the concentrations of all species are set to their bulk equilibrium values and at the electrode surface, the experimentally measured data give the rates of CO_2 consumption and OH^- generation:

$$D_{CO_{2(aq)}} \frac{d(CO_{2(aq)})}{\partial x} = R_{CO2} \quad (11)$$

$$D_{HCO_{3(aq)}^{-}} \frac{d(HCO_{3(aq)}^{-})}{\partial x} = 0 \quad (12)$$

$$D_{CO_{3(aq)}^{2-}} \frac{d\left(CO_{3(aq)}^{2-}\right)}{\partial x} = 0 \quad (13)$$

$$D_{OH_{(aq)}^{-}} \frac{d(OH_{(aq)}^{-})}{\partial x} = R_{OH-} \quad (14)$$

Where R_{CO2} and R_{OH-} are the rates of CO_2 consumption and hydroxide generation respectively, in units of moles/s cm^2. Diffusion coefficients were taken from previous data:[17] $D_{CO_{2(aq)}} = 1.91x10^{-9}\ m^2s^{-1}$, $D_{HCO_{3(aq)}^{-}} = 9.23x10^{-10}\ m^2s^{-1}$, $D_{CO_{3(aq)}^{2-}} = 1.19x10^{-9}\ m^2s^{-1}$, $D_{OH_{(aq)}^{-}} = 5.27x10^{-9}\ m^2s^{-1}$. Eqns. 7-10 together with the boundary conditions given by eqns. 11-4 were solved using COMSOL Multiphysics 5.1 to yield pH and CO_2 concentration profiles in the hydrodynamic boundary layer.

6.4 Results and discussion

6.4.1 Buffer concentration effects on the activity of Cu(100) oriented films

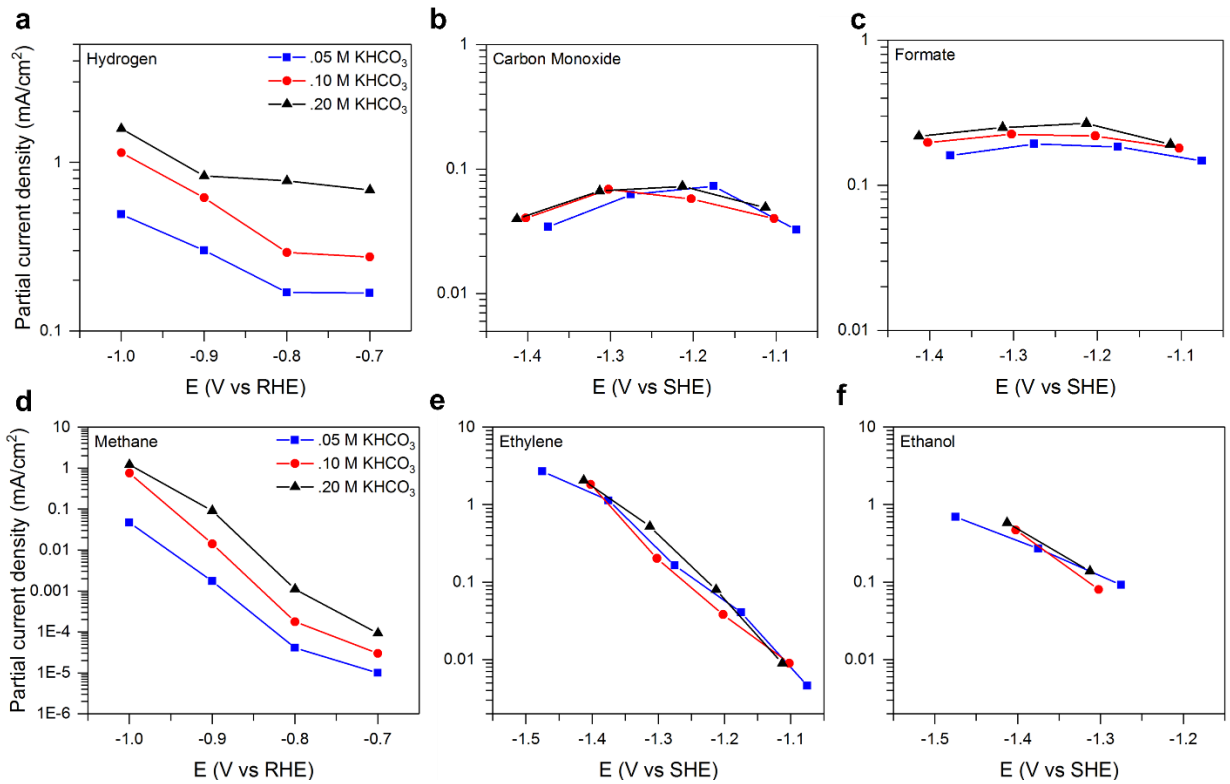

Figure 6.1: Effect of bicarbonate buffer concentration on the partial currents of formation of major products of CO_2 reduction over Cu(100). Partial current densities for each of the major products as a function of the bicarbonate buffer concentration on Cu(100). Data are presented at potential between −0.7 to −1.0 V vs RHE. For C_2H_4 and CH_3CH_2OH, partial currents are reported against an SHE scale.

The steady-state activity and selectivity of the Cu(100) surface was investigated by potentiometric electrolysis at potentials between -0.7 and -1.0 V vs the reversible hydrogen electrode (RHE). The initial measurements were carried out in CO_2-saturated electrolytes of 0.05 M, 0.10 M, and 0.20 M $KHCO_3$ with K_2SO_4 added to maintain the salinity of each electrolyte at 0.2 M. Figure 1 shows that with increasing buffer concentration, the partial currents of H_2 and CH_4 formation increase. By contrast, the partial currents of CO, $HCOO^-$, C_2H_4 and CH_3CH_2OH formation are minimally affected by buffer concentration, when the cathode voltage is given versus the standard hydrogen electrode (SHE), which accounts for differences in bulk pH of the electrolyte. These results are consistent with previous studies on the effects of bicarbonate concentration on the activity of Cu for the CO2RR.[7, 9, 10, 20]

To understand why it the partial currents of H_2 and CH_4 should be plotted on the RHE scale and those for the CO, $HCOO^-$, C_2H_4, and CH_3CH_2OH on the SHE scale, it is necessary to review the meaning of these scales and understand how they relate to the elementary processes leading to each product. The SHE scale defines the potential for a given reaction relative to the potential for the reaction:

$$2\,H^+_{(aq)} + 2\,e^- \leftrightarrow H_{2(g)} \qquad (15)$$

with all components at unit activity ($P_{H_2} = 1\ bar, a_{H^+} = 1$), the reference state. For these conditions, the potential for reaction 1, is E^o_{H2}, which by convention is set to zero. The potential of the standard hydrogen electrode can be determined for other conditions using the Nernst equation:

$$E_{H_2} = E^o_{H_2} + \frac{RT}{2F} ln \frac{[H^+]}{p^{1/2}_{H_2}}$$

(16)

At room temperature and fixed pressure of hydrogen ($P_{H_2} = 1\ bar$), this reduces to:

$$E_{H_2} = E^o_{H_2} - 0.059\ pH$$

(17)

The potential for any chemical reaction can now be referenced to the SHE and is given by the following equation:

$$E_{SHE} = E^o_{SHE} - 0.059\ pH \quad (18)$$

Here $E^o_{H_2}$ is the potential for the reaction of interest referenced to the standard hydrogen electrode under standard conditions.

A second reference potential scale is the reversible hydrogen electrode scale (RHE). The reversible hydrogen electrode is a subtype of the standard hydrogen electrode and is used for electrochemical processes. Unlike the standard hydrogen electrode, potentials measured relative to the reference hydrogen electrode do not change with pH. The RHE scale and the SHE scale are related by:

$$E_{RHE} = E_{SHE} + 0.059\ pH \quad (19)$$

For reactions involving the same number of protons and electrons, the parital current vs cathode potential expressed on the RHE scale is not expected to shift with pH. An example of such a reaction would be the hydrogenation of CO:

$$*CO + H^+ + e^- \longrightarrow *CHO \quad (20)$$

However, if the reaction does not involve a proton-electron transfer, the partial current vs cathode potential expressed on SHE scale should not shift with pH. An example of a reaction of this type would be coupling of two adsorbed CO molecules:

$$*CO + *CO \longrightarrow *OCCO \quad (21)$$

It should be noted that these conclusions will hold under conditions, such as those relevant to the CO2RR, where electron reduction of water, $H_2O + e^- \longrightarrow \frac{1}{2}H_{2(g)} + OH^-_{(aq)}$, rather than the reduction of a proton, $H^+_{(aq)} + e^- \longleftrightarrow \frac{1}{2}H_{2(g)}$ is the source of hydrogen. We note that a proton transfer reaction in which water is the reactant: depends on pH in the same was as if a proton were the reactant, since the concentrations of protons and hydroxide ions are related through the following relationship:

$$-log[H^+] - log[OH^-] = 14 \quad (22)$$

It has been observed previously that partial currents for the formation of multicarbon products such as C_2H_4 and CH_3CH_2OH are pH independent when the cathode potential is reported on an SHE scale, meaning that they are sensitive to pH on an RHE scale.[20] In particular, the potential at which these products are observed becomes more positive as the pH of the electrolyte increases, in accordance with the Nernst equation. This conclusion can be understood considering the mechanism for the formation of these products. Density functional theory calculations have shown that carbon-carbon bond formation is the rate determining step for forming any multicarbon product observed during CO_2R,.[21, 22] and occurs via coupling of two adsorbed CO molecules (denoted *CO) or the addition of an adsorbed CO molecule to an adsorbed formyl (*CHO) molecule:

$$*CO + *CO \longrightarrow *OCCO \tag{23}$$

$$*CO + *CHO \longrightarrow *OCCHO \tag{24}$$

As neither of these elementary reactions involves a proton transfer in the rate determining step, the rates of both reactions should be pH independent, consistent with the observation of a pH independence of the rate of multicarbon product formation on an SHE scale. Therefore, our observation (see Figure 1) that the partial currents for the formation of C_2H_4 and CH_3CH_2OH formation are independent of buffer concentration when the rates are compared on an SHE scale is what should be expected. Similarly, the production of CO and $HCOO^-$ have previously been shown to be independent of pH, suggesting that the rate limiting step does not involve a concerted proton-coupled electron-transfer step, but rather electron transfer to form a $CO_2^{\delta-}$.[23-27] We note here that the effects of pH and buffer concentration on the formation of CO and $HCOO^-$ can be observed more readily on metals selective for these products.

The rate limiting step for production of methane, however, is proposed to be the hydrogenation of adsorbed CO to form adsorbed CHO.[28]

$$*CO + H_2O + e^- \longrightarrow *CHO + OH^- \tag{25}$$

Consequently, this reaction should have a pH dependence on an SHE scale, and be pH independent on an RHE scale if no specific effects of pH are involved. Similarly, hydrogen evolution should be pH independent on an RHE scale assuming no explicit effects of pH.

6.4.2 Surface pH effects for bicarbonate buffer electrolytes

For the data presented in Figure 1, the cathode potential on the RHE scale was determined using the bulk pH of the solution. Previous work has shown that while the bulk of CO_2-saturated electrolyte solution of $KHCO_3$ has a pH of 6.8, the pH near the cathode can rise to nearly 10, as a consequence of electrolyte polarization, a phenomenon that becomes particularly important for cathodes potentials below ~ -0.9 V.[29] For this range of pHs, the source of hydrogen for the formation of H_2 and the hydrogenation of CO_2 is adsorbed H_2O. H atoms are produced at the cathode surface by the reaction of adsorbed H_2O with an electron. The counter product of this reaction is an OH^- anion, which is released into the electrolyte. In the presence of a buffering anion, such as HCO_3^-, the following reaction can occur:

$$OH^- + HCO_3^- \longrightarrow H_2O + CO_3^{2-} \tag{26}$$

Hydroxide anions can also react with CO_2 to form bicarbonate anions, thereby depleting the availability of the reactant. To clearly define the extent to which the pH at the cathode surface affects partial current densities for H_2 and CH_4, the surface pH was calculated as a function of the current density for different HCO_3^- concentrations (see Methods for full description).[15, 29]

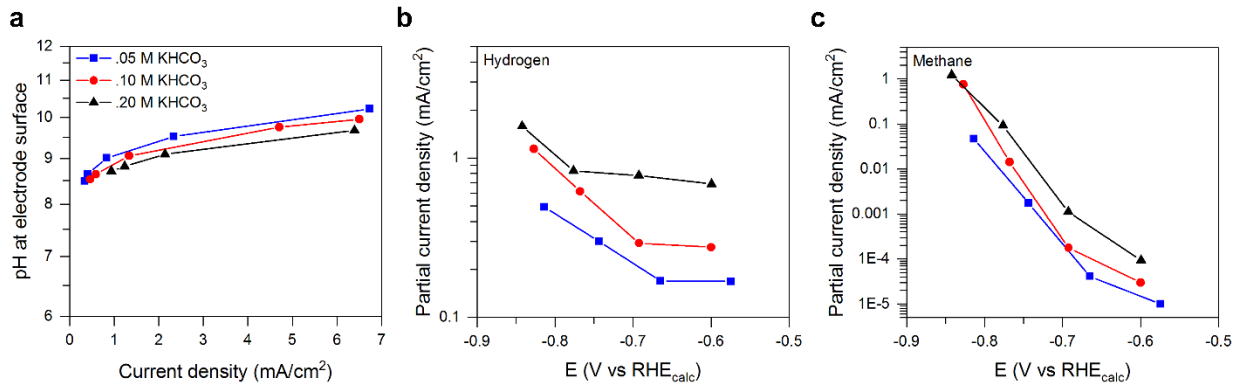

Figure 6.2: Surface pH effects on the partial currents of formation of major products of CO_2 reduction over Cu(100). a) pH at the electrode surface as a function of current density with increasing bicarbonate buffer concentration. b) Partial current densities for H_2 and CH_4 production as a function of the bicarbonate buffer concentration on Cu(100). Data are presented at potentials vs RHE_{calc} using the calculated local pH, rather than the pH of the bulk electrolyte.

Figure 2 shows that the pH at the cathode surface is higher than that of the bulk electrolyte, and increases with increasing current density as a consequence of the increase in the rate of hydroxide anion formation at the cathode. However, the differences in surface pH with buffer concentration are relatively small, particularly at low current densities, consistent with previous calculations of the effects of buffer concentration on the local pH during CO_2R.[15, 29] The partial currents of H_2 and CH_4 production can now be examined on a calculated RHE scale. The calculated RHE is related to the SHE potential and the pH at the electrode surface obtained from the model, rather than the bulk electrolyte pH:

$$E_{RHE_{calc}} = E_{SHE} + 0.059\, pH_{calc} \tag{25}$$

Figure 2 shows that substantial differences in activity persist even after differences in surface pH with buffer concentration are taken into account. Namely, the partial currents of H_2 and CH_4 production increase with buffer concentration irrespective of differences in local pH.

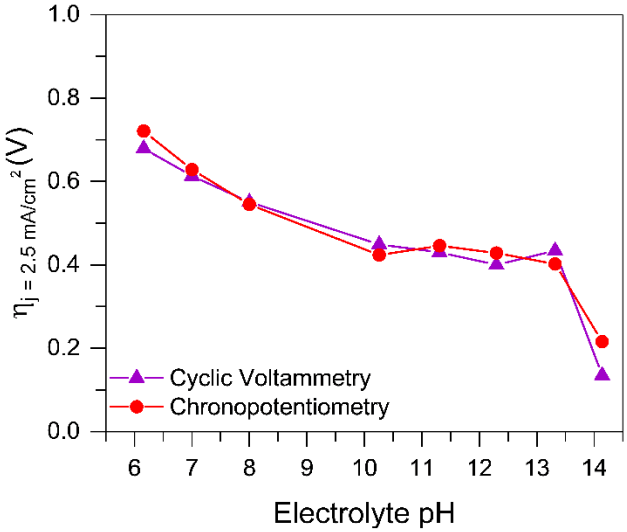

Figure 6.3: The overpotential for the HER over polycrystalline Cu as a function of pH for a current density of 2.5 mA/cm^2.

Previous studies have shown that HER activity is influenced by pH, contrary to what would be expected.[30-33] To investigate the influence of this effect, HER activity measurements were performed on a polycrystalline Cu electrode in a rotating disk electrode configuration in order to minimize mass transfer effects. The activity was measured as a function of electrolyte pH in the absence of CO_2 in a mixture of KCl and KOH electrolytes in order to maintain the total salinity of the electrolyte constant. Figure 3 shows that for a current density of 2.5 mA/cm^2, the overpotential for hydrogen evolution decreases with increasing electrolyte pH. This finding is consistent with previous studies of the explicit effect of pH on the rate of hydrogen evolution, which attribute the increase in the rate of this reaction with increasing pH to the stronger adsorption of hydrogen atoms to the surface of Cu.[34] The authors of this study explain that since Cu binds hydrogen more weakly than would optimal for high HER activity, an increase in the hydrogen binding energy should increase the HER activity.[35] Therefore, the explicit effect of pH on HER activity is to increase the rate of this reaction with increasing pH. One might similarly expect the rate of methane formation to increase with increasing pH, since the rate-limiting step for this reaction has been proposed to be *H + *CO → *HCO.[28, 36] Figure 4 shows data, adapted from Hori and coworkers, for the partial currents of methane production from CO reduction, at a range of electrolyte pH values. Similar studies for CO_2 reduction are not possible since OH^- will react with CO_2 to form HCO_3^-. These data shows that the partial current of methane formation increases with increasing pH, in a manner similar to that seen for hydrogen evolution. It is notable, though, that the trends in the rates of H_2 and CH_4 production seen in Figures 3 and 4 are opposite to those observed with increasing buffer concentration seen in Figure 1. In the latter figure shows that as the highest activity is observed for the highest buffer concentration, which has the lowest near-surface pH. What we conclude from the analysis to this point is that changes in local pH with buffer concentration do not fully account for the observed differences in the rates of H_2 and CH_4 formation.

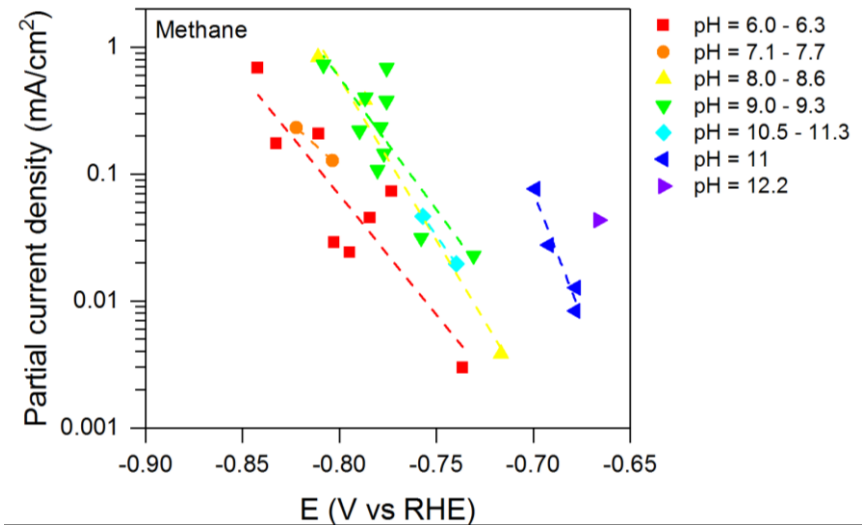

Figure 6.4: pH effects on the partial currents of formation of methane during CO reduction over polycrystalline Cu. (Adapted from Hori and coworkers)[20] Partial current densities for methane at a range of pH values. Methane activity is observed to increase with pH.

6.4.3 Buffering anions as a hydrogen source

The preceding conclusion led us to examine the hypothesis that products for which the rate-limiting step involves hydrogen addition (H_2 and CH_4) should depend on the source of hydrogen, while products for which the rate-limiting step does not involve hydrogen addition should be unaffected by the nature of the source of hydrogen. A plausible explanation for the trends in partial current density observed with buffer concentration is that the hydrogen for these reaction steps may come not only from water but also from a another source, such as HCO_3^-.

$$HCO_3^- + e^- \longrightarrow {}^*H + CO_3^{2-} \qquad (26)$$

While this idea has been proposed previously, little evidence for it has been given.[26] We note that even though the concentration of HCO_3^- is substantially lower than that of water, the pKa of HCO_3^- is 4 pKa units lower than that of water, which means that HCO_3^- can be considered as a relevant hydrogen donor. For the case of HCO_3^-, the concentration of this anion near the cathode surface under the conditions used in the present studies is estimated to be ~ 50% of the bulk electrolyte concentration (0.1 M) (see SI), which is about 10^3 lower than the concentration of water (55 M). On the other hand the equilibrium constant for the deprotonation of HCO_3^- is 10^4 higher than that for H_2O. Therefore, it is conceivable that HCO_3^- could serve as a source of H atoms.

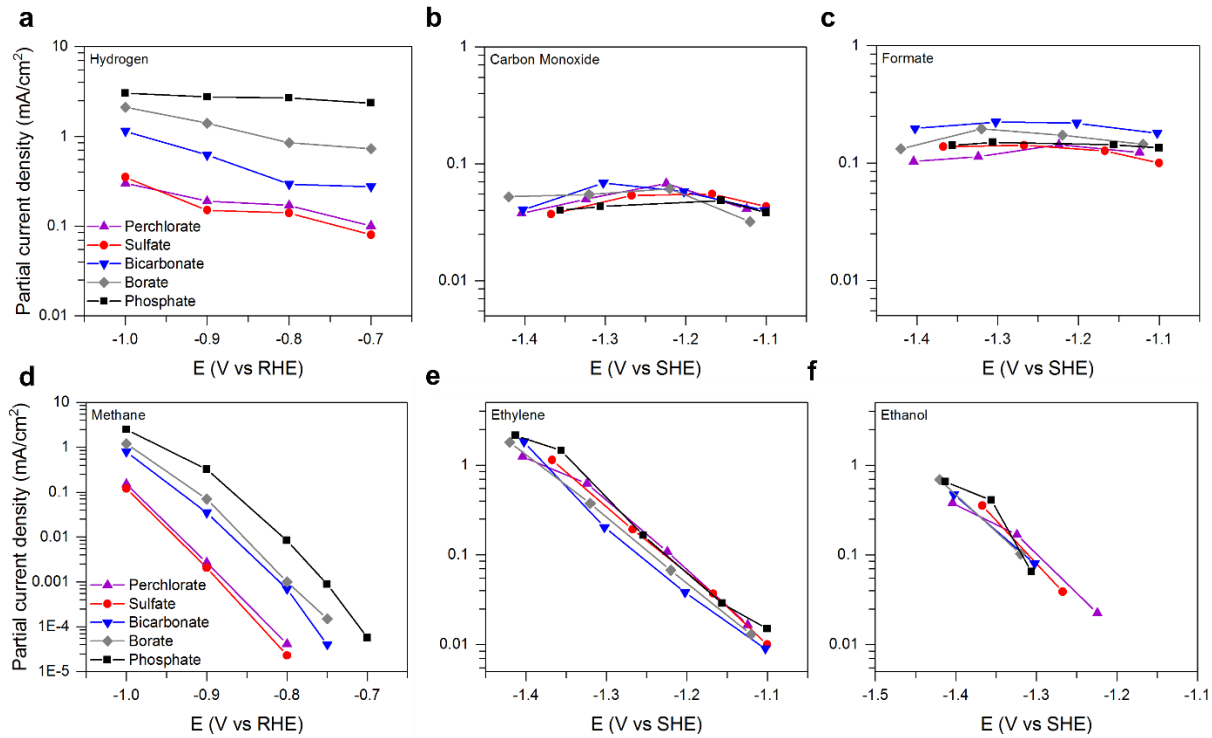

Figure 6.5: Partial current densities for major products of CO_2 reduction over Cu (100) in different anionic electrolytes. Partial current densities for each of the major products as a function of the electrolyte anion on Cu(100). All electrolytes are of a fixed potassium cation concentration of 0.1 M. Data are presented at potential between −0.7 to −1.0 V vs RHE. For C_2H_4 and CH_3CH_2OH, partial currents are reported against an SHE scale.

6.4.4 Buffer identity effects on the activity of Cu(100) oriented films

To investigate the possibility that buffering anions can act a source of hydrogen, the steady state activity and selectivity of the Cu(100) surface was investigated by potentiometric electrolysis at potentials from -0.7 to -1.0 V vs RHE carried out in CO_2-saturated electrolytes containing different anions. Potassium cations were used in all electrolytes. Two classes of anions were used: buffering and non-buffering. For non-buffering electrolytes, the two electrolytes chosen were perchlorate (ClO_4^-), which is a weakly adsorbing anion and sulfate (SO_4^{2-}), which is a more strongly adsorbing anion.[37] The buffering anions were chosen to have a range of pKa's from 7 to 10. The buffer equilibrium reaction and the pK_a for each anion are shown below.[17]

$$HCO_3^- \leftrightarrow H^+ + CO_3^{2-}, pKa = 10.33 \quad (25)$$

$$B(OH)_3 + H_2O \leftrightarrow H^+ + B(OH)_4^-, pKa = 9.23 \quad (26)$$

$$H_2PO_4^- \leftrightarrow H^+ + HPO_4^{2-}, pKa = 7.21 \quad (27)$$

Figure 5 shows the partial current density of each of the major products of CO_2 reduction over Cu(100) as a function of the potential for all five electrolyte compositions. The current density for hydrogen evolution is the same for $KClO_4$ and K_2SO_4, indicating that ClO_4^- and SO_4^{2-} have no effect on the rate of the HER. Because the potentials applied during CO_2 reduction are

much more negative than the potential of zero charge (PZC) of the low-index facets of Cu, ~ −0.7 V_{SHE} [38], solvated cations, rather than anions should accumulate near the surface of the electrode during reaction.[21, 24] On the other hand, Figure 5 shows that electrolytes containing buffering anions yield significantly higher rate of hydrogen evolution, and that the partial current increases in the order HCO_3^- < H_3BO_3 < HPO_4^{2-}, in the order of decreasing pK_a of the anion. The partial current for methane production is also independent of anion identity for non-buffering anions, but increases with decreasing pK_a of the buffering anion. The partial currents of CO and $HCOO^-$ formation are insensitive to the anion identity when compared on an SHE scale, and have been shown previously to be independent of pH.[23-26] The partial currents for C_2H_4 and CH_3CH_2OH vs cathode potential expressed on the SHE scale is also independent of anion identity, consistent with previous observation.[20]

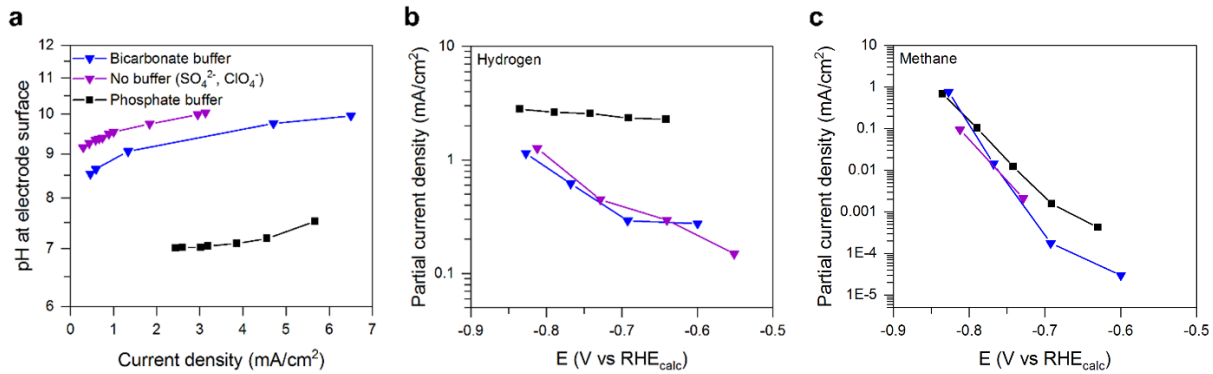

Figure 6.6: Surface pH and anion identity effects on the partial currents of formation of major products of CO_2 reduction over Cu(100). a) pH at the electrode surface as a function of current density with different anionic electrolytes. All electrolytes are of a fixed potassium cation concentration of 0.1 M. b) Partial current densities for H_2 and CH_4 production as a function of the electrolyte identity on Cu(100). Data are presented at potential between −0.7 to −1.1 V vs RHE using the calculated local pH, rather than the pH of the bulk electrolyte.

6.4.5 Surface pH effects for different buffer electrolytes

To assess the extent to which differences in the partial currents for H_2 and CH_4 observed for buffering and non-buffering annions are due to differences in the local pH at the cathode surface, we calculated the local pH as a function of current density for all electrolytes. Figure 6a show that for non-buffering anions, the surface pH is higher than that for bicarbonate anions at any concentration. To determine whether differences in local pH could account for the differences in the observed activity, the partial currents for H_2 and CH_4 production were plotted versus the calculated RHE potential. Figures 6b and 6c shows nearly identical partial currents for H_2 and CH_4 formation in electrolyte containing ClO_4^-, SO_4^{2-}, or HCO_3^-. It is also notable that difference between partial currents at given cathode voltage for experiments carried out in electrolytes containing $KHCO_3$ vs $KClO_4$ or KSO_4 is much smaller in Figure 6b than in Figure 5, suggesting that a large part of the difference seen Figure 5 is due to the differences in the pH of the electrolytes at the cathode surface. In unbuffered electrolyte, HCO_3^- ions can be formed from reaction of CO_2 with OH^-, and these HCO_3^- ions could then act as a hydrogen source. However, the concentration of these ions formed is estimated to be three orders of magnitude lower than their concentration in the electrolyte with HCO_3^- intentionally added. The reason for the higher than expected partial currents of HER and methane production is likely due to the more alkaline

pH near the electrode surface relative to the case in which buffers are added to the electrolyte. With increasing pH, we showed above that the HER rate increases on an RHE scale, as does the rate of methane production. Thus, HCO_3^- and H_2O at this higher pH are competitive hydrogen donors. Figure 6a shows that the cathode surface pH in KH_2PO_4 is lower than that in $KHCO_3$; however, Figure 6b shows that the partial current for H_2 is much higher in KH_2PO_4 than in $KHCO_3$. We hypothesize that this difference is due the significantly higher ability of H_2PO4^- to serve as a source of hydrogen due to its considerably lower pK_a (see above). Figure 6c shows a qualitatively similar pattern for CH_4 as that seen Figure 6b for H_2; however, in the case of CH_4, the partial current is much less sensitive to the anion composition, particularly at low applied potentials, than for the formation of H_2. We speculate that this difference in sensitivity could be due to the relative importance of surface hydrogenation (via *H) versus hydrogenation from solution (via H transfer from H_2O) in the rate-limiting step for the formation of these two products.[39]

6.5 Conclusions

In this study we have attempted to develop a complete picture of the role of anion composition on the electrochemical reduction of CO_2. We have confirmed that the composition and concentration of electrolyte anions has relatively little effect on the formation of CO, $HCOO^-$, C_2H_4, and CH_3CH_2OH. This finding is attributed to fact that the rate-limiting step for the formation of each of these products does not involve the addition of hydrogen atoms, a process that can be thought of as the concerted transfer of a proton and electron or the reaction of a water molecule and an electron with the release of a hydroxyl anion. By contrast, the formation of H_2 and CH_4 do exhibit a strong sensitivity to the composition and concentration of the electrolyte anion. It is notable that once differences in the pH at the cathode surface versus the bulk electrolyte are taken into account, significant differences in the partial currents for H_2 and CH_4 are still observed at a given potential vs the RHE (determined using the local pH). We propose that these residual differences are associated with the ability of buffering anions to serve as a significant source of hydrogen in competition with water. We note that while the concentrations of buffering anions is much lower than that of water, the pKa's of these anions are much larger than that of water. The results of this study suggest that to maximize the yields of multicarbon products such as C_2H_4 and CH_3CH_2OH, while minimizing production of H_2 and CH_4, one should use electrolytes with low buffering capacity. While, these electrolytes will have a reduced ability to mitigate changes caused by concentration polarization at high reaction rates, which will result in a reduced faradaic efficiency to the desired products, these effects can be offset by reducing the boundary layer thickness for mass transfer by stirring or . In view of the trade-off between the benefits of buffering and non-buffering anions, buffering electrolytes of low salinity (0.1 M $KHCO_3$) are preferred to maximize the production of desired C_{2+} products.

6.6 References

1. Lewis, N. S.; Nocera, D. G. *Proc. Natl. Acad. Sci.* **2006,** 103, (43), 15729-15735.
2. Chu, S.; Majumdar, A. *Nature* **2012,** 488, (7411), 294-303.

3. Hori, Y.; Wakebe, H.; Tsukamoto, T.; Koga, O. *Electrochim. Acta* **1994,** 39, (11), 1833-1839.
4. Kuhl, K. P.; Hatsukade, T.; Cave, E. R.; Abram, D. N.; Kibsgaard, J.; Jaramillo, T. F. *J. Am. Chem. Soc.* **2014,** 136, (40), 14107-14113.
5. Hori, Y., Electrochemical CO_2 Reduction on Metal Electrodes. In *Modern Aspects of Electrochemistry*, Vayenas, C. G.; White, R. E.; Gamboa-Aldeco, M. E., Eds. Springer New York: New York, NY, 2008; pp 89-189.
6. Kuhl, K. P.; Cave, E. R.; Abram, D. N.; Jaramillo, T. F. *Energy Environ. Sci.* **2012,** 5, (5), 7050-7059.
7. Hori, Y.; Murata, A.; Takahashi, R. *J. Chem. Soc. Faraday Trans. 1* **1989,** 85, (8), 2309-2326.
8. Resasco, J.; Chen, L. D.; Clark, E.; Tsai, C.; Hahn, C.; Jaramillo, T. F.; Chan, K.; Bell, A. T. *J. Am. Chem. Soc.* **2017,** 139, 11277-11287.
9. Varela, A. S.; Kroschel, M.; Reier, T.; Strasser, P. *Catal. Today* **2016,** 260, 8-13.
10. Kas, R.; Kortlever, R.; Yılmaz, H.; Koper, M. T. M.; Mul, G. *ChemElectroChem* **2015,** 2, (3), 354-358.
11. Hahn, C.; Hatsukade, T.; Kim, Y.-G.; Vailionis, A.; Baricuatro, J. H.; Higgins, D. C.; Nitopi, S. A.; Soriaga, M. P.; Jaramillo, T. F. *Proc. Natl. Acad. Sci.* **2017,** 114, (23), 5918-5923.
12. Jiang, H.; Klemmer, T. J.; Barnard, J. A.; Payzant, E. A. *J. Vac. Sci. Technol. A* **1998,** 16, (6), 3376-3383.
13. Kim, Y.-G.; Baricuatro, J. H.; Javier, A.; Gregoire, J. M.; Soriaga, M. P. *Langmuir* **2014,** 30, (50), 15053-15056.
14. Lobaccaro, P.; Singh, M. R.; Clark, E. L.; Kwon, Y.; Bell, A. T.; Ager, J. W. *Phys. Chem. Chem. Phys.* **2016,** 18, (38), 26777-26785.
15. Gupta, N.; Gattrell, M.; MacDougall, B. *J. Appl. Electrochem.* **2006,** 36, (2), 161-172.
16. Butler, J. N., *Carbon dioxide equilibria and their applications*. CRC Press: 1991.
17. Haynes, W. M., *CRC handbook of chemistry and physics*. CRC press: 2014.
18. Schulz, K. G.; Riebesell, U.; Rost, B.; Thoms, S.; Zeebe, R. E. *Mar. Chem.* **2006,** 100, (1), 53-65.
19. Lum, Y.; Yue, B.; Lobaccaro, P.; Bell, A. T.; Ager, J. W. *J. Phys. Chem. C* **2017,** 121, (26), 14191-14203.
20. Hori, Y.; Takahashi, R.; Yoshinami, Y.; Murata, A. *J. Phys. Chem. B* **1997,** 101, (36), 7075-7081.
21. Goodpaster, J. D.; Bell, A. T.; Head-Gordon, M. *J. Phys. Chem. Lett.* **2016,** 7, (8), 1471-1477.
22. Montoya, J. H.; Shi, C.; Chan, K.; Nørskov, J. K. *J. Phys. Chem. Lett.* **2015,** 6, (11), 2032-2037.
23. Shi, C.; O'Grady, C. P.; Peterson, A. A.; Hansen, H. A.; Norskov, J. K. *Phys. Chem. Chem. Phys.* **2013,** 15, (19), 7114-7122.
24. Cheng, T.; Xiao, H.; Goddard, W. A. *J. Am. Chem. Soc.* **2016,** 138, (42), 13802-13805.
25. Yoshio, H.; Shin, S. *Bull. Chem. Soc. Jpn.* **1982,** 55, (3), 660-665.
26. Wuttig, A.; Yaguchi, M.; Motobayashi, K.; Osawa, M.; Surendranath, Y. *Proc. Natl. Acad. Sci.* **2016,** 113, (32), E4585-E4593.
27. Wuttig, A.; Yoon, Y.; Ryu, J.; Surendranath, Y. *J. Am. Chem. Soc* **2017,** 139, 17109-17113.

28. Liu, X.; Xiao, J.; Peng, H.; Hong, X.; Chan, K.; Nørskov, J. K. *Nat. Commun.* **2017,** 8, 15438.
29. Singh, M. R.; Clark, E. L.; Bell, A. T. *Phys. Chem. Chem. Phys.* **2015,** 17, (29), 18924-18936.
30. Bockris, J. O. M.; Potter, E. C. *J. Electrochem. Soc.* **1952,** 99, (4), 169-186.
31. Durst, J.; Siebel, A.; Simon, C.; Hasche, F.; Herranz, J.; Gasteiger, H. A. *Energy Environ. Sci.* **2014,** 7, (7), 2255-2260.
32. Strmcnik, D.; Uchimura, M.; Wang, C.; Subbaraman, R.; Danilovic, N.; van der, V.; Paulikas, A. P.; Stamenkovic, V. R.; Markovic, N. M. *Nat. Chem.* **2013,** 5, (4), 300-306.
33. Ledezma-Yanez, I.; Wallace, W. D. Z.; Sebastián-Pascual, P.; Climent, V.; Feliu, J. M.; Koper, M. T. M. *Nat. Energy* **2017,** 2, 17031.
34. Sheng, W.; Zhuang, Z.; Gao, M.; Zheng, J.; Chen, J. G.; Yan, Y. *Nat. Commun.* **2015,** 6, 5848.
35. Nørskov, J. K.; Bligaard, T.; Logadottir, A.; Kitchin, J. R.; Chen, J. G.; Pandelov, S.; Stimming, U. *J. Electrochem. Soc.* **2005,** 152, (3), J23-J26.
36. Peterson, A. A.; Abild-Pedersen, F.; Studt, F.; Rossmeisl, J.; Norskov, J. K. *Energy Environ. Sci.* **2010,** 3, (9), 1311-1315.
37. Mostany, J.; Herrero, E.; Feliu, J. M.; Lipkowski, J. *J. Phys. Chem. B* **2002,** 106, (49), 12787-12796.
38. Łukomska, A.; Sobkowski, J. *J. Electroanal. Chem.* **2004,** 567, (1), 95-102.
39. Cheng, T.; Xiao, H.; Goddard, W. A. *Proc. Natl. Acad. Sci.* **2017,** 114, (8), 1795-1800.